Final Research Report Submitted to the Austrian Marshall Plan Foundation

Submitted by:
Kuseso Onai
Marshall Plan Scholarship Recipient 2019

Supervised by:
Univ.-Prof. Dr.-Ing. Annette Muetze
Ass.Prof. Dipl.-Ing. Dr.techn. Roland Seebacher
Ass.Prof. Dipl.-Ing. Dr.techn. Klaus Krischan
Graz University of Technology
Electric Drives and Machines Institute
Graz, Austria

January – August 2019

Acknowledgements:

My foremost appreciation goes to the Austrian Marshall Plan Foundation for awarding me the scholarship to undertake this research project. I would like to thank Prof. Muetze of Graz University of Technology and Prof. Joseph Ojo of Tennessee Technological University for introducing me to the Marshall Plan Scholarship. I greatly appreciate the guidance given to me by Ass.Prof. Roland Seebacher and Ass.Prof. Klaus Krischan during the course of the research.

I would like to express my gratitude to Andrew of the Office of International Education and Amy Miller of the Study Abroad office of Tennessee Technological University for the immigration support and travel grant respectively. My research would not have been possible but for your support.

To Heinrich, Christiane and Madeleine, with whom I shared the same office, I appreciate the many conversations we had- spanning all kinds of subjects. Your friendship is very much appreciated. I hope to meet you again someday. To Thomas and Hannes, I enjoyed the conversations we had during my stay there. I cannot forget Helga for all the help you provided me. Thank you all for the interactions and support.

I am profoundly grateful to members of the International Office in Graz University of Technology for all the help and support during my stay. My stay would not have been successful but for you services.

I deeply appreciate the support and prayers of my family and friends during my stay in Austria.

Research Topic:

Evaluation of Model Predictive Control Schemes for Inverter Driven Induction Machines Including Low Loss Sine Filters

Table of Content

CHAPTER 1
INTRODUCTION TO RESEARCH

1.1 INTRODUCTION

Voltage source inverters driving electric machines (Fig. 1) are widely used in all branches of industry, as well as in household and automotive applications spanning over a large power range. A precise and accurate control of electric machine state variables has been of immense concern to industry in recent years [1]. Among the various control strategies proposed in industrial application of induction machines, Direct Torque Control and Field Oriented Control are the two most commonly used [2]-[4]. Despite their widespread use, these methods suffer from some major drawbacks. Direct Torque Control for instance is known to suffer from high torque ripples and operate with a variable switching frequency [5], [6]. Field Oriented Control on the other hand requires an additional modulation block in the control structure [7].

Model Predictive Control has been proposed as a direct competitor to both Direct Torque Control and Field Oriented Control and is attracting a lot of attention in industry and academia [8]—[112]. Model Predictive Control boast of conceptual simplicity and fast dynamic response. Various Model Predictive Control strategies have been proposed in literature. These strategies can be categorized into two groups: Finite and Continuous control set Model Predictive Control. Because of the numerous advantages of Model Predictive Control reported in literature, it is a good candidate for further research.

The control method notwithstanding, aside from the intended (fundamental) component of the inverter output voltage, a certain amount of harmonic content is always present due to the operating principles of such inverters [13]. Fig. 2 shows the rms-value of the harmonics for an inverter using sinusoidal or space vector pulse width modulation in dependence of the modulation index. While modulation algorithms and control strategies may change the output voltage waveforms, the rms value of the harmonics remain nearly constant, as long as the low frequency component remains sinusoidal.

The Inverter output voltage harmonics cause additional losses in the machine, overvoltage peaks at the machine terminals, reduce the machine insulation life time expectancy and may cause issues regarding electromagnetic interference [13], [14]. By proper dimensioning of the drive system, the cabling layout and machine insulation, these issues can nowadays be handled quite well, sometimes by limiting the output power and/or the operating temperature of the machine, when compared with operation at sinusoidal supply.

To overcome some or all of the above mentioned drawbacks, dv/dt filters, reducing the very high frequency harmonic components only, or sine filters are discussed and installed in some applications. Both types of filters basically consist of an LC filter, with dimensioning of the components according to the frequency range to be filtered [15]. The series inductances introduce some voltage drop, reducing the overall utilisation of the drive system whereas the parallel capacitances further increase the number of state variables in the system and introduce possible resonances together with the filter inductance as well as with the machine inductances. The standard approach for dealing with these resonances is to introduce damping resistances [16]. Unfortunately, this increases the system losses and the circuit complexity.

One of the challenges during filter design is to place the resonance frequencies into ranges with the least probabilities of the presence of excitation signals to cause resonance. Sometimes this is only possible by reducing the controller dynamics, thus heavily influencing the dynamic performance of the drive system.

As an alternative to introducing damping resistance into the filter circuitry, active damping by the control can be considered [17]-[19]. To achieve this, control of the filter states, given by the inductance currents and the capacitance voltages, is needed. As a consequence, these filter state variables need to be measured or observed, again increasing the complexity of either the hardware or the control algorithm. Controlling the filter states adds up to the control of the machine states, given by stator currents, rotor flux linkages and the speed.

Model Predictive Control is well suited for the control design complexity introduced by the addition of filters at the output of the converter due to its ability to handle multi-input-multi-output systems with embedded constraints. Despite the inherent advantages of using Model Predictive Control, there are still many challenges associated with their implementation, hence the need for further research.

Model Predictive Control relies on linear models of the system. The accuracy of the linear model may affect the performance of the system. These models are heavily reliant on an accurate determination of the parameters of the system. In induction machine, there is some level of uncertainty in determining the parameters of the machine since the parameters are heavily dependent on the operating conditions of the machine. Also, the complexity of the matrix computation could affect the performance of the system. This is particularly critical when considering an inverter driven Induction Machine with input sine loss filter because of the additional states introduced by the filter.

This work evaluates the performance of existing Model Predictive Control Schemes with regards to computational efficiency and parameter uncertainty. The best scheme is selected and used as basis to design a controller for inverter driven induction machine with sine loss filters. The performance of the designed controller is assessed based on its computational efficiency and robustness against parameter uncertainty.

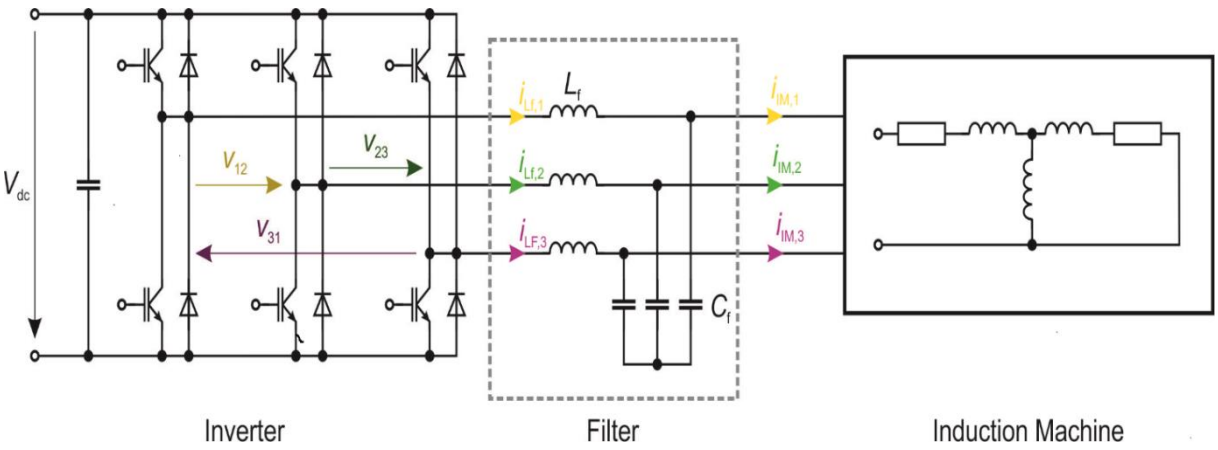

Fig. 1. Structure of the voltage source inverter driven induction machine, including the (optional) sine filter (dashed rectangle).

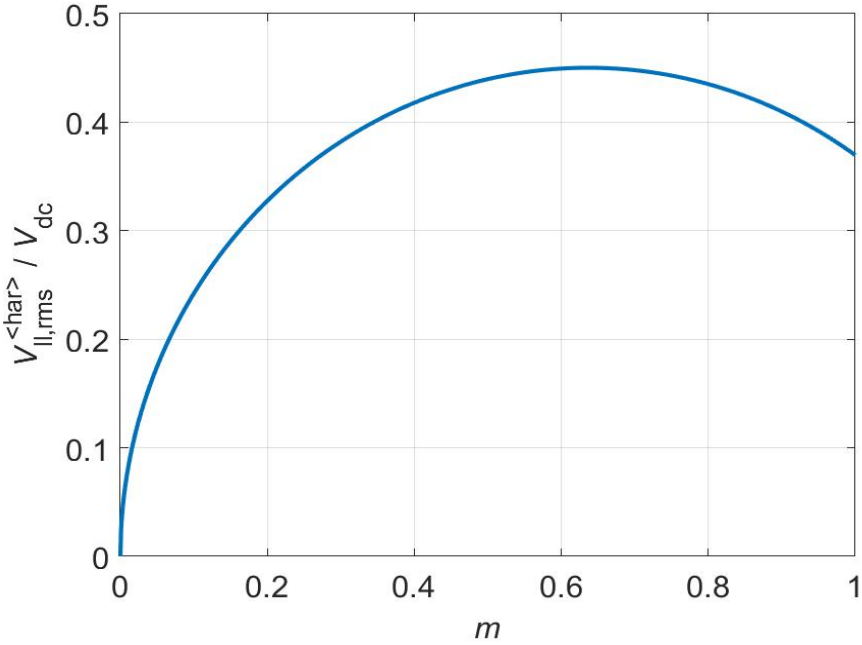

Fig. 2. Output voltage harmonics rms value (scaled by the dc-link voltage) in dependence of the modulation index m

1.2 LITERATURE REVIEW

In the following sections, the state of Model Predictive Control is examined. The different Model Predictive |Control schemes applied to electric machine drive system are introduced and the relevant literature dealing with issues concerning computational efficiency and robustness against parameter uncertainty discussed.

1.2.1 MODEL PREDICTIVE CONTROL

Implementation of Model Predictive Control relies on a mathematical model of the system under control. These models were initially obtained by finite impulse response or step response of the system. However, the finite impulse response and step response are limited to stable systems and the resulting model order are generally high. Transfer function based models were later developed but are considered less effective in handling multivariable systems. For electric machine control, an explicit mathematical model of the machine and converter system is derived and a state space formulation of the model applied in the controller implementation. The general principle of Model Predictive Control is to predict the future evolution of a system based on the current state of the system and the derived dynamic equations of the system. The states are then optimized to achieve a particular control objective and the inputs needed to achieve that objective are computed and applied to the system under control at a future time. At every sample time the future trajectory of the system is predicted over a finite future time known as the prediction horizon. Future control input signals needed to achieve the future trajectory is computed. The number of samples of the control inputs needed to capture the future control trajectory is termed as the control horizon. Even though a number of future control inputs required are computed, only the current control input is applied in the machine control in what is known as receding horizon control.

The two main Model Predictive Control schemes applied to induction machine control, in literature, are Continuous Control Set Model Predictive Control and Finite Control Set Model Predictive Control[20]-[21]. In the next two sections, these two schemes are explained.

1.2.2 CONTINUOUS CONTROL SET MODEL PREDICTIVE CONTROL

Continuous Control Set Model Predictive Control uses a modulator to synthesize the inverter states. Because of the presence of the modulator, Continuous Control Set Model Predictive Control operates with a constant switching frequency. The control input that optimizes a predefined objective function is obtained and passed on to the modulator to obtain the switching states. One unique aspect of model predictive control is its ability to utilize a long-range prediction horizon. This allows the current control input to take into account the future evolution of the system. Where a prediction horizon greater than one is used, even though it is possible to calculate several control inputs (control horizon), only the first input is applied to the modulator.

1.2.3 FINITE CONTROL SET MODEL PREDICTIVE CONTROL

In Finite Control Set Model Predictive Control, the inverter switching states are directly synthesized by the controller. Therefore, finite control set model predictive control does not require a modulator as the outputs of the controller are directly applied to the inverter. Because of this, the switching frequency of finite control set model predictive control is not constant. This may have adverse effects when it comes to the design of output filters for the inverter. The control algorithm for finite control set model predictive control takes advantage of the fact that an inverter has a finite number of states (there are only eight possible switching combinations for a voltage source inverter). In the case of finite control set model predictive control, as opposed to continuous control set model predictive control, all the possible voltage vectors at a given frequency are applied as inputs to the objective function. The voltage vector that optimizes the objective function is selected and the switching states needed to synthesize the voltage vector directly obtained.

CHAPTER 2
INDUCTION MACHINE MODEL

Induction Machines are widely used in industry for converting electrical energy to mechanical energy (motoring) or vice versa (generating). The development of different control methods has made it possible to drive the induction machine to achieve any given objective. In this chapter, the principle of operation of an induction machine is explained.

Model Predictive Controller Design relies on the accuracy of the derived model of the system. In order to design the controller, therefore, a model of the induction machine is derived. The derived model is transformed from the normal abc frame to the qdo frame using Park's Transform. The derived model is validated using Matlab/Simulink environment and the results compared with a complex vector calculation.

Model Predictive Control is based on the linearized model of the system. Therefore, the induction machine model is linearized around the steady-state operating points using Taylor series expansion. Implementation of the controller will be done on a digital platform. In order to achieve that, a digitized version of the system state space model is obtained.

2.1 PRINCIPLE OF OPERATION OF AN INDUCTION MACHINE

The winding arrangements of a two-pole, three-phase symmetrical induction machine is shown in fig. 3. The windings in the stator are identical- having equivalent number of turns and resistances. The rotor of an induction machine may be wound rotor or squirrel cage. The rotor may be approximated by equivalent windings with a given number of turns and resistance. The air gap of the induction machine is assumed uniform.

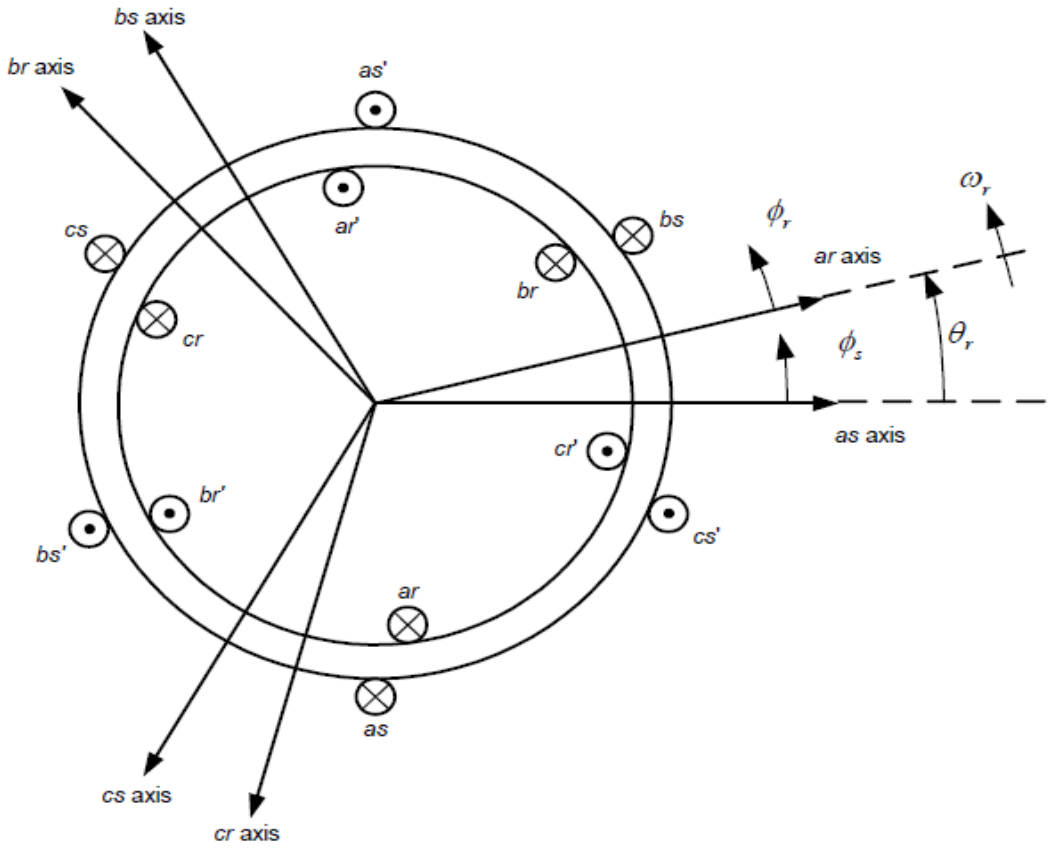

Fig. 3. Winding arrangements of a two-pole, three-phase symmetrical induction machine

The induction machine is normally operated by connecting the stator windings to a balanced three-phase voltage source. A balance three-phase current is generated in the stator windings. The stator windings are sinusoidally distributed with a 120 electrical degree phase shift. The stator currents produce a rotating magneto-motive force in the air gap. The speed of rotation of the air gap flux is given by:

$$\omega_e = \frac{P}{2}\omega_m$$

Where P is the number of poles, ω_e is the electrical speed and ω_m is the mechanical speed all in radians per second. According to Lenz's law, when the rotor speed is different from the electrical speed, three-phase currents are induced in the rotor windings to oppose the change of flux linkages between the rotor and flux. The frequency of rotation of the current in the rotor windings is given by the difference between the electrical speed, ω_e and the rotor speed ω_r, and is known as the slip frequency.

An air gap flux is generated by the induced rotor current. The air gap magneto-motive force generated by the rotor rotates at the same frequency as that generated by the stator. These two magneto-motive forces interact with each other to produce a torque. The rotor speed has to be different from the electrical speed of the machine, otherwise current cannot be induced in the rotor and hence no torque can be produced by the machine. If the rotor frequency is greater than the electrical frequency, then the induction machine is said to be generating. If the rotor frequency is less than the electrical frequency, then the induction machine is motoring.

2.2 OPEN LOOP MODELLING AND EVALUATION

In this section the open loop model of the induction machine and the inverter system is developed. In order to apply model predictive control (MPC) to an induction machine, it is essential to accurately model the induction since the MPC relies on an accurate model of the induction machine. The fundamental equations underlining the operation of an induction machine are well established and can be found in literature [1]. In this report, a brief description of the model is given.

The voltage equations describing the operation of an induction machine in the regular abc frame are given as:

$$v_{as} = r_s i_{as} + \frac{d\lambda_{as}}{dt} \quad (1)$$

$$v_{bs} = r_s i_{bs} + \frac{d\lambda_{bs}}{dt} \quad (2)$$

$$v_{cs} = r_s i_{cs} + \frac{d\lambda_{cs}}{dt} \quad (3)$$

$$v_{ar} = r_r i_{ar} + \frac{d\lambda_{ar}}{dt} \quad (4)$$

$$v_{br} = r_r i_{br} + \frac{d\lambda_{br}}{dt} \quad (5)$$

$$v_{cr} = r_r i_{cr} + \frac{d\lambda_{cr}}{dt} \quad (6)$$

Where r_s and r_r are the resistance of each stator and rotor phase windings respectively. v and λ are the voltage and flux linkage variables respectively. The first and second subscripts represent the phase and winding type the variable belongs.

It is well established that the inductances associated with the voltage equations given above are time varying and therefore make the analysis of the system complex. A change of variable is used to reduce the complexity of the analysis- which leads to the concept of reference frame transformation. The machine variables in the regular abc frame can be transformed to any arbitrary reference frame using the transformation given by:

$$f_{qdo} = Kf_{abc} \tag{7}$$

$$\text{Where} \quad k = \frac{2}{3}\begin{bmatrix} cos\vartheta & \cos(\vartheta - {}^{2\pi}/_{3}) & \cos(\vartheta + {}^{2\pi}/_{3}) \\ \sin\vartheta & \sin(\vartheta - {}^{2\pi}/_{3}) & \sin(\vartheta + {}^{2\pi}/_{3}) \\ {}^{1}/_{2} & {}^{1}/_{2} & {}^{1}/_{2} \end{bmatrix}$$

The equations defining the operation of an induction in the qd synchronous reference frame are given as:

$$v_{qs} = r_s i_{qs} + p\lambda_{qs} + \omega_e \lambda_{ds} \tag{8}$$

$$v_{ds} = r_s i_{ds} + p\lambda_{ds} - \omega_e \lambda_{qs} \tag{9}$$

$$v'_{qr} = r'_r i'_{qr} + p\lambda'_{qr} + (\omega_e - \omega_r)\lambda'_{dr} \tag{10}$$

$$v'_{dr} = r'_r i'_{dr} + p\lambda'_{dr} - (\omega_e - \omega_r)\lambda'_{qr} \tag{11}$$

$$T_e = \frac{3P}{4}\frac{L_m}{L_r}\left(\lambda'_{dr} I_{qs} - \lambda'_{qr} I_{ds}\right) \tag{12}$$

$$p\omega_r = \frac{P}{2J}(T_e - T_l) \tag{13}$$

Where

$$p \; is \; the \; operator \frac{d}{dt}$$

Where

$$\lambda_{qs} = L_{ls} i_{qs} + L_M\left(i_{qs} + i'_{qr}\right)$$
$$\lambda_{ds} = L_{ls} i_{ds} + L_M(i_{ds} + i'_{dr})$$
$$\lambda'_{qr} = L'_{lr} i'_{qr} + L_M\left(i_{qs} + i'_{qr}\right)$$
$$\lambda'_{dr} = L'_{lr} i'_{dr} + L_M(i_{ds} + i'_{dr})$$

Where v_{qs} and v_{ds} are the q and d-axis stator voltages, r_s and r'_r are the stator and rotor referred winding resistance, i_{qs} and i_{ds} are the q and d-axis stator currents, λ_{qs} and λ_{ds} are the q and d-axis stator fluxes, v'_{qr} and v'_{dr} are the q and d-axis rotor referred voltages, i'_{qr} and i'_{dr} are the q and d-axis rotor referred currents, λ'_{qr} and λ'_{dr} are the q and d-axis rotor referred

fluxes, P is the number of poles, ω_e is the electrical angular speed and ω_r is the rotor electrical angular speed.

In the first step the analysis of the inverter system is done without the filter. The output voltage equation of the inverter is given by:

$$V_{ao} = \frac{V_{dc}}{2}(2S_{ap} - 1) \tag{14}$$

$$V_{bo} = \frac{V_{dc}}{2}(2S_{bp} - 1) \tag{15}$$

$$V_{co} = \frac{V_{dc}}{2}(2S_{cp} - 1) \tag{16}$$

$$V_{no} = \frac{1}{3}(V_{ao} + V_{bo} + V_{co}) \tag{17}$$

$$V_{as} = V_{ao} - V_{no} \tag{18}$$

$$V_{bs} = V_{bo} - V_{no} \tag{19}$$

$$V_{cs} = V_{co} - V_{no} \tag{20}$$

Where S_{ap}, S_{bp} and S_{cp} are the switching functions of the upper switches of phases a,b and c respectively. V_{ao}, V_{bo} and V_{co} are the voltages between the inverter legs and the midpoint of the dc-link. V_{no} is the neutral point voltage.

To verify the accuracy of the developed model, a dynamic simulation of the system was carried out in the Matlab/Simulink platform. The parameters used for the simulation are provided in table. 1. Fig. 4 shows the simulation result for the normalised pwm-signal obtained by comparing the modulation signal to a triangular carrier. The modulation index is 0.8. Fig. 5 shows the same pwm signals in Fig. 4 within a shorter timescale.

TABLE 1.

TEST MACHINE PARAMETERS

Parameter	Value
L_m	0.0073
L_{ls}	3.3899× 10^{-4}
L_{lr}	3.3899× 10^{-4}
r_s	0.1706
r_r	0.1000
T_L	0
J	0.0170
P	2
V_{dc}	120
f_{sw}	6kHz

Fig. 6 shows the stator phase “a” current of the induction machine as a function of time. The transient and steady state envelope of the current can be seen from this figure. The envelope of the stator current varies during transient condition due to interaction between stator and rotor electrical transients. Fig, 7 shows the stator phase “a” steady state current of the machine as a function of time. As expected, as a result of the switching action of the inverter, harmonic content can be seen in the current waveform.

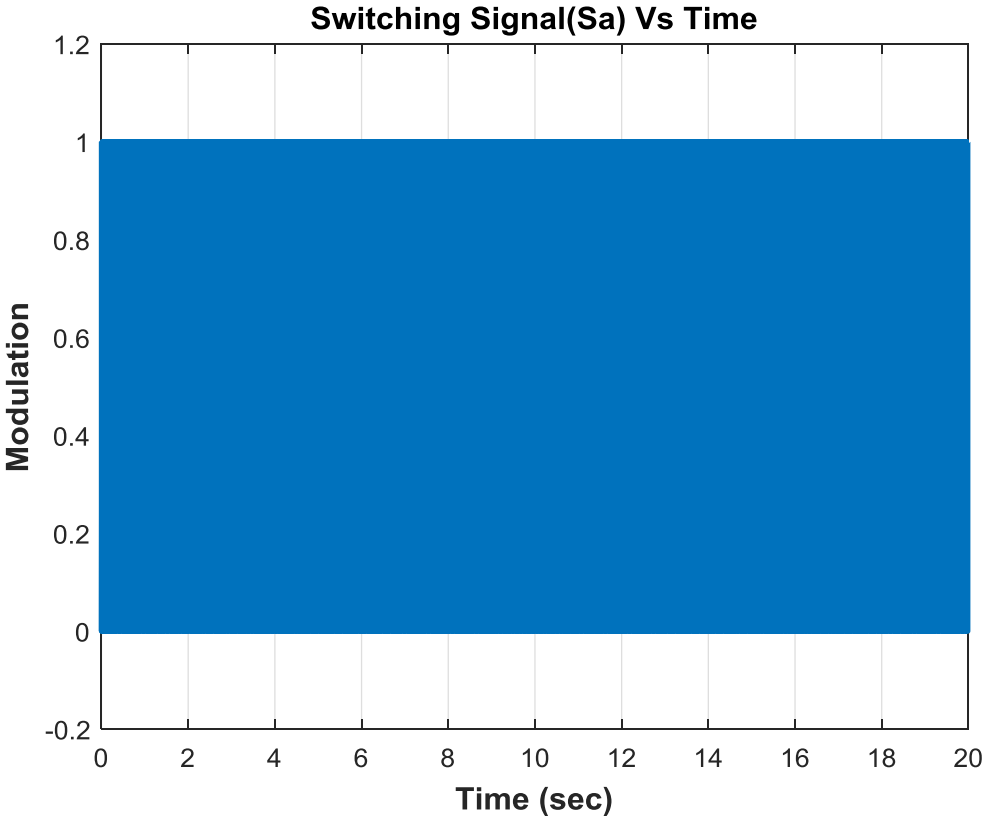

Fig. 4. Normalised PWM signals for inverter control

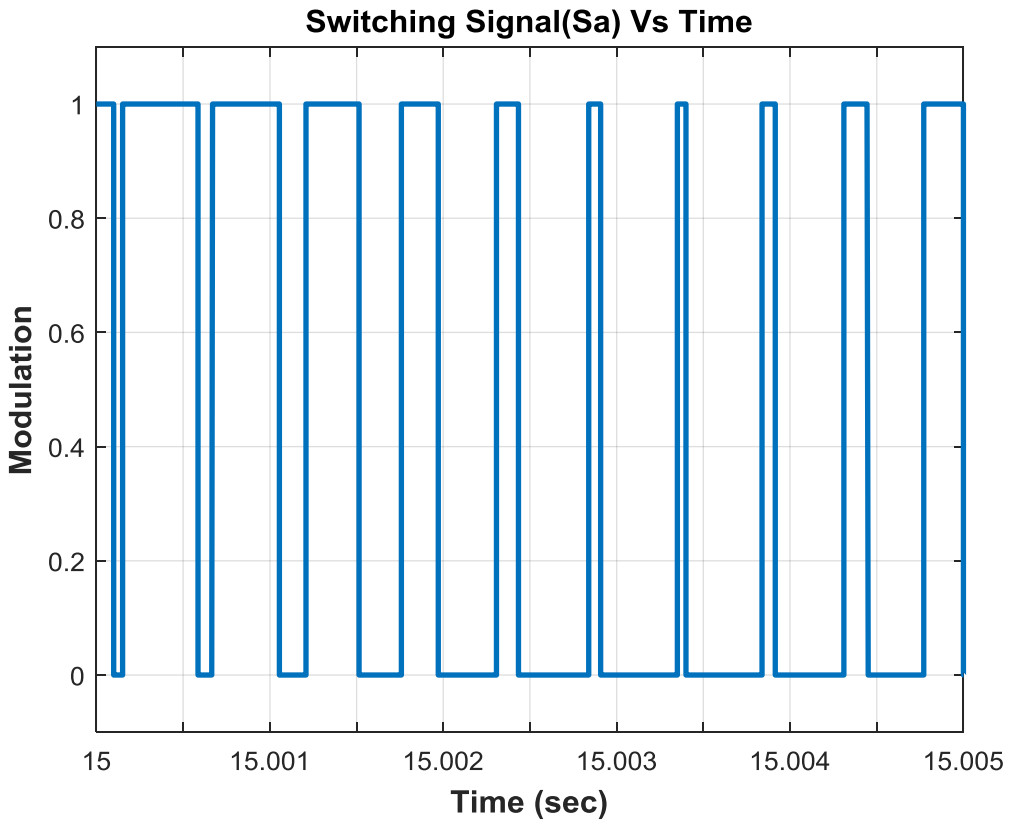

Fig. 5. Normalised PWM signals zoomed in to reveal switching details

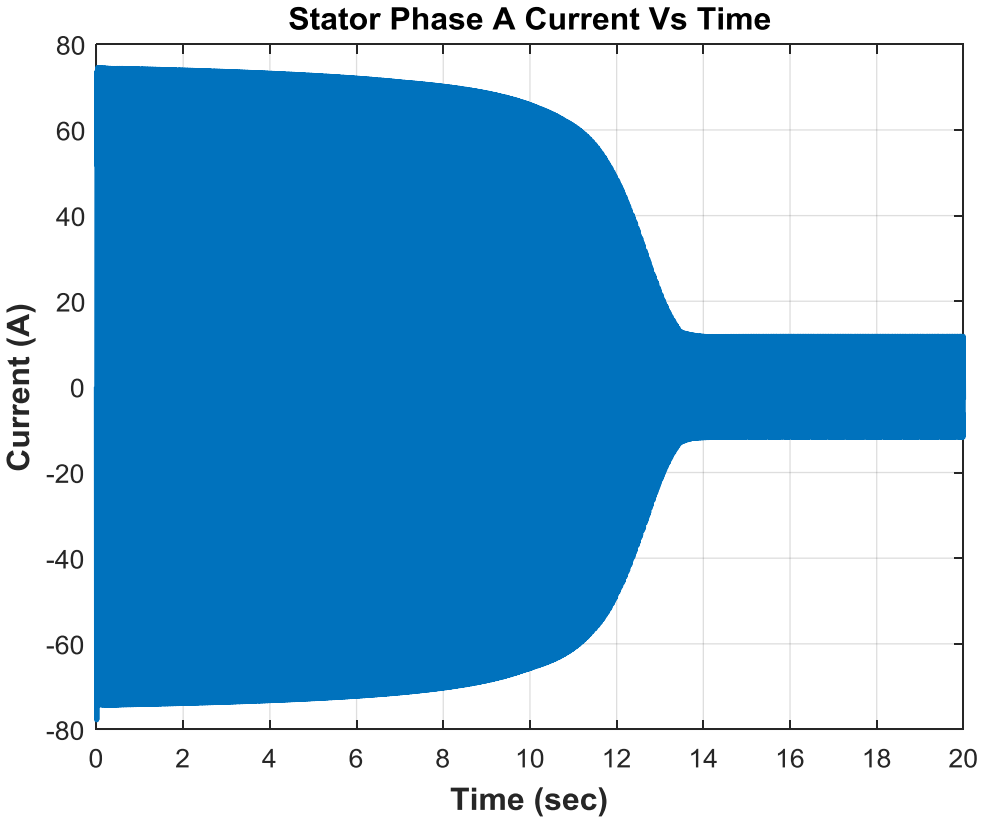

Fig. 6. Stator Phase “a’ current envelope as function of time

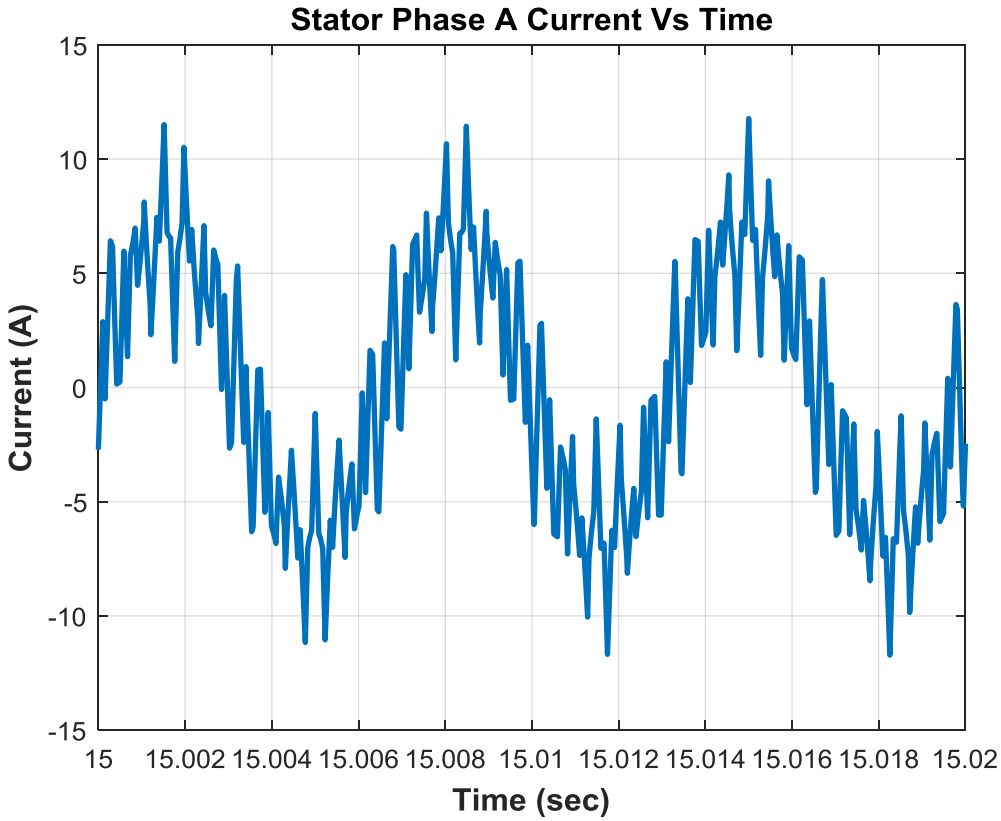

Fig. 7. Steady state phase "a" current waveform as function of time

Fig. 8 and 9 show the dynamic simulation for the q-axis stator flux linkage as a function of time. Fig. 9 gives the steady state stator flux linkage of the machine.

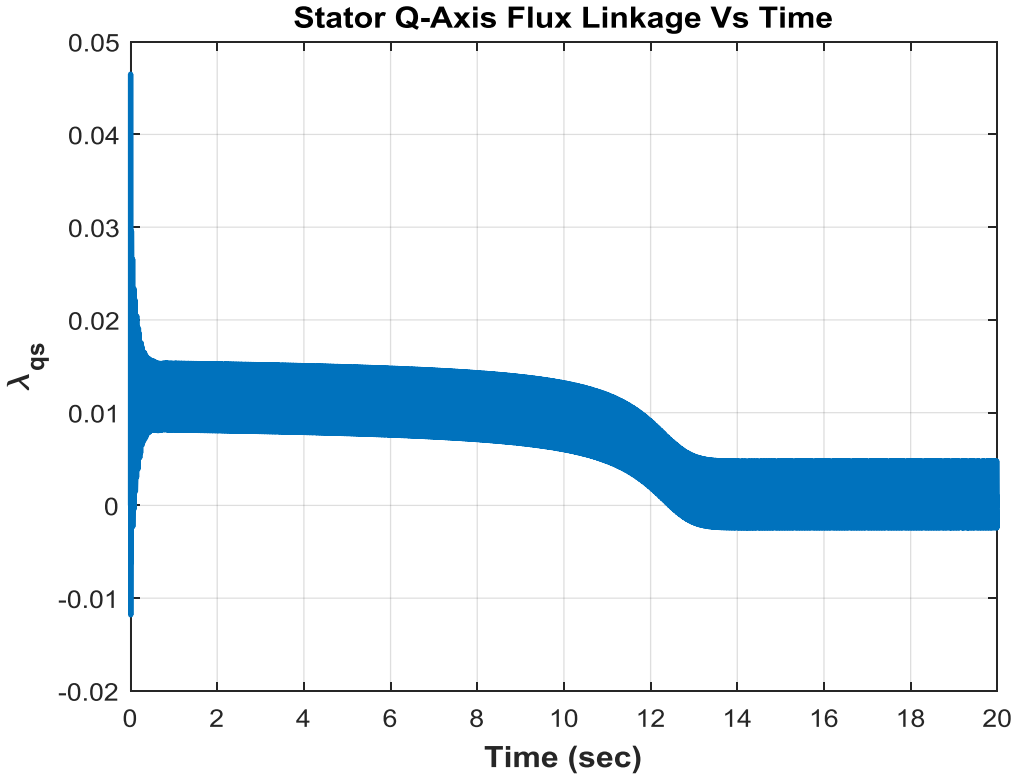

Fig. 8. Transient response of stator q-axis flux linkage as function of time

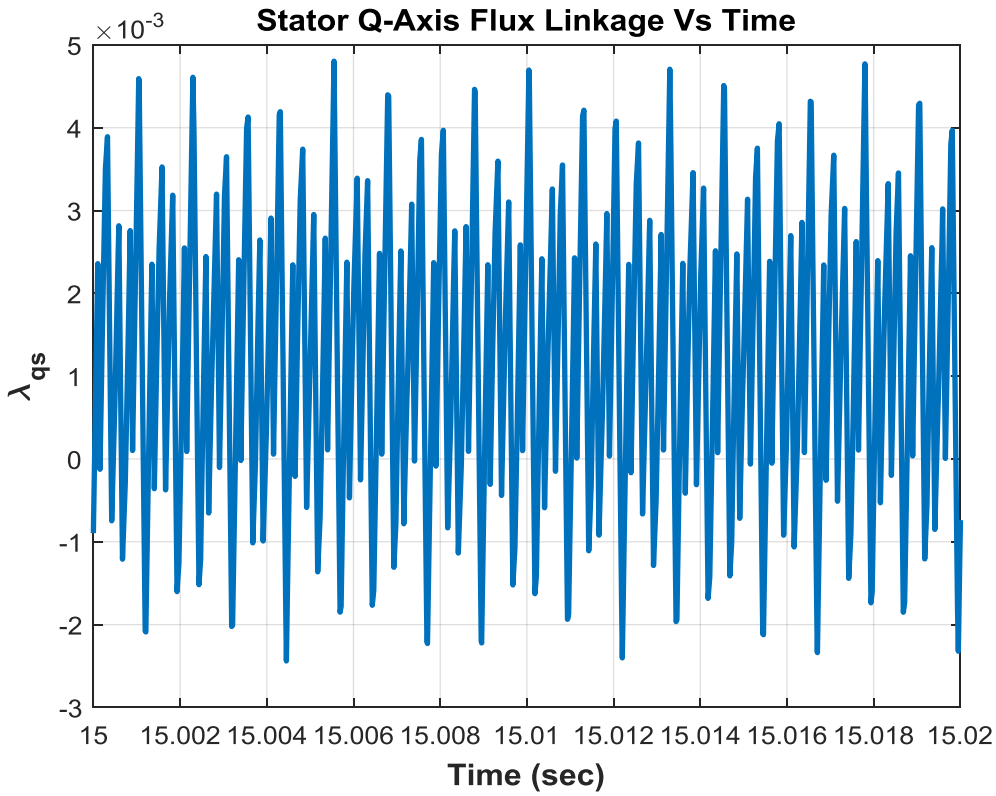

Fig. 9. Stator q-axis flux linkage shown switching ripples

The electromagnetic torque at start has a positive average value as shown in fig. 10. Rated torque is developed close to the synchronous speed, therefore this induction machine is a low slip induction machine.

Fig. 11 shows the rotor electrical angular speed of the induction machine. Because windage losses are not present the machine accelerates to synchronous speed. The machine is low horsepower machine hence the speed of the rotor is easily damped and does not exceed the synchronous speed.

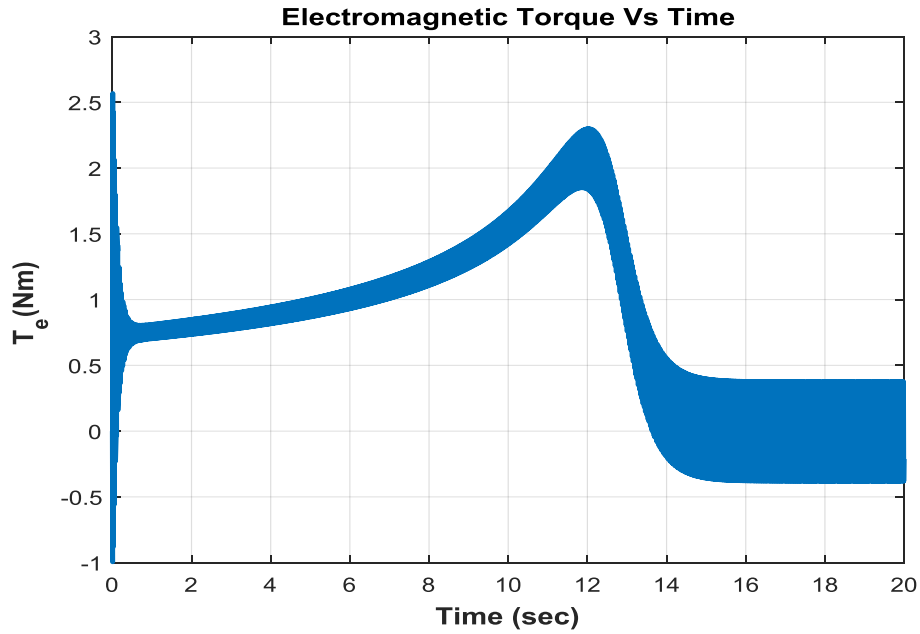

Fig. 10. Electromagnetic torque of induction machine as function of time

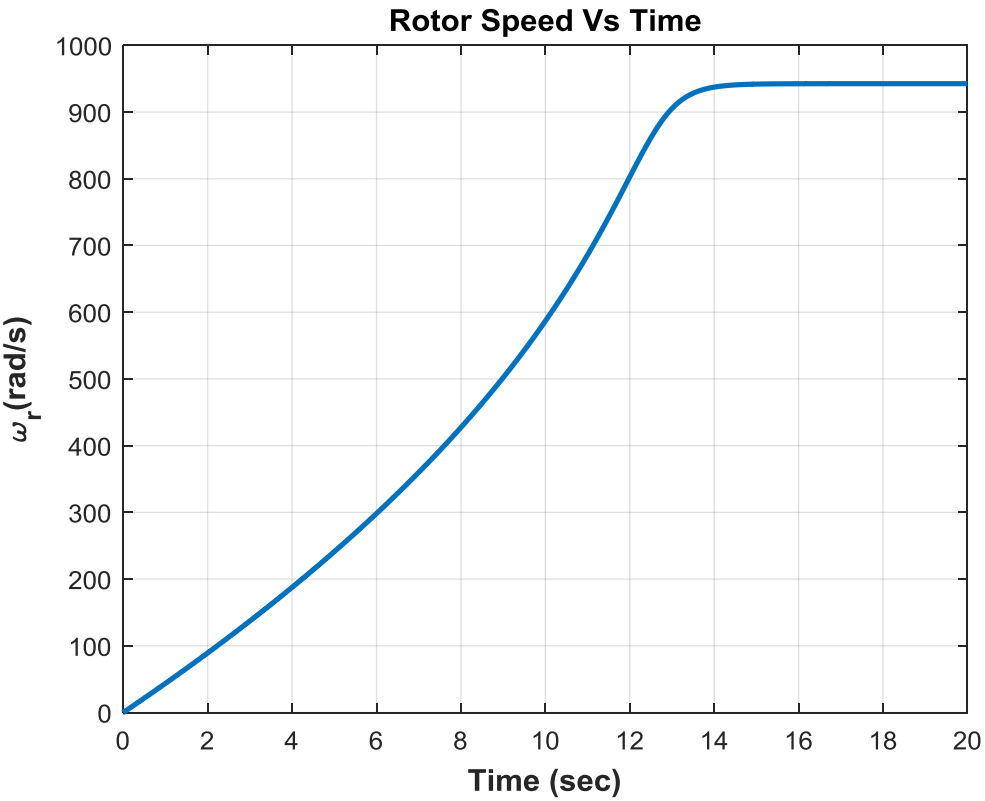

Fig. 11. Rotor electrical angular speed of the induction machine as a function of time.

In order to ascertain the accuracy of the model developed, the simulation results were compared with a complex vector calculation of the steady state values of the machine states. The complex vector calculation is presented as follows:

At steady state

$$v_{qds} = r_s i_{qds} + j\omega_e \lambda_{qds} \tag{21}$$

$$v'_{qdr} = r'_r i'_{qdr} + (\omega_e - \omega_r)\lambda'_{qdr} \tag{22}$$

$$v_{qds} = r_s i_{qds} + j\omega_e \lambda_{qds}$$

$$v'_{qdr} = r'_r i'_{qdr} + (\omega_e - \omega_r)\lambda'_{qdr}$$

If the machine is operating at synchronous speed then,

$$\omega_e = \omega_r = 2\pi 150 = 942.48$$

$L_r = L_s = 7.639 \times 10^{-3}, r_r = 0.10, r_s = 0.1706$

$$\lambda_{qds} = L_{ls} i_{qds} + L_M\left(i_{qds} + i'_{qdr}\right) \tag{23}$$

$$\lambda'_{qdr} = L'_{lr} i'_{qdr} + L_M\left(i_{qds} + i'_{qdr}\right) \tag{24}$$

$$v_{qs} = 48cos0 = 48$$

$$v_{ds} = 48sin0 = 0$$

$v_{qds} = 48, v'_{qdr} = 0$

$$\lambda_{qds} = 7.639 \times 10^{-3} i_{qds} + 0.0073 i'_{qdr}$$

$$\lambda'_{qdr} = 7.639 \times 10^{-3} i'_{qdr} + 0.0073 i_{qds}$$
$$48 = (0.1706 + j7.2) i_{qds} + 6.88 i'_{qdr}$$
$$0 = 0.10 i'_{qdr} + j0 i_{qds}$$
$$i'_{qdr} = 0$$
$$i_{qds} = \frac{48}{(0.1706 + j7.2)}$$
$$i_{qds} = 0.158 - j6.66$$
$$i_{qs} = 0.158$$
$$i_{ds} = 6.66$$
$$T_e = \frac{3P}{4} L_m \left(i'_{dr} i_{qs} - i'_{qr} i_{ds}\right) = 0$$

2.3 DYNAMIC MODEL OF INDUCTION MACHINE FOR MODEL PREDICTIVE CONTROL

Model Predictive Control relies on state space model of the system to be controlled. In this section the state space model of the induction machine is derived beginning with the qd model of the machine obtained in previous sections. The voltage equations of the induction machine are repeated here for completeness:

$$v_{qs} = r_s i_{qs} + p\lambda_{qs} + \omega_e \lambda_{ds}$$
$$v_{ds} = r_s i_{ds} + p\lambda_{ds} - \omega_e \lambda_{qs}$$
$$v'_{qr} = r'_r i'_{qr} + p\lambda'_{qr} + (\omega_e - \omega_r)\lambda'_{dr}$$
$$v'_{dr} = r'_r i'_{dr} + p\lambda'_{dr} - (\omega_e - \omega_r)\lambda'_{qr}$$

The rotor currents of the induction machine are not know and can be replaced with the rotor flux linkages and stator currents using the following substitutions:

$$\lambda'_{qr} = L'_{lr} i'_{qr} + L_M \left(i_{qs} + i'_{qr}\right)$$
$$\lambda'_{dr} = L'_{lr} i'_{dr} + L_M (i_{ds} + i'_{dr})$$

Depending on the variables selected as the states of the system, the voltage equations can be reduced further. In this research, the stator currents and rotor fluxes are selected as the states of the system. The stator flux linkages are therefore replaced by the rotor flux linkages and stator currents using:

$$\lambda_{qs} = L_{ls} i_{qs} + L_M \left(i_{qs} + i'_{qr}\right)$$
$$\lambda_{ds} = L_{ls} i_{ds} + L_M (i_{ds} + i'_{dr})$$

After performing the appropriate substitutions, the voltage equations can be rewritten in the form:

$$v_{qs} = L_\sigma p i_{qs} + r i_{qs} + \omega_e L_\sigma i_{ds} - \frac{r'_r L_M}{L_r^2} \lambda_{qr} + \omega_r \frac{L_M}{L_r} \lambda_{dr} \quad (25)$$

$$v_{ds} = L_\sigma p i_{ds} + r i_{ds} - \omega_e L_\sigma i_{qs} - \frac{r'_r L_M}{L_r^2} \lambda_{dr} - \omega_r \frac{L_M}{L_r} \lambda_{qr} \quad (26)$$

$$0 = p\lambda_{qr} + \frac{r_r}{L_r} \lambda_{qr} - \frac{r_r L_M}{L_r} i_{qs} + (\omega_e - \omega_r)\lambda_{dr} \quad (27)$$

$$0 = p\lambda_{dr} + \frac{r_r}{L_r}\lambda_{dr} - \frac{r_r L_M}{L_r} i_{ds} - (\omega_e - \omega_r)\lambda_{qr} \tag{28}$$

$$p\omega_r = \frac{P}{2J}(T_e - T_L) \tag{29}$$

Where $L_\sigma = L_s - \frac{L_m^2}{L_r}$ and $r = r_s + \frac{r_r L_m^2}{L_r^2}$

For actual implementation, obtaining the rotor flux is a difficult task. In general, the rotor flux linkages are not directly measured and need to be estimated from the measured states. In actual implementation, the stator currents and speed/position of the motor are measured. There has also been the development of sensorless control methods in recent times, in which case speed is not measured but estimated. To obtain the rotor flux linkages, estimation is done from the measured states or observers are designed to obtain the flux linkages. The direct approach is to compute the stator flux linkages by integrating the back EMF of the induction machine from the stator voltages and currents in the stationary reference frame, i.e.

$$\lambda_{qs} = \int (v_{qs} - r_s i_{qs})\, dt \tag{30}$$

$$\lambda_{ds} = \int (v_{ds} - r_s i_{ds})\, dt \tag{31}$$

Since the signals are in the stationary reference frame, they are AC signals. Integration of AC signals can lead to saturation and drift problems. This is because it is not realistic to start the integration when the integrated signal is exactly at zero. This is called the initial condition problem and it results in a DC component after integration. Also, the signal itself is not pure AC signal and it has DC component. The average value of the integrated signal is not zero due to the distortion of the signal itself and the resolution of the sensors. The existing DC offset will drift the integration result to saturation. Finally, the frequency of the integrated signal is not high enough especially during the starting. This will make integration result to saturation even if the magnitude of the signal to be integrated is very small.

To solve the problems, the pure integrator is replaced by a low pass filter. The transfer function of a low pass filter is $s + a$ compared with that of a pure integrator with transfer function s.

By using the low pass filter, the small DC offset in the integrated signals cannot cause saturation although the estimated values are not correct at the very beginning. The DC offset in the outputs introduced by the initial values is also mitigated. But there still exists the magnitude and phase errors due to the introduction of a (cut-off frequency) especially when a is relatively big, which is generally the case to get a good performance for the low pass filter. The gain and phase differences in the final results are therefore compensated for. From the stator flux linkages and stator currents, the rotor flux linkages are computed.

If the rotor flux is aligned with the d-axis of the synchronous reference frame, then:

$$\lambda_{qr} = 0$$

$$\lambda_{dr} = \lambda_r$$

The machine equations become:

$$v_{qs} = L_\sigma p i_{qs} + r i_{qs} + \omega_e L_\sigma i_{ds} + \omega_r \frac{L_M}{L_r} \lambda_r \tag{32}$$

$$v_{ds} = L_\sigma p i_{ds} + r i_{ds} - \omega_e L_\sigma i_{qs} - \frac{r_r' L_M}{L_r^2} \lambda_r \tag{33}$$

$$0 = -\frac{r_r L_M}{L_r} i_{qs} + (\omega_e - \omega_r)\lambda_r \tag{34}$$

$$0 = p\lambda_{dr} + \frac{r_r}{L_r}\lambda_{dr} - \frac{r_r L_M}{L_r} i_{ds} - (\omega_e - \omega_r)\lambda_r \tag{35}$$

$$p\omega_r = \frac{2}{J}(T_e - T_L) \tag{36}$$

One advantage of Model Predictive Control over traditional PID controller is its fast response to step changes. Therefore, in the control architecture, PID can be used for the control of the variables with slow response whilst variables requiring a fast response are controlled using Model Predictive Control, In this regard, for the design of the Model Predictive Controller, it is assumed that the speed and rotor flux are kept at a constant reference value because of their slow dynamics. The dynamic equations of the machine reduced to a form which can be written as:

$$p i_{qs} = -\frac{r}{L_\sigma} i_{qs} - \omega_e i_{ds} - \frac{\omega_r L_M}{L_\sigma L_r}\lambda_r + \frac{v_{qs}}{L_\sigma} \tag{37}$$

$$p i_{ds} = \omega_e i_{qs} - \frac{r}{L_\sigma} i_{ds} + \frac{r_r L_M}{L_\sigma L_r^2}\lambda_r + \frac{v_{ds}}{L_\sigma} \tag{38}$$

The state-space model of the system from the above equations can be derived and are given as shown below:

$$\begin{bmatrix} p i_{ds} \\ p i_{qs} \end{bmatrix} = \begin{bmatrix} -\frac{r}{L_\sigma} & \omega_e \\ -\omega_e & -\frac{r}{L_\sigma} \end{bmatrix} \begin{bmatrix} i_{ds} \\ i_{qs} \end{bmatrix} + \begin{bmatrix} \frac{1}{L_\sigma} & 0 \\ 0 & \frac{1}{L_\sigma} \end{bmatrix} \begin{bmatrix} v_{ds} \\ v_{qs} \end{bmatrix} + \begin{bmatrix} -\frac{\omega_r L_M}{L_\sigma L_r}\lambda_r \\ \frac{r_r L_M}{L_\sigma L_r^2}\lambda_r \end{bmatrix} \tag{39}$$

The designed controller is implemented on a digital platform. The equations obtained above are therefore digitized using Euler method and the discrete state space model is derived. The stator currents at the next sampling instant are predicted as:

$$x(k+1) = Ax(k) + Bu(k) + D \tag{40}$$

Where

$$A = \begin{bmatrix} 1 - T_s \frac{r}{L_\sigma} & \omega_e \\ -\omega_e & 1 - T_s \frac{r}{L_\sigma} \end{bmatrix}$$

$$B = \begin{bmatrix} T_s \frac{1}{L_\sigma} & 0 \\ 0 & T_s \frac{1}{L_\sigma} \end{bmatrix}$$

$$D = \begin{bmatrix} -T_s \dfrac{\omega_r L_M}{L_\sigma L_r} \lambda_r \\ T_s \dfrac{r_r L_M}{L_\sigma L_r^2} \lambda_r \end{bmatrix}$$

T_s is the sampling period of the digital system.

CHAPTER 3

Finite Control Set Model Predictive Control

In finite control set model predictive control, the discrete nature of inverter states is taking into account in the control implementation. In a two level voltage source inverter, there are only eight possible combinations of inverter switching states, hence the name finite control set. In this control scheme the inverter states are directly synthesized without the need for a pulse width modulator.

For a voltage source inverter, the possible combination of switching states is obtained as follows:

In the two level inverter shown in fig. 12, the switches in the upper leg are complementary to their corresponding switches in the lower half. The switching modes of a voltage source inverter and the corresponding voltages in the stationary reference frame can be found by using Clarke's transformation. Clarke's transformation for a three-phase voltage is given as:

$$\begin{bmatrix} v_\alpha \\ v_\beta \end{bmatrix} = \frac{2}{3}\begin{bmatrix} 1 & -\frac{1}{2} & -\frac{1}{2} \\ 0 & \frac{\sqrt{3}}{2} & -\frac{\sqrt{3}}{2} \end{bmatrix}\begin{bmatrix} v_{an} \\ v_{bn} \\ v_{cn} \end{bmatrix} \tag{41}$$

The voltages in the stationary reference frame can be expressed in terms of the switching functions of the switches in the upper half phase leg. The result is given in (42).

$$\begin{bmatrix} v_\alpha \\ v_\beta \end{bmatrix} = \frac{2}{3}V_{dc}\begin{bmatrix} 1 & -\frac{1}{2} & -\frac{1}{2} \\ 0 & \frac{\sqrt{3}}{2} & -\frac{\sqrt{3}}{2} \end{bmatrix}\begin{bmatrix} S_{ap} \\ S_{bp} \\ S_{cp} \end{bmatrix} \tag{42}$$

To take into account the position of the voltage vector at a given frequency, the voltage is converted from stationary reference frame to the synchronous reference frame using the Clarke to Parke transformation and is given as:

$$\begin{bmatrix} v_q \\ v_d \end{bmatrix} = \begin{bmatrix} -sin\theta_e & cos\theta_e \\ cos\theta_e & sin\theta_e \end{bmatrix}\frac{2}{3}V_{dc}\begin{bmatrix} 1 & -\frac{1}{2} & -\frac{1}{2} \\ 0 & \frac{\sqrt{3}}{2} & -\frac{\sqrt{3}}{2} \end{bmatrix}\begin{bmatrix} S_{ap} \\ S_{bp} \\ S_{cp} \end{bmatrix} \tag{43}$$

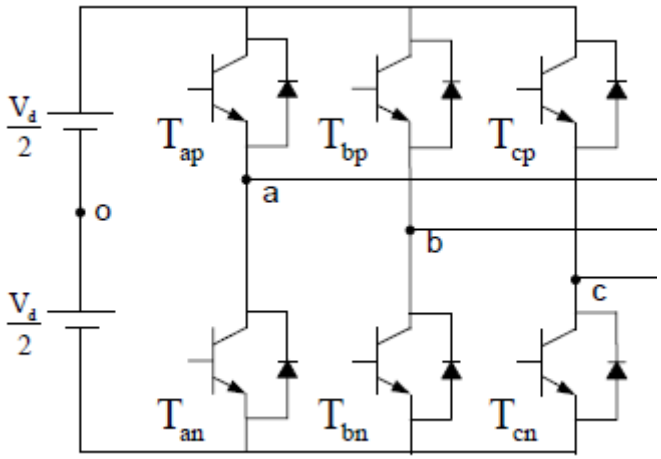

Fig. 12. Two level voltage source inverter.

Where $\frac{d\theta_e}{dt} = \omega_e$

By these derivations, the trajectory of the control signal with respect to the angle θ_e is obtained in the synchronous reference frame.

The derivation of the voltages above shows that, without the use of a pulse width modulator, there are only eight possible choices for the input signal. The eight sets of v_q and v_d at a given sampling time form the candidates for a finite control set.

The next step is to define an objective function to reflect the purpose of the controller design in order to obtain which pair of input signals to use. For the control of the q and d axis currents, the objective function in this work is defined as the squared error between the desired currents and the predicted currents. The objective function is mathematically expressed as:

$$J(k) = \big(e(k+1)\big)^T \big(e(k+1)\big) \tag{44}$$

Where $e(k+1)$ is the one step ahead predicted error state given as:

$$e(k+1) = x^*(k) - x(k+1) \tag{45}$$

and $x^*(k)$ is the reference states.

In a digital implementation of the control algorithm, for every sampling instant, there are eight pairs of inputs available for optimization of the objective function. In the finite control set model predictive controller, the next step is to find the pair of input voltage vectors that will optimize the objective function. This is done by calculating the eight possible objective functions base on the eight pairs of input voltage vectors at a given sampling time instant. The voltage pair that gives the minimum value of the objective function is selected and based on which the switching function is determined. When the zero voltage vectors gives the minimum value of the objective function, it is necessary to decide which of the two voltage vector switching states to apply to the inverter. The choice is based on the zero vector that will produce the least number of changes in switching states. In that case, it is essential to take into consideration the previous switching states of the inverter.

At the next sampling instant, the currents and speed of the induction machine are measured and the angular location of the vector obtained. Based on which the eight pairs of voltage vectors are computed and the optimization process carried out.

The control gain of the finite control set model predictive controller is determined by the sampling frequency. To achieve good performance characteristics from this controller, the sampling frequency should be kept as high as possible. At very low sampling frequency, the finite control set controller fails to achieve satisfactory performance. The choice of sampling frequency is therefore critical to the stability of the designed controller.

The graphs below show the response of the control system to various reference signals. Fig. 13 shows the response of the current controller to a reference current $I_{ds} = 10$ and a step change in the q-axis current from zero to twenty-five and then from twenty-five to zero at time steps 0.5s and 1.3s respectively. As can be seen, the output current tracks the given reference as desired. The q and d-axis current computed from the observer were compared with those obtained directly from the model to show the effectiveness of the designed observer. At zero torque the observer is able to calculate the actual q and d-axis currents. As can be seen from fig. 13, when I_{qs} is increased from zero to twenty-five (which represents an increase in the electromagnetic torque), the current ripple is observed to increase accordingly. Fig. 14 shows the ripples in the q-axis current at 25A. A ripple of 1.4A can be observed.

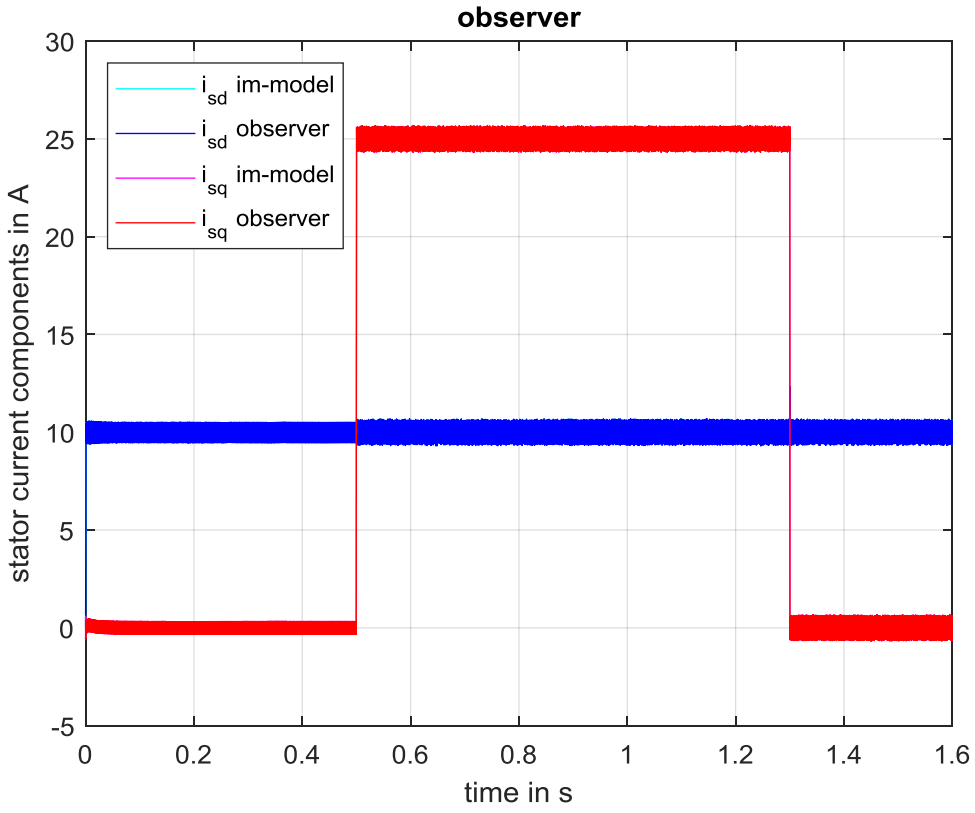

Fig. 13. Simulation results showing the estimated q and d axis currents by the observer and their respective values as obtained from the machine model.

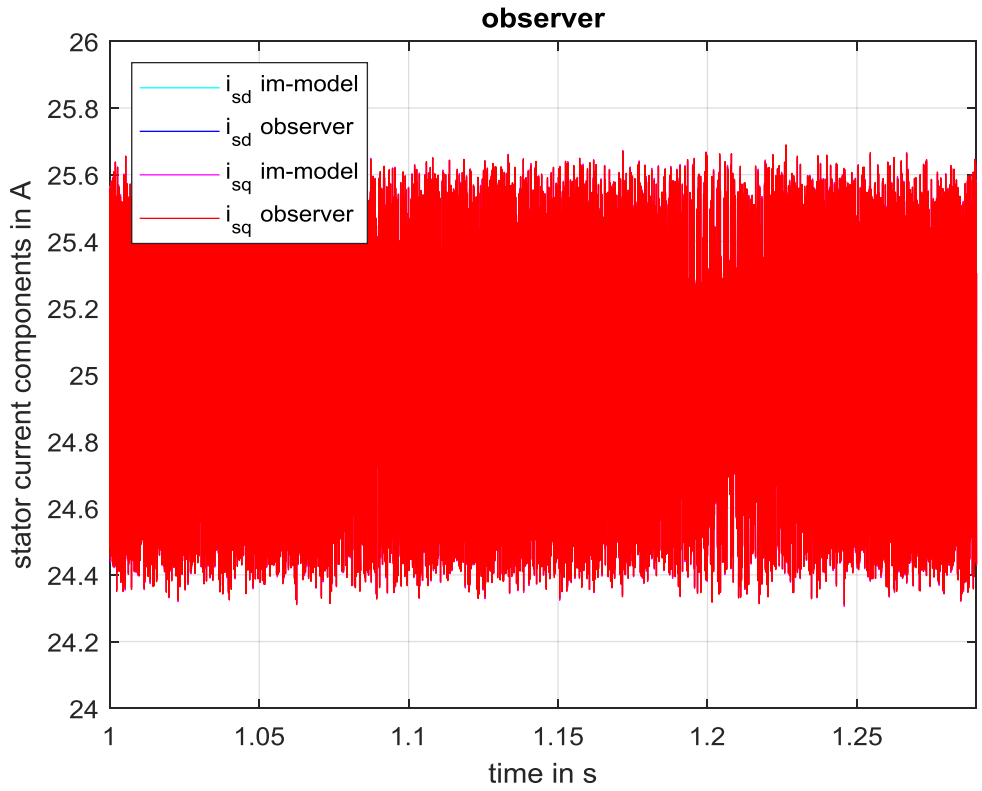

Fig. 14. Stator q-axis ripple current

The electromagnetic torque is given in fig. 15. The torque is controlled by the rotor flux and q-axis current. An increase in the q-axis current results in an increase in the electromagnetic torque. The speed of the rotor is shown in fig. 16. As can be observed, the controllers are able to track the reference signals even at low speeds. The dynamic response of the controller for a step change in the reference signal is shown in fig. 17. It takes $200\mu s$ for the torque to reach its steady state value. This reveals the fast dynamics of the model predictive control scheme. In subsequent sections, the dynamic response of the finite control set model predictive scheme will be compared to other model predictive control schemes.

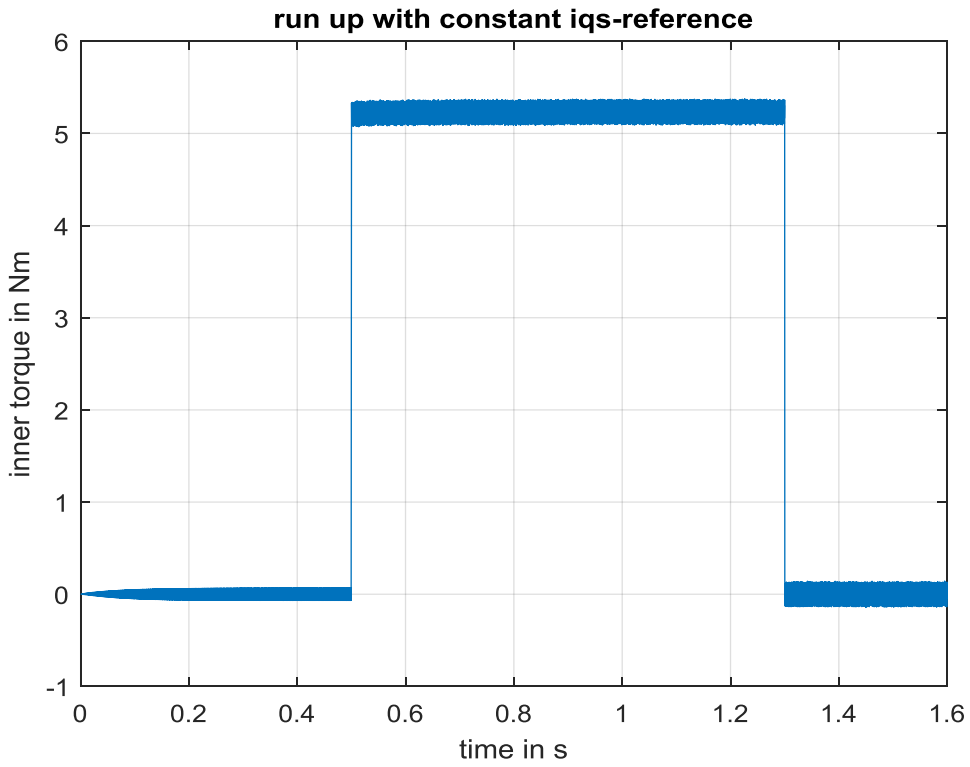

Fig. 15. Response of the electromagnetic torque to a step change in the q axis current

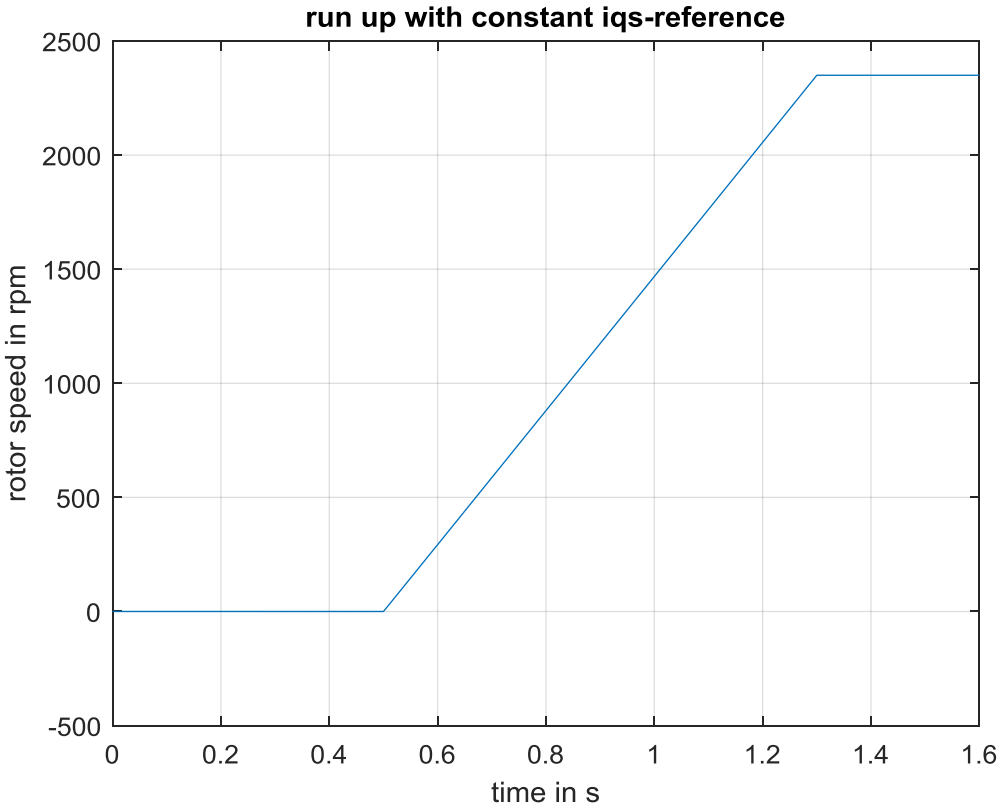

Fig. 16. Speed response of the system during a step change in the q axis current

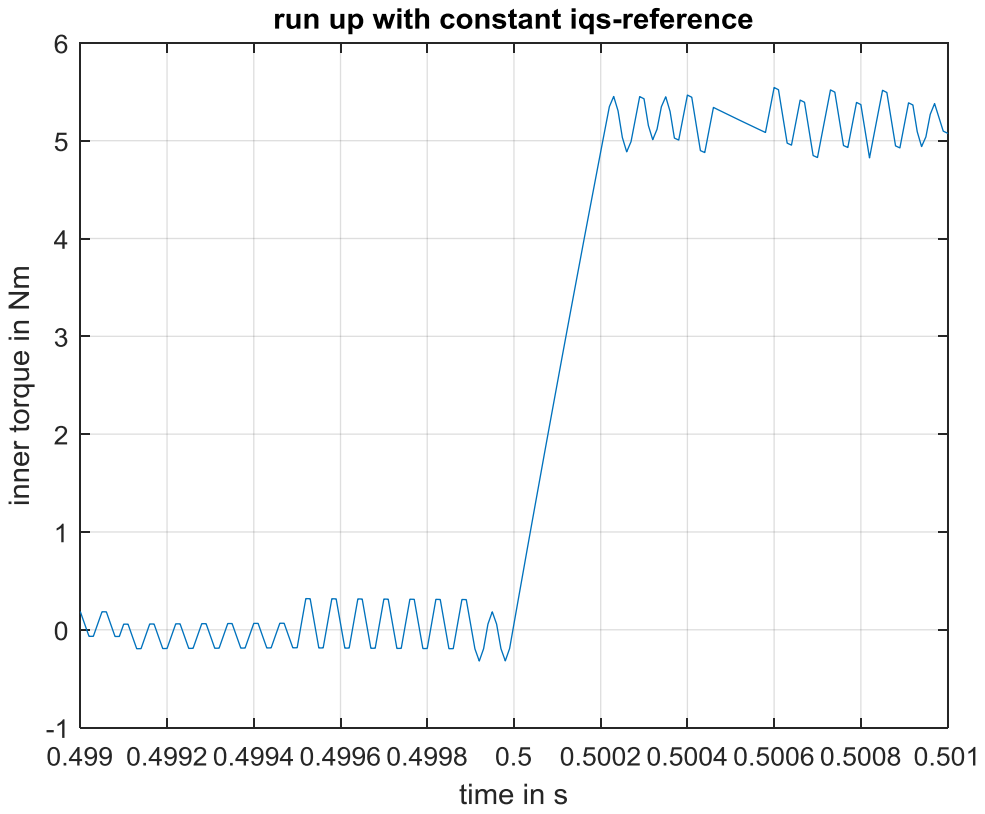

Fig. 17. Electromagnetic torque response of the induction machine under finite control set model predictive control.

The rotor flux estimated by the designed observer is compared to the corresponding flux obtained directly from the machine model as shown in fig. 18. As can be seen there is a close match between the two. The largest error between the estimated rotor flux and the actual flux occurs during the step change in the q-axis stator current. The computed difference between the actual and estimated rotor flux is shown in fig. 19 below.

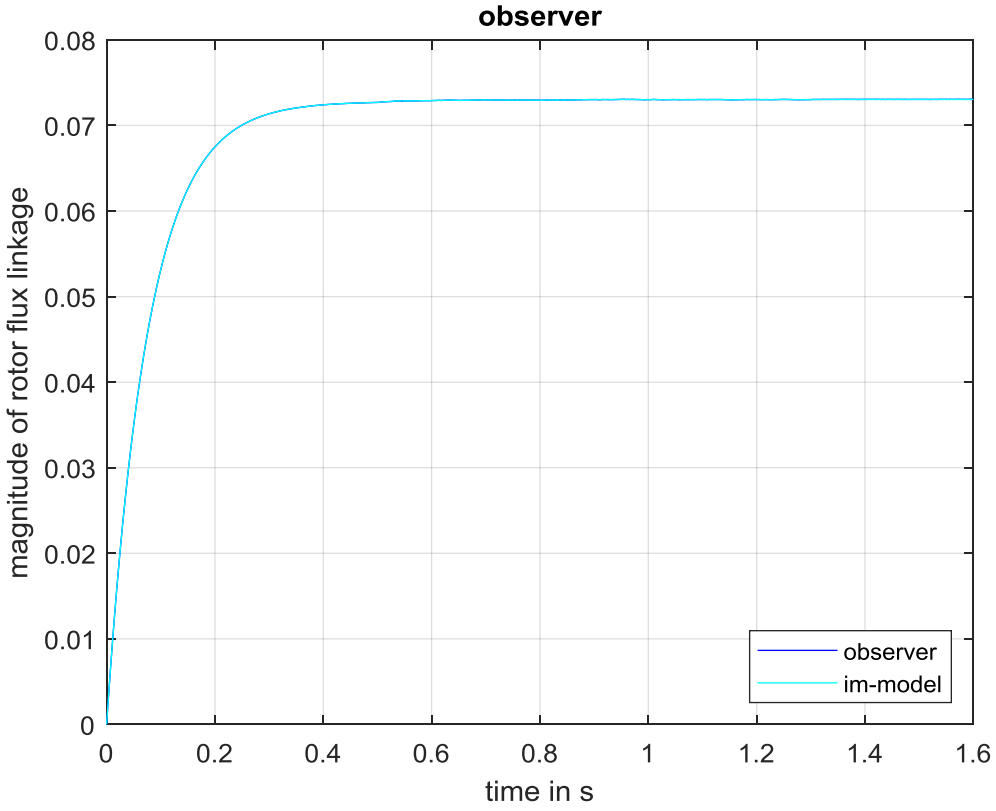

Fig. 18. A comparison between estimated rotor flux from the designed observer and the actual rotor flux.

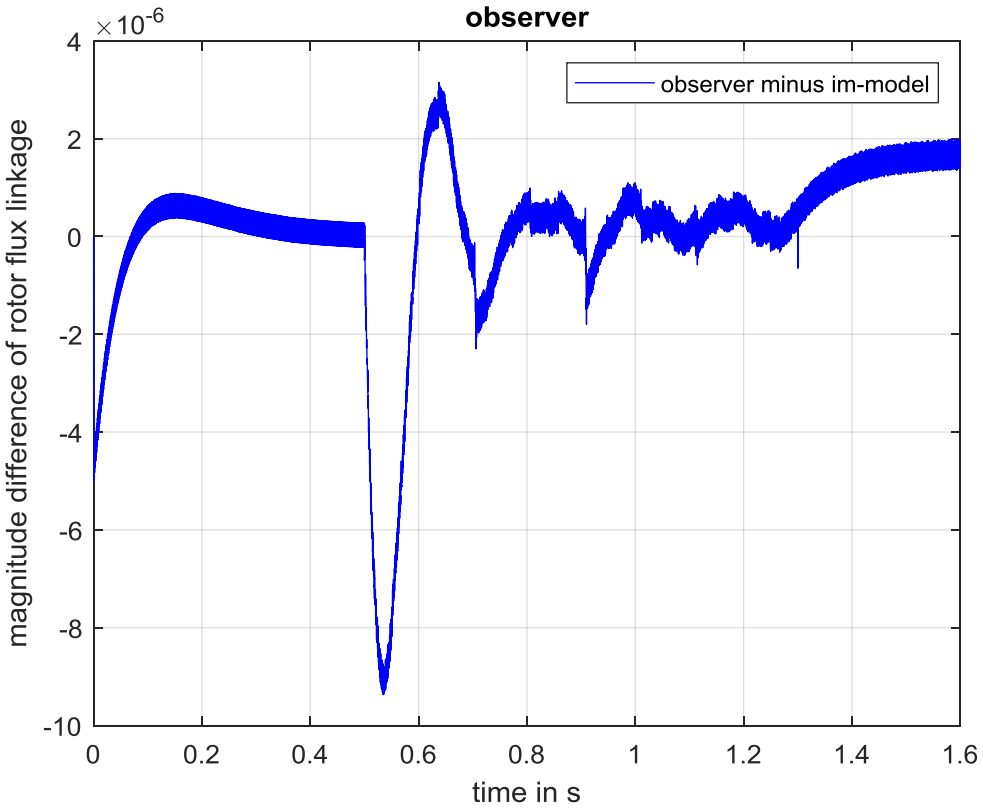

Fig. 19. Computed error in the rotor flux obtained from the designed observer.

The envelope of the stator currents of the machine in the regular abc frame is shown in fig. 20. The magnitude and frequency of the stator current is dependent on the magnitude of the q and d-axis currents and the speed of the induction machine respectively. Fig. 21 shows the stator currents of the machine in a short timescale. As can be seen, the current has switching harmonics superimposed on the fundamental frequency current. One disadvantage of the finite control set model predictive control widely reported in literature is the issue of high ripple torque and currents.

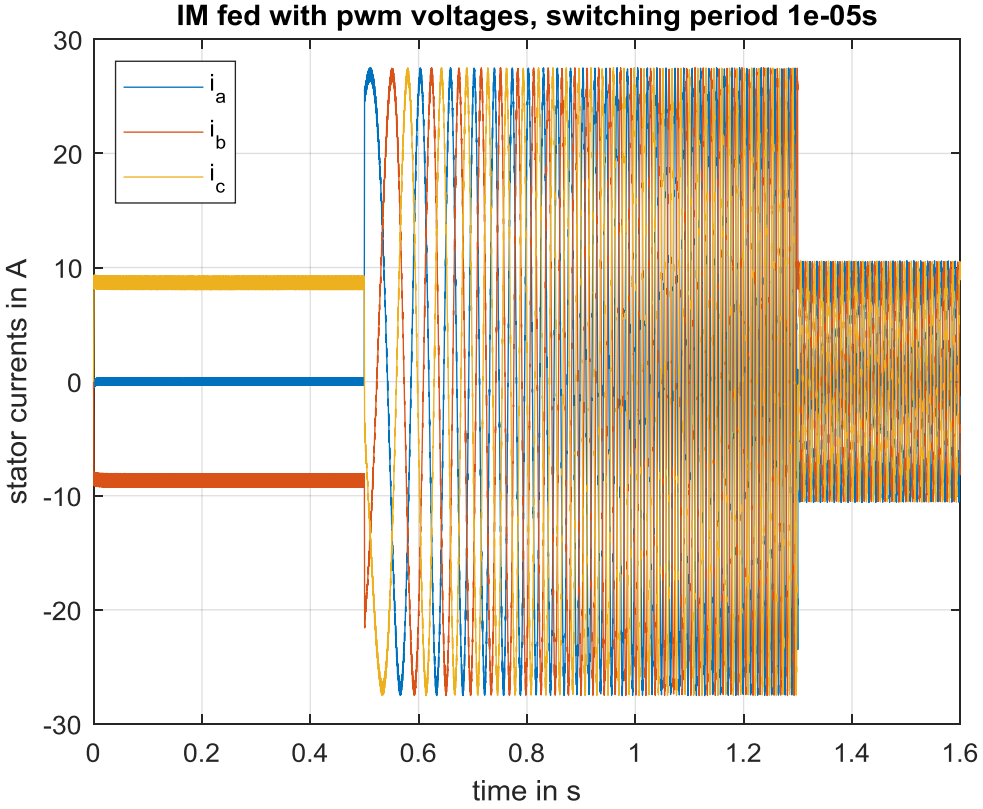

Fig. 20. Induction Machine Currents

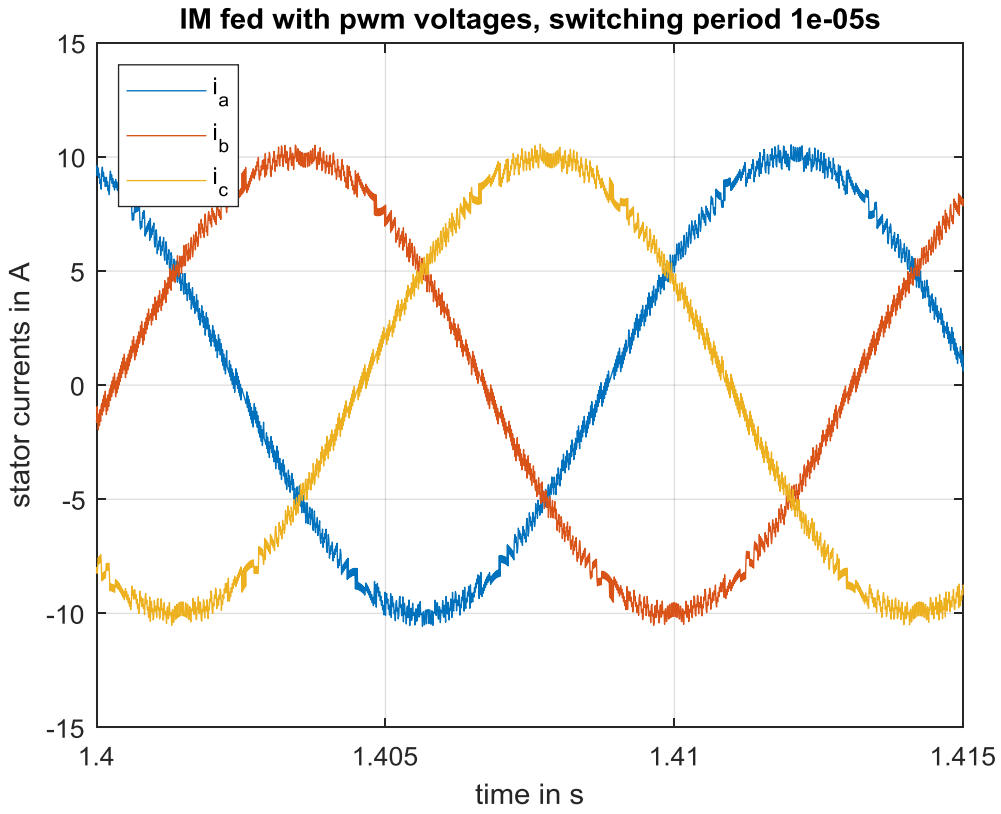

Fig. 21. Induction machine currents showing current ripples for finite control set model predictive control.

In all of the analysis shown above, a sampling time of $10\mu s$ was used. The sampling time was then changed to $100\mu s$ to see the influence of the sampling time on the performance of the controller. As can be observed, the ripple factor for this control scheme depends on the sampling time of the designed control. A decrease in the sampling time leads to an increase in the current ripple of the machine. Therefore to decrease the current and torque ripple of the machine, a high sampling time should be used. However this turns to increase the computational burden of the controller in the final implementation. Therefore a tradeoff between current ripple and computational burden should inform the choice of the sampling time. Fig. 22 shows the current response of the system for step change in the q axis stator current when the sampling time is $100\mu s$. The actual currents and the estimated currents from the designed observer have been provided. Though the controller is able to track the reference current, a very high current ripple is observed. Fig. 23 shows the current ripple for this increase in sampling time. A current ripple of 12A was obtained. This is an order of magnitude higher than that obtained when the sampling time was $10\mu s$. A corresponding increase in the electromagnetic torque ripple is observed as shown in fig. 24.

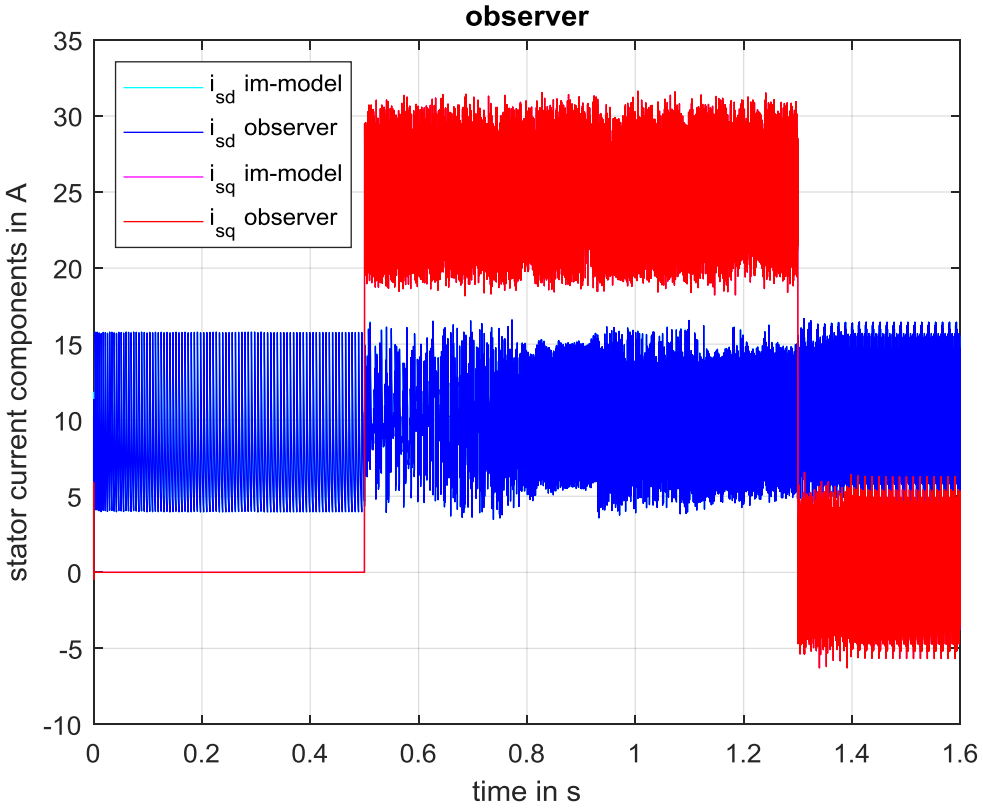

Fig. 22. Simulation results showing the estimated q and d axis currents by the observer and their respective values as obtained from the machine model for a sampling time of $100\mu s$.

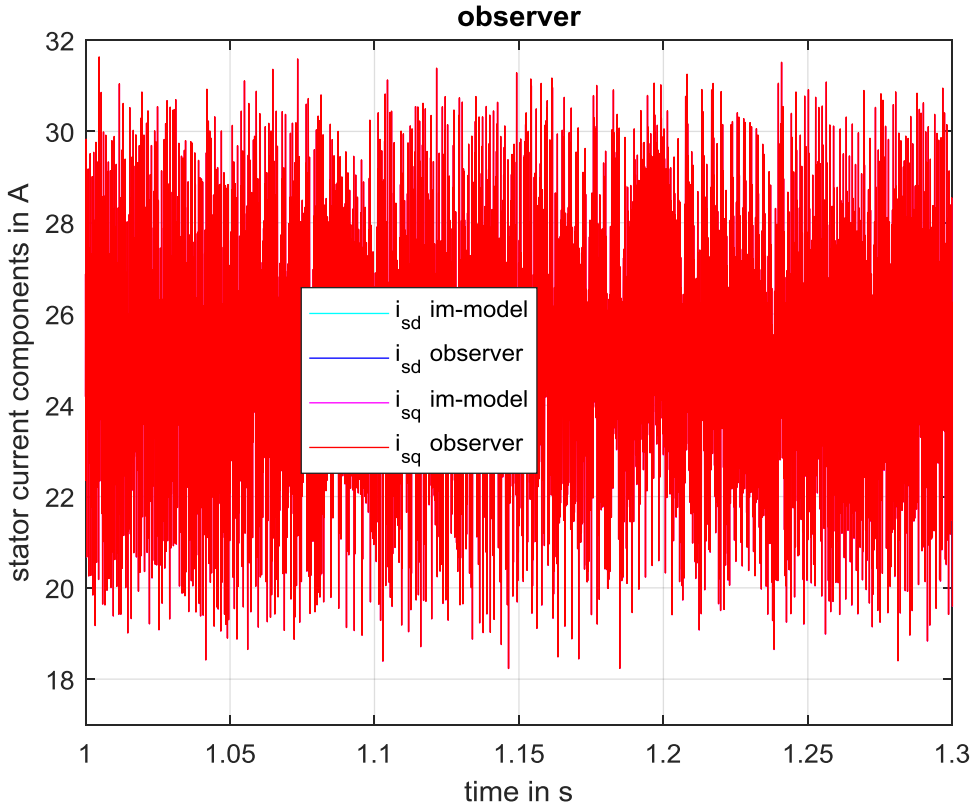

Fig. 23. Q-axis stator current for sampling time of $100\mu s$.

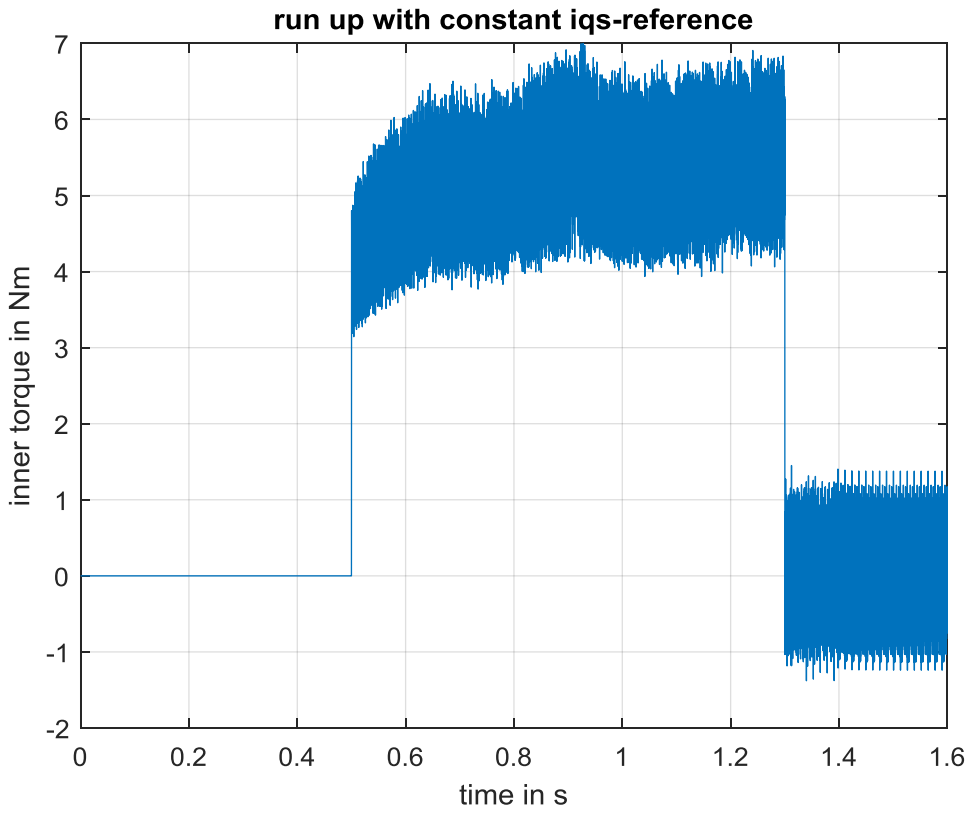

Fig. 24. Electromagnetic torque for sampling time of 100μs showing an increase in ripple.

CHAPTER 4

Continuous Control Set Model Predictive Control

In continuous control set model predictive control scheme, the output of the control is applied to a pulse width modulator. The pulse width modulator generates the switching states which are applied to the inverter. Therefore constant switching frequency is obtained in this regard. Unlike the finite control set case, continuous control obtains the input voltage vectors by solving the optimization function for the optimum solution. The input voltage that gives the optimum solution is obtained and applied to the pulse width modulator.

An objective function is defined to reflect the purpose of the controller design in order to obtain which pair of input signals to use. For the control of the q and d axis currents, the objective function in this work is defined as the squared error between the desired currents and the predicted currents. The objective function is mathematically expressed as:

$$J(k) = \big(e(k+1)\big)^T \big(e(k+1)\big) \tag{46}$$

$$e(k+1) = x^*(k) - x(k+1) \tag{47}$$

From the state space model of the system given as (40):

$$x(k+1) = Ax(k) + Bu(k) + D$$

In order to obtain the optimum solution of the optimization problem explicitly, the optimization function is written in terms of the control input and is given as:

$$J(k) = (x^*(k) - (Ax(k) + Bu(k) + D)^T (x^*(k) - (Ax(k) + Bu(k) + D) \tag{48}$$

The objective function written in the form shown above is to be optimized with respect to the control inputs (voltage vectors). The optimum solution is obtained by taking the derivative of the optimization function with respect to the control input and setting the resulting expression to zero. That is:

$$\frac{dJ(k)}{du(k)} = \frac{d}{du(k)}\Big((x^*(k) - \big(Ax(k) + Bu(k)\big)^T (x^*(k) - \big(Ax(k) + Bu(k)\big)\Big) = 0 \tag{49}$$

The optimum control input is obtained as:

$$U_{opt} = (B^T B)^{-1} B^T (x^*(k) - \big(Ax(k)\big)) \tag{50}$$

In an inverter, the maximum possible output voltage is limited by the dc-link voltage. The relationship between the maximum voltage amplitude and the dc-link voltage is given by:

$$V_{max} = \frac{V_{dc}}{\sqrt{3}} \tag{51}$$

Where V_{dc} is the dc-link voltage. The optimum solution is therefore constrained by V_{max}. If the computed optimum solution violates this constraint, the solution needs to be modified prior to the modulation stage. The optimum solution in this case is modified using the expression:

$$U_{opt}^{a} = \frac{V_{max}}{\|U_{opt}\|} U_{opt} \tag{52}$$

Where U_{opt}^{a} is the modified optimum solution and $\|U_{opt}\|$ is the magnitude of the optimum voltage vector. The voltage is then transformed to a space vector modulator to generate the switching pulses for the inverter.

For the space vector modulator design, first, the optimum voltage vector obtained above is transformed from the synchronous reference frame to the stationary reference frame using the Park to Clarke Transformation given as:

$$\begin{bmatrix} v_\alpha \\ v_\beta \end{bmatrix} = \begin{bmatrix} cos\theta_e & sin\theta_e \\ sin\theta_e & -cos\theta_e \end{bmatrix} \begin{bmatrix} v_q \\ v_d \end{bmatrix} \tag{53}$$

The phase angle between the two vectors is then computed using:

$$tan\delta = \frac{v_\beta}{v_\alpha} \tag{54}$$

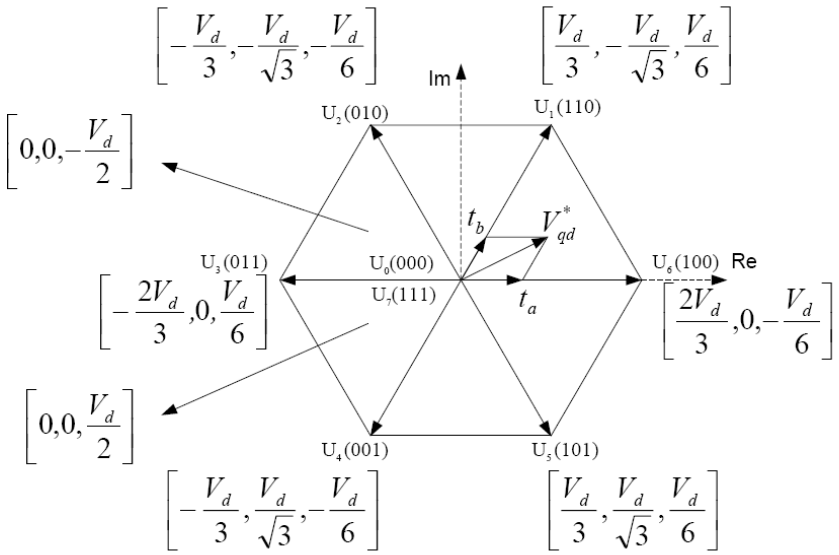

Fig. 25. Schematic of space vector PWM

Based on the value of the angle δ the sector location of the voltage vector can be identified. The switching times for the various switches are then computed based on the sector location.

The duration in which the two active voltage vectors are applied are computed as follows:

For sector one:

$$\frac{t_a}{T_{sc}} = \frac{3v_a - \sqrt{3}v_\beta}{2V_{dc}} \tag{55}$$

$$\frac{t_b}{T_{sc}} = \frac{\sqrt{3}v_\beta}{V_{dc}} \tag{56}$$

For sector two:

$$\frac{t_a}{T_{sc}} = \frac{3v_a + \sqrt{3}v_\beta}{2V_{dc}} \quad (57)$$

$$\frac{t_b}{T_{sc}} = \frac{-3v_a + \sqrt{3}v_\beta}{2V_{dc}} \quad (58)$$

For sector three:

$$\frac{t_a}{T_{sc}} = \frac{\sqrt{3}v_\beta}{V_{dc}} \quad (59)$$

$$\frac{t_b}{T_{sc}} = \frac{-3v_a - \sqrt{3}v_\beta}{2V_{dc}} \quad (60)$$

For sector four:

$$\frac{t_a}{T_{sc}} = \frac{-3v_a + \sqrt{3}v_\beta}{2V_{dc}} \quad (61)$$

$$\frac{t_b}{T_{sc}} = -\frac{\sqrt{3}v_\beta}{V_{dc}} \quad (62)$$

For sector five:

$$\frac{t_a}{T_{sc}} = \frac{-3v_a - \sqrt{3}v_\beta}{2V_{dc}} \quad (63)$$

$$\frac{t_b}{T_{sc}} = \frac{3v_a - \sqrt{3}v_\beta}{2V_{dc}} \quad (64)$$

For sector six:

$$\frac{t_a}{T_{sc}} = -\frac{\sqrt{3}v_\beta}{V_{dc}} \quad (65)$$

$$\frac{t_b}{T_{sc}} = \frac{3v_a + \sqrt{3}v_\beta}{2V_{dc}} \quad (66)$$

T_{sc} is the switching time of the converter.

The time in which the null states are applied is calculated as:

$$t_o = 1 - t_a - t_b \quad (67)$$

Depending on the sector of operation the appropriate switches are then selected.

At every sampling instance, the optimum control is computed. The selection of the controller sampling time is limited by the switching frequency of the converter. In this work, the sampling time of the controller is chosen as half the switching time of the converter. i.e.

$$T_s = 0.5T_{sc} \quad (68)$$

T_s is the sampling time of the controller.

The graphs below show the response of the control system to various reference signals. Fig. 26 shows the response of the current controller to a reference current $I_{ds} = 10$ and a step change in the q-axis current from zero to twenty-five and then from twenty-five to zero at time steps 0.5s and 1.3s respectively. As can be seen, the output current tracks the given reference as desired. The q and d-axis current computed from the observer were compared with those obtained directly from the model to show the effectiveness of the designed observer. At zero torque the observer is able to calculate the actual q and d-axis currents. As can be seen from fig. 26, when I_{qs} is increased from zero to twenty-five (which represents an increase in the electromagnetic torque), the current ripple is observed to increase accordingly. Fig. 27 shows the ripples in the q-axis current at 25A. A ripple of 3A can be observed.

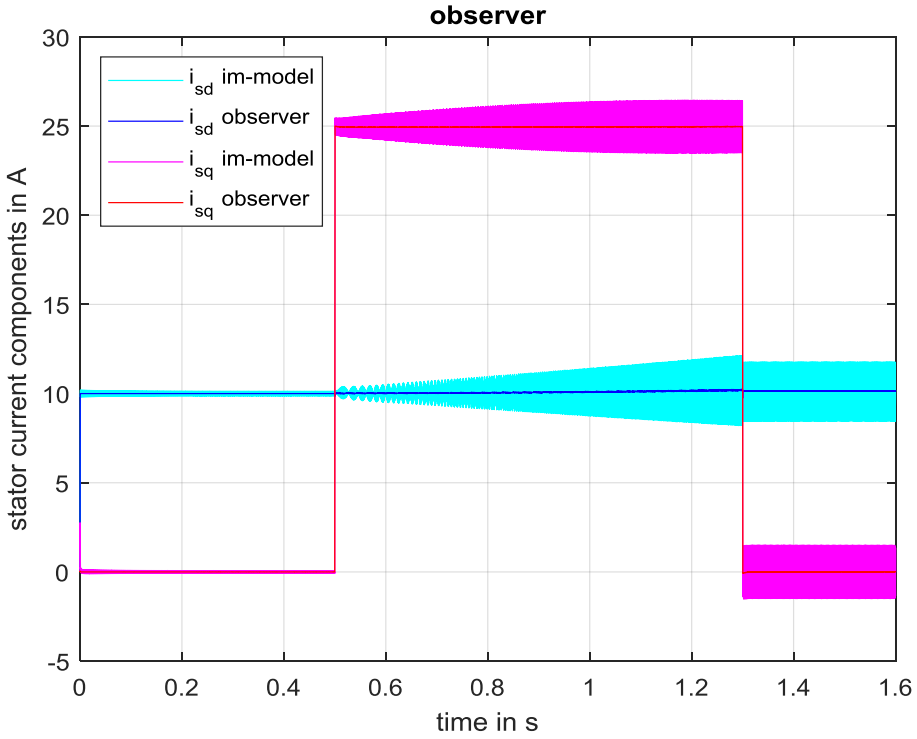

Fig. 26. Simulation results showing the estimated q and d axis currents by the observer and their respective values as obtained from the machine model.

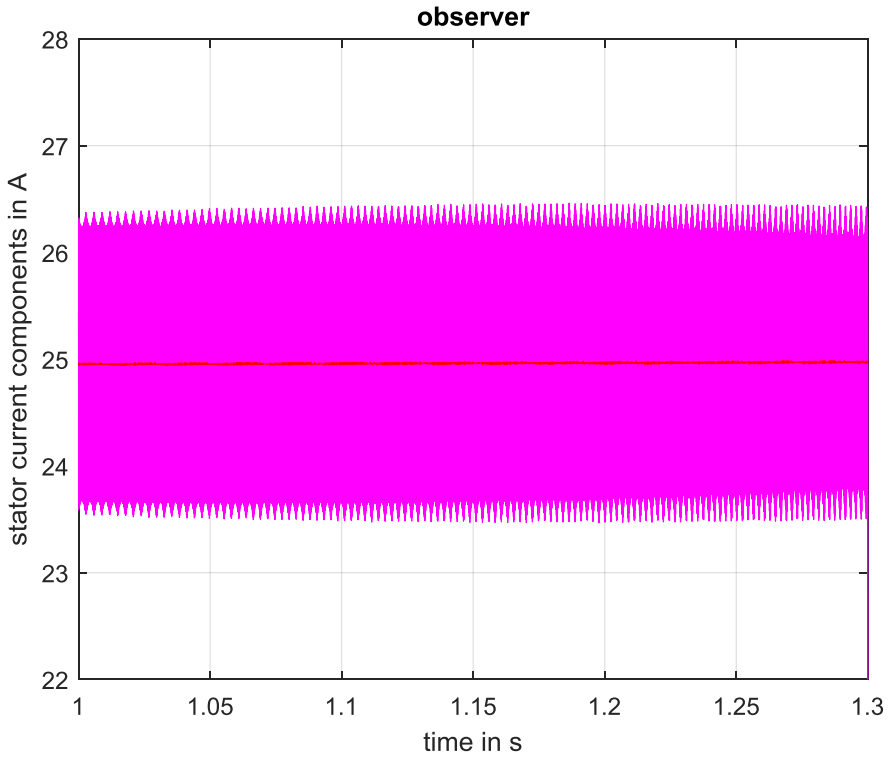

Fig. 27. Q axis stator current

The electromagnetic torque is given in fig. 28. The torque is controlled by the rotor flux and q-axis current. An increase in the q-axis current results in an increase in the electromagnetic torque. The speed of the rotor is shown in fig. 29. As can be observed, the controllers are able to track the reference signals even at low speeds. The dynamic response of the control for a step change in the reference signal is shown in fig. 30. It takes $250\mu s$ for the current to reach its steady state value. This reveals the fast dynamics of the model predictive control scheme. In subsequent sections, the dynamic response of the continuous control set model predictive scheme will be compared to other model predictive control schemes.

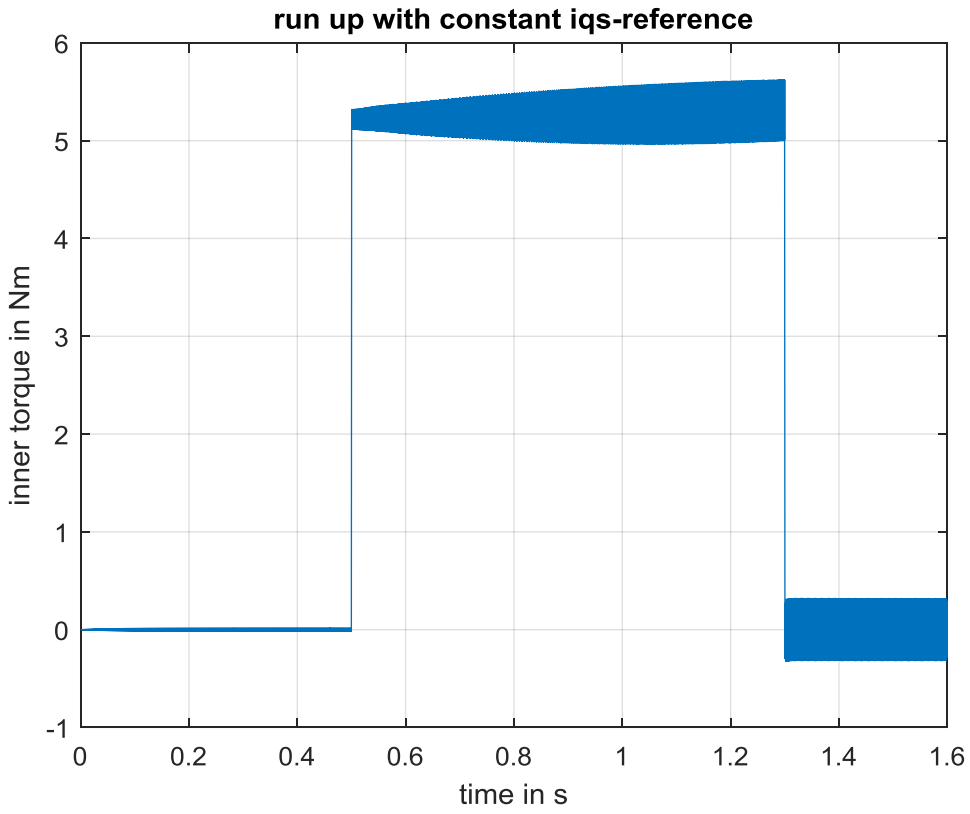

Fig. 28. Response to the electromagnetic torque to a step change in the q axis current

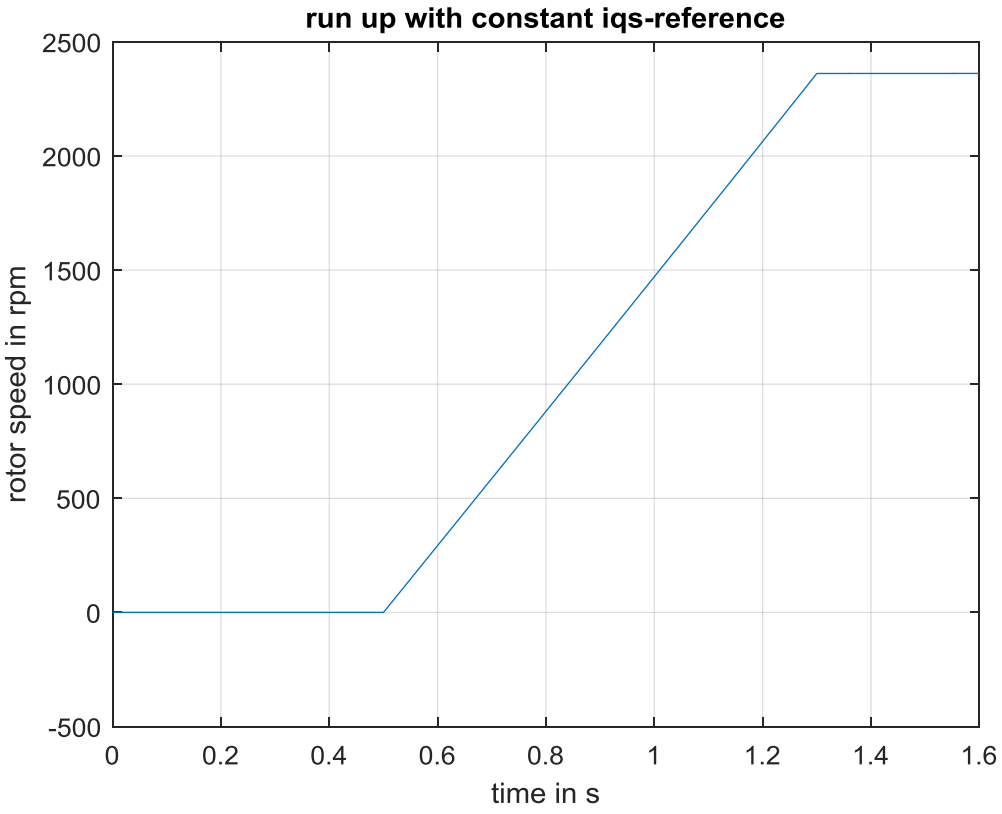

Fig. 29. Speed response for the induction machine for a step change in q axis current under continuous control set model predictive control.

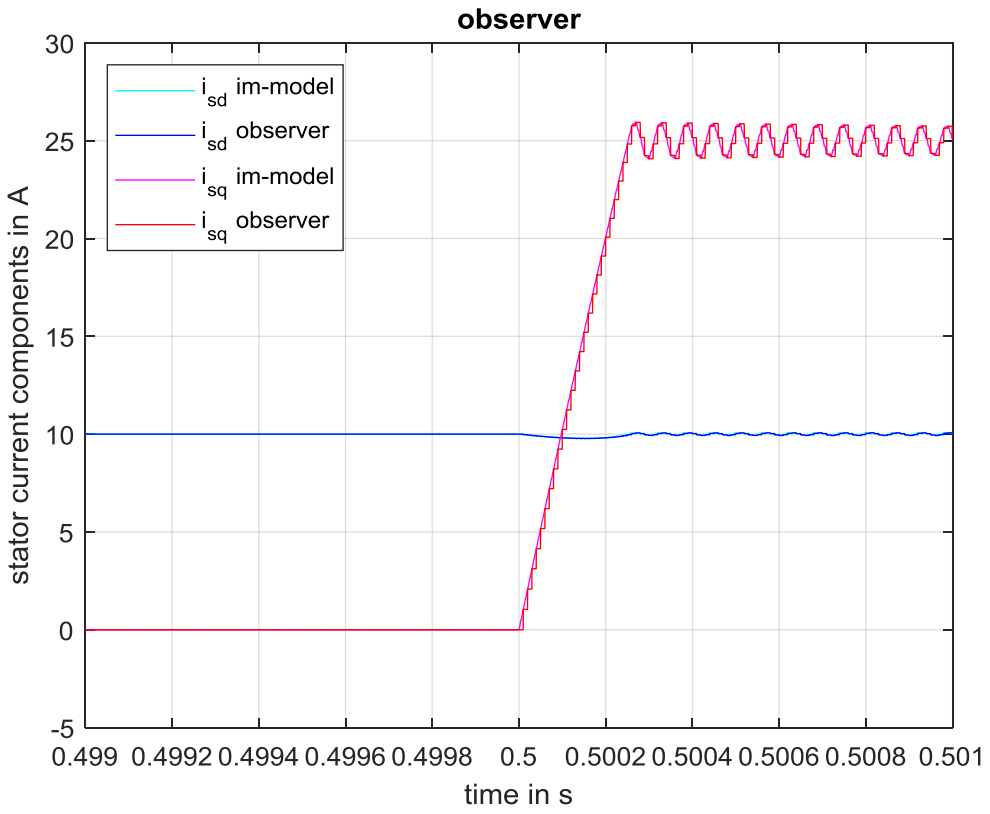

Fig. 30. Current response of the induction machine under continuous control set model predictive control.

The rotor flux computed by the observer is compared to that obtained directly from the machine model in fig. 31. As can be seen there is a close match between the two. However, at high speed and zero torque, the estimated flux deviates from the expected value. This phenomenon is shown in fig. 32. where the error between the estimated flux and actual flux is presented.

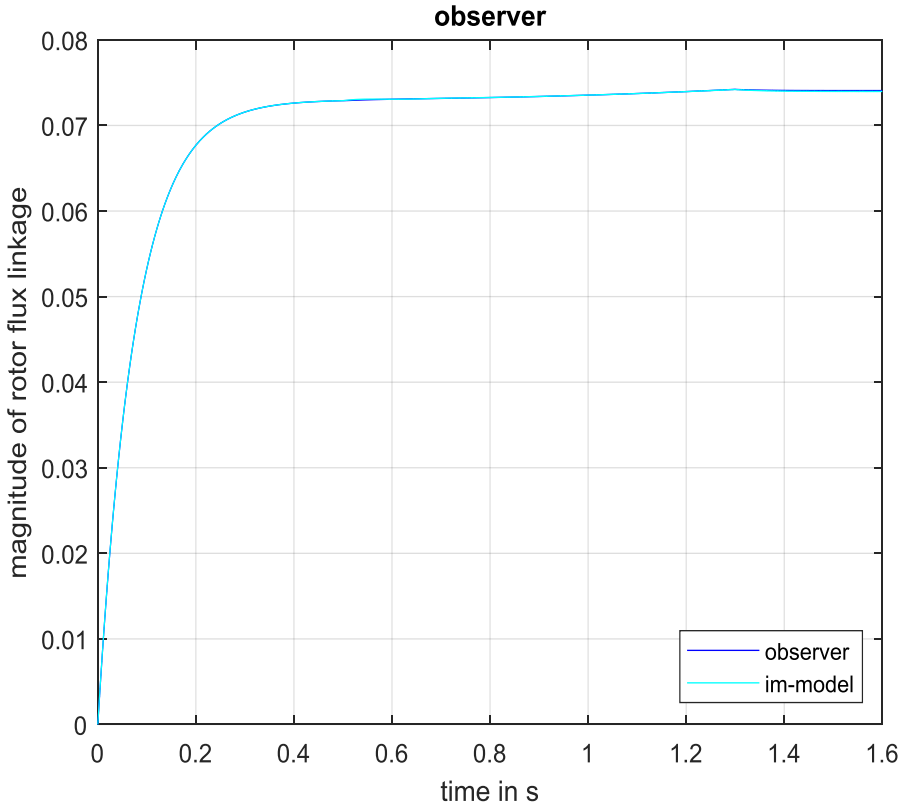

Fig. 31. A comparison between estimated rotor flux from the designed observer and the actual rotor flux.

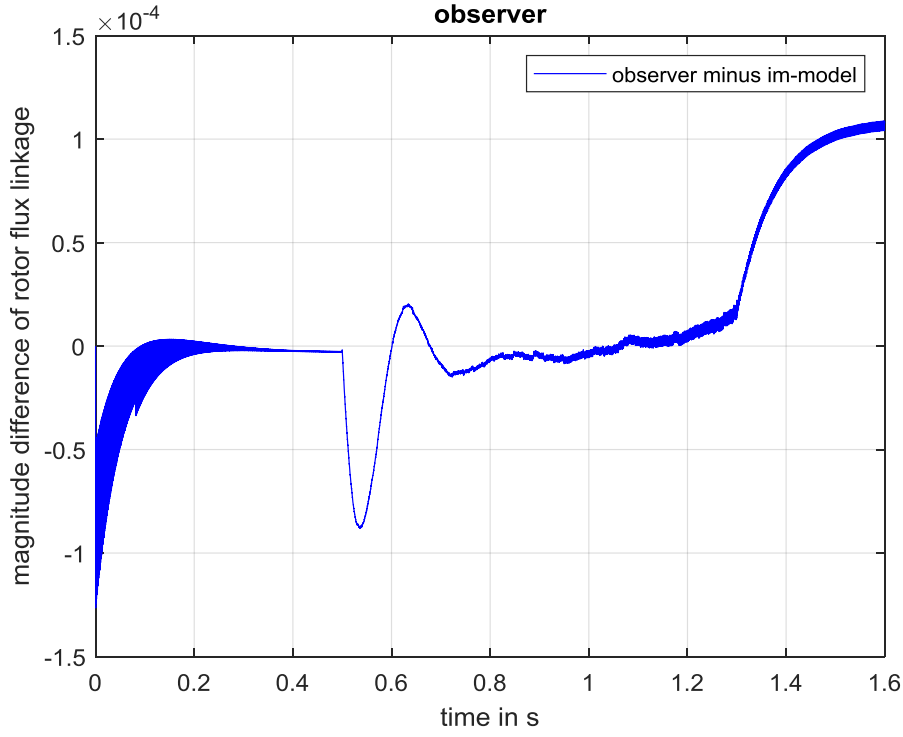

Fig. 32. Computed error in the rotor flux obtained from the designed observer.

The stator current of the machine in the regular abc frame is shown in fig. 33. The magnitude and frequency of the stator current is dependent on the magnitude of the q and d-axis currents and the speed of the induction machine respectively. Fig. 34 shows the stator currents of the machine in a short timescale. The current has switching harmonics superimposed on the fundamental frequency current. One disadvantage of the continuous control set model predictive control widely reported in literature is the issue of ripple currents.

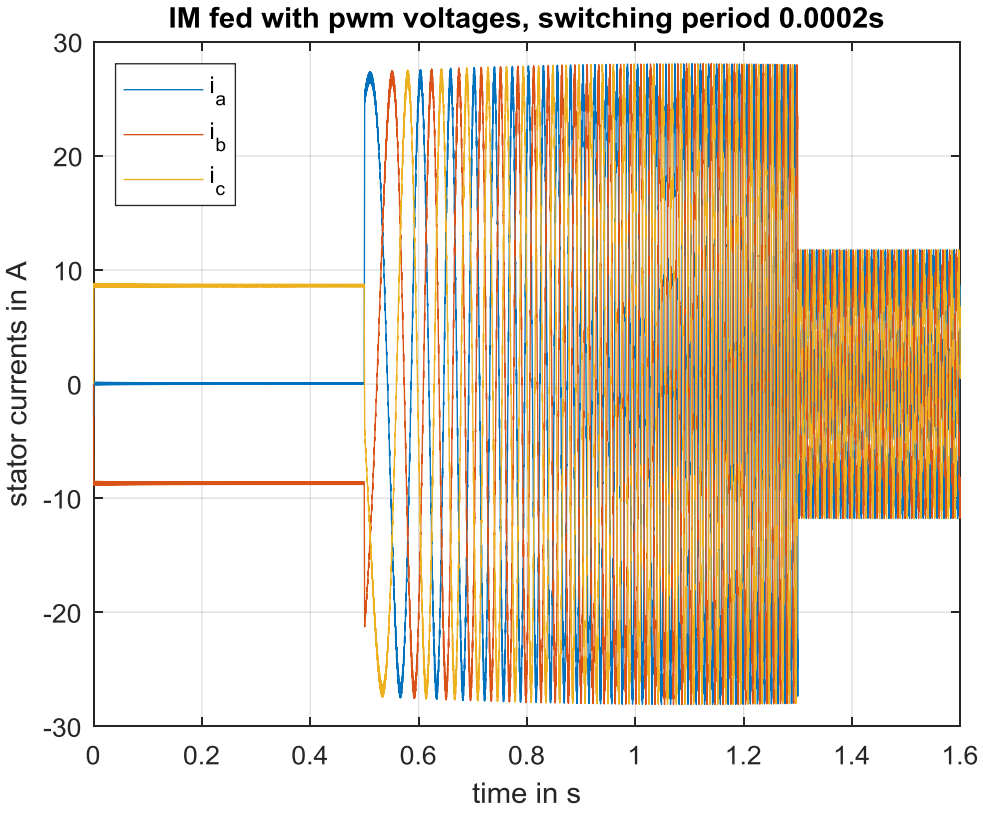

Fig. 33. Induction machine current envelope under continuous control set model predictive control.

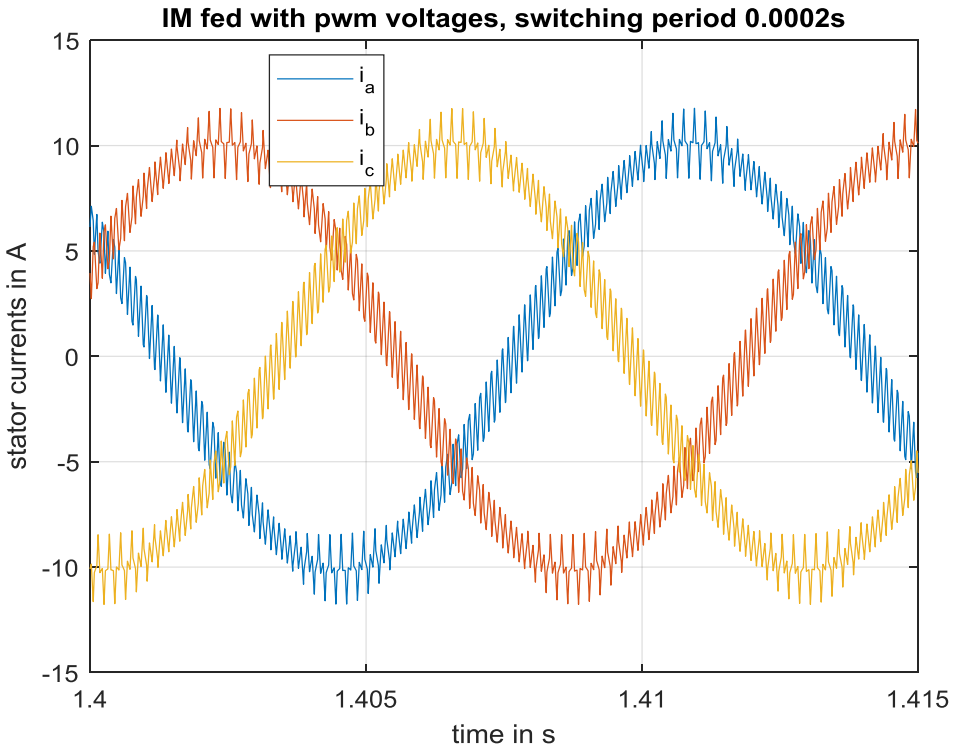

Fig. 34. Induction machine currents shown current ripples for continuous control set model predictive control.

Chapter 5

Continuous Control Set Model Predictive Control with Long Prediction and Control Horizon (CCSLP-MPC)

In the work done so far, the computation of the control input and/or switching states was done by making a one step ahead prediction of the states based on the present outputs. In general, instead of making a step ahead prediction of the future evolution of the system, the trajectory of the system can be calculated in a number of time steps into the future. By computing the evolution of the system in a number of steps into the future, planning of the future control action could be incorporated into the calculating the present control input. The time steps (the number of samples) used to capture the future states of the system is known as the prediction horizon. The number of control actions needed to drive the system to the predicted future can also be decided. If a few number of samples are used to capture the input action this could lead to an aggravated control action and drive the controller into saturation. The number of samples used to capture the control action is known as the control horizon.

Instead of using the actual machine states in the controller implementation, the incremental dynamics of the system states are used. By using the incremental dynamics, the constant term, which represents the disturbance input to the system, is eliminated. An augmented state space model is obtained by augmenting the output incremental dynamics with that of the state space incremental dynamics. Therefore, a new state vector is chosen as $[\Delta x(k), y(k)]$. The future control trajectory is denoted by the vector $[\Delta u(k), \Delta u(k+1) \dots \Delta u(k+N_c-1)]$ where N_c is the control horizon, indicating the number of samples used to capture the future control trajectory. With this information, the future state vectors are predicted by N_p samples, where N_p is the prediction horizon. Even though N_c samples are used to capture the future control action, only the first component of the samples is used. This in model predictive control is called receding horizon control. At every time step, a prediction is made into the future but only the first sample of the control input is used.

Using the augmented model, the future trajectory is calculated sequentially leading to a set of equations which can be written in compact form as:

$$x(k+1) = Fx(k) + \phi\Delta u \tag{69}$$

Where $F = \begin{bmatrix} A \\ A^2 \\ \vdots \\ A^{N_p} \end{bmatrix}$, $\phi = \begin{bmatrix} B & 0 & \cdots & 0 \\ AB & B & \cdots & 0 \\ A^2B & AB & \cdots & 0 \\ \vdots & \vdots & \cdots & \vdots \\ A^{N_p-1}B & A^{N_p-2}B & \cdots & A^{N_p-N_c}B \end{bmatrix}$

The cost function is given by the sum of the squared error between the reference state values and the measured states and the squared error between the desired control input and the actual control input. The cost function is mathematically expressed as:

$$J = x^T Q x + \Delta u^T R \Delta u \tag{70}$$

Where Q and R are block diagonal matrices.

Following a similar approach as presented in the case for CCS MPC, the optimum control input can be obtained. The optimum control input is given as:

$$\Delta \mathrm{u}_{\mathrm{opt}} = -(\phi^T Q \phi + R)^{-1}(\phi^T Q F x) \tag{71}$$

Only the first component of the optimum input is used in the actual control implementation under receding horizon control. The optimum input computed is the incremental control input. The actual input to the plant is calculated as the sum of the computed optimum input and the past input to the plant. This is given by the expression:

$$u(k) = u(k-1) + \Delta u_{opt} \tag{72}$$

For this purpose, the past plant input are stored and used in the computation of the current control input. Alternatively, the measured voltage at the inverter output is fed to the controller. This is seldom done in practice since it will lead to additional cost in measuring the output voltages with its attendant measurement errors. In the determination of the prediction and control horizons, one should be mindful of the extra computational burden imposed on the controller by the additional data and computations. This is often a limiting factor in determining the prediction and control horizons.

To examine the performance of the designed controller, a dynamic simulation of the system was performed in Matlab/Simulink. The graphs below show the response of the control system to various reference signals for a prediction horizon of five and a control horizon of 2. Fig. 35 shows the response of the current controller to a reference current $I_{ds} = 10$ and a step change in the q-axis current from zero to twenty-five and then from twenty-five to zero at time steps 0.5s and 1.3s respectively. As can be seen, the output current tracks the given reference as desired. The q and d-axis current computed from the observer were compared with those obtained directly from the model to show the effectiveness of the designed observer. At zero torque the observer is able to estimate the actual q and d-axis currents. As can be seen from fig. 35, when I_{qs} is increased from zero to twenty-five (which represents an increase in the electromagnetic torque), the current ripple is observed to increase accordingly. Compared to the two CCS-MPC and FCS-MPC, CCSLP-MPC has an oscillatory response with a high peak overshoot. Fig. 36 shows the ripples in the q-axis current at 25A. A ripple of 1.1A can be observed. The magnitude of the ripple for the various model predictive control schemes will be compared in subsequent sections.

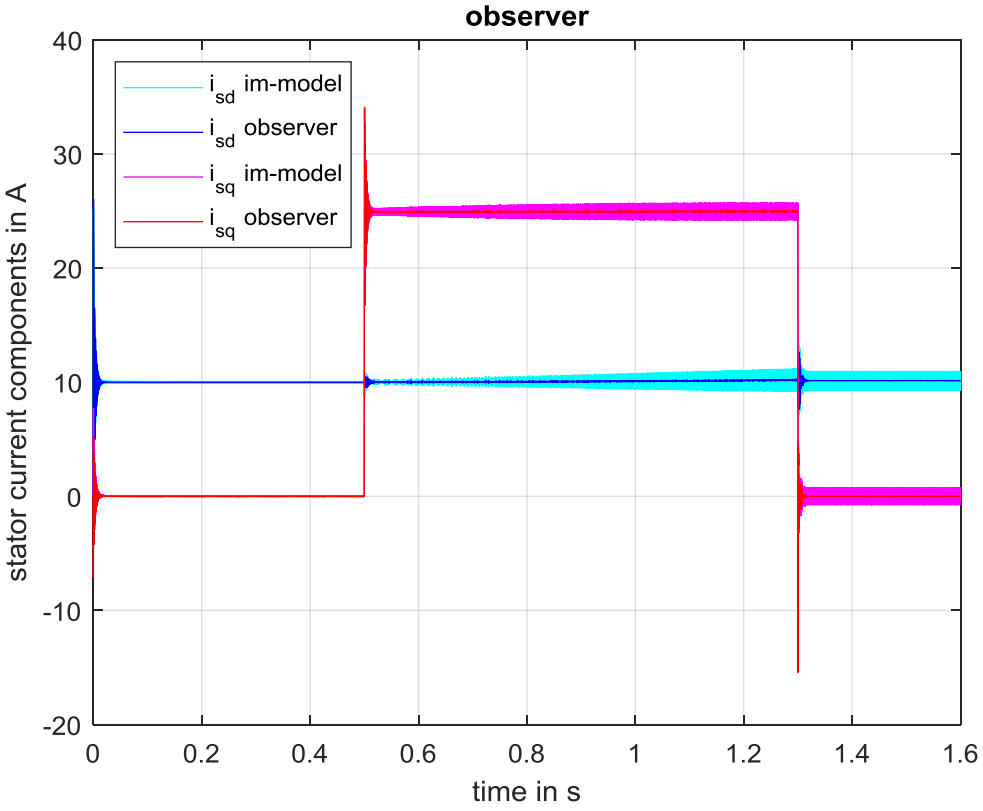

Fig. 35. Simulation results showing the estimated q and d axis currents by the observer and their respective values as obtained from the machine model.

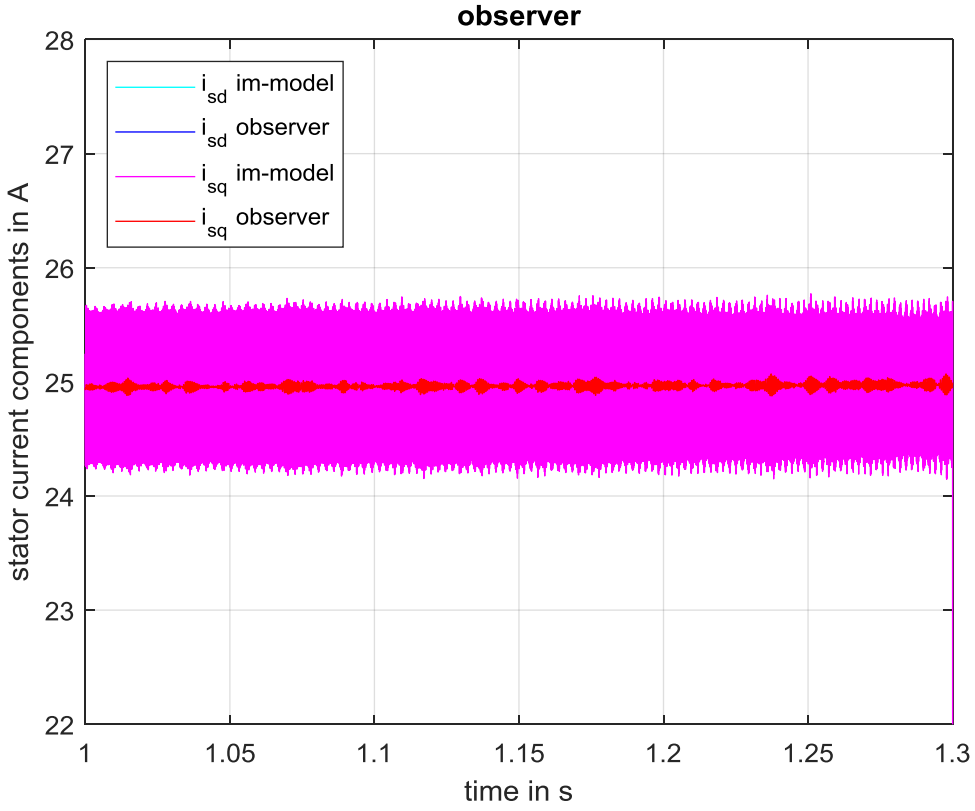

Fig. 36. Q axis stator current.

The electromagnetic torque is given in fig. 37. The torque is controlled by the rotor flux and q-axis current. An increase in the q-axis current results in an increase in the electromagnetic torque. The speed of the rotor is shown in fig. 38. As can be observed, the controllers are able to track the reference signals even at low speeds. The dynamic response of the control for a step change in the reference signal is shown in fig. 39. It takes $5ms$ for the current to reach its steady state value. This reveals the fast dynamics of the model predictive control scheme. In subsequent sections, the dynamic response of the CCSLP-MPC will be compared to other model predictive control schemes.

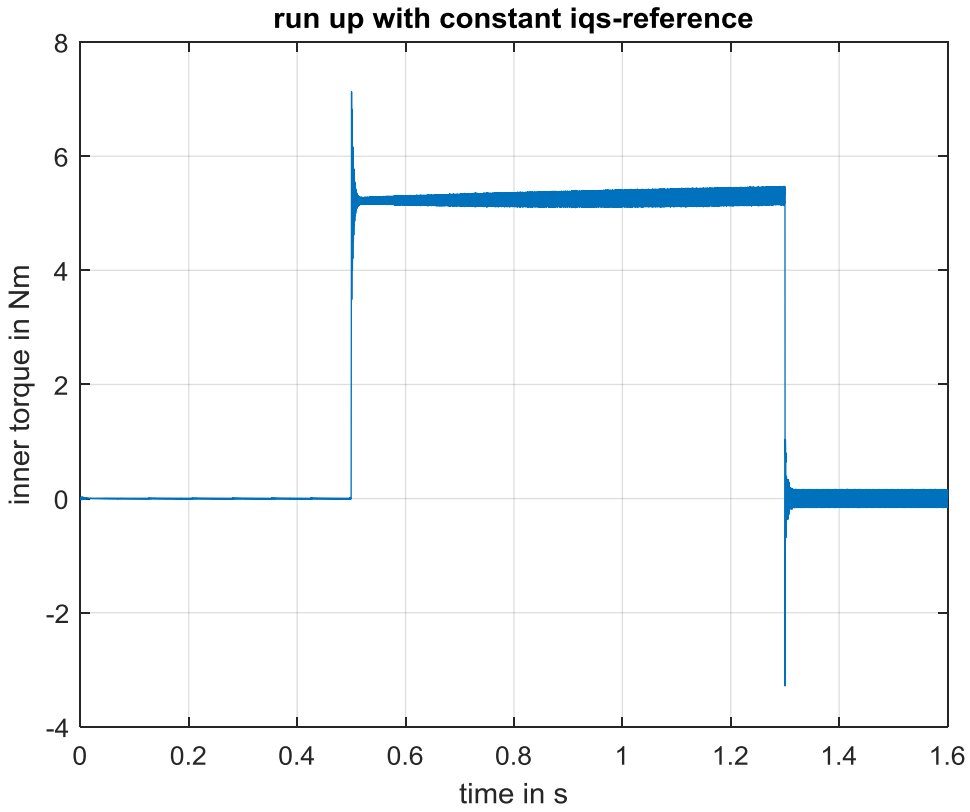

Fig. 37. Response to the electromagnetic torque to a step change in the q axis current

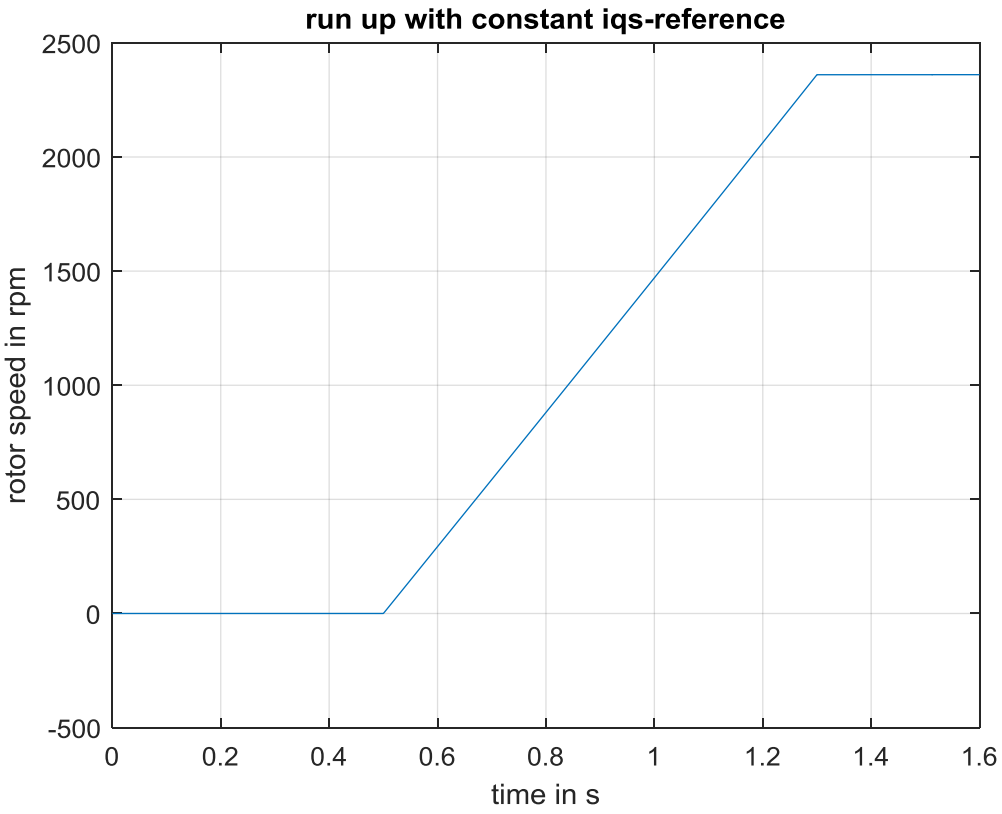

Fig. 38. Speed response of the induction machine for a step change in q axis current under CCSLP-MPC.

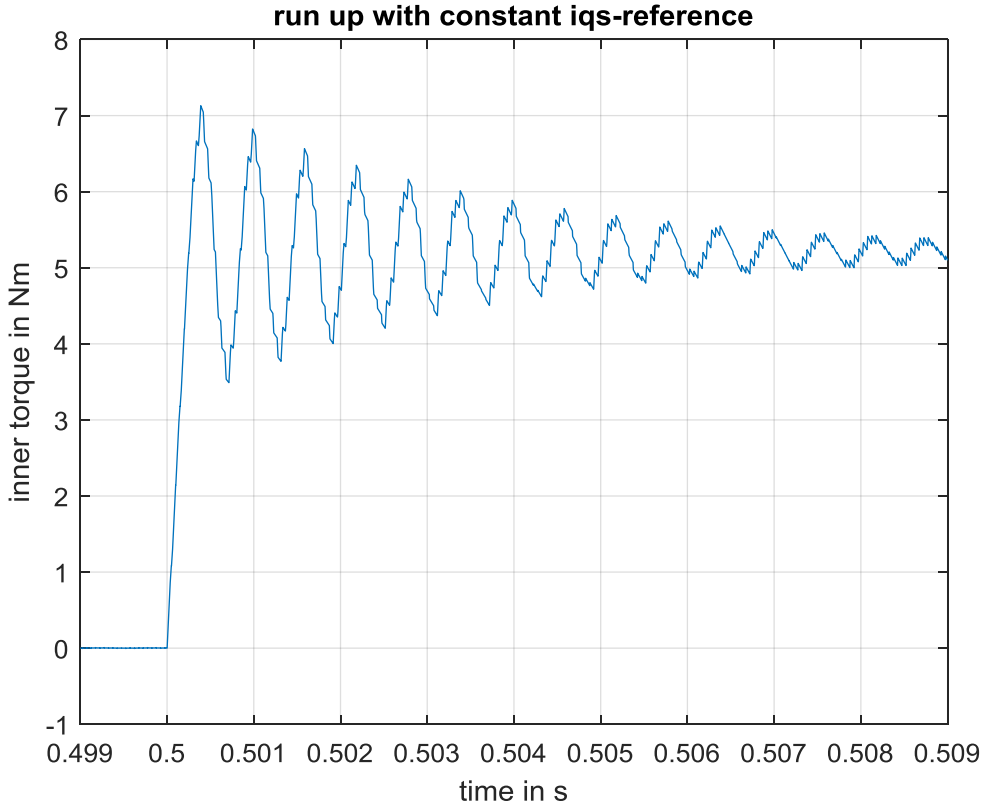

Fig. 39. Electromagnetic torque response of the induction machine under CCSLP-MPC.

The stator current of the machine in the regular abc frame is shown in fig. 40. The magnitude and frequency of the stator current is dependent on the magnitude of the q and d-axis currents and the speed of the induction machine respectively. Fig. 41 shows the stator currents of the machine in a short timescale. As can be seen, the current has switching harmonics superimposed on the fundamental frequency current.

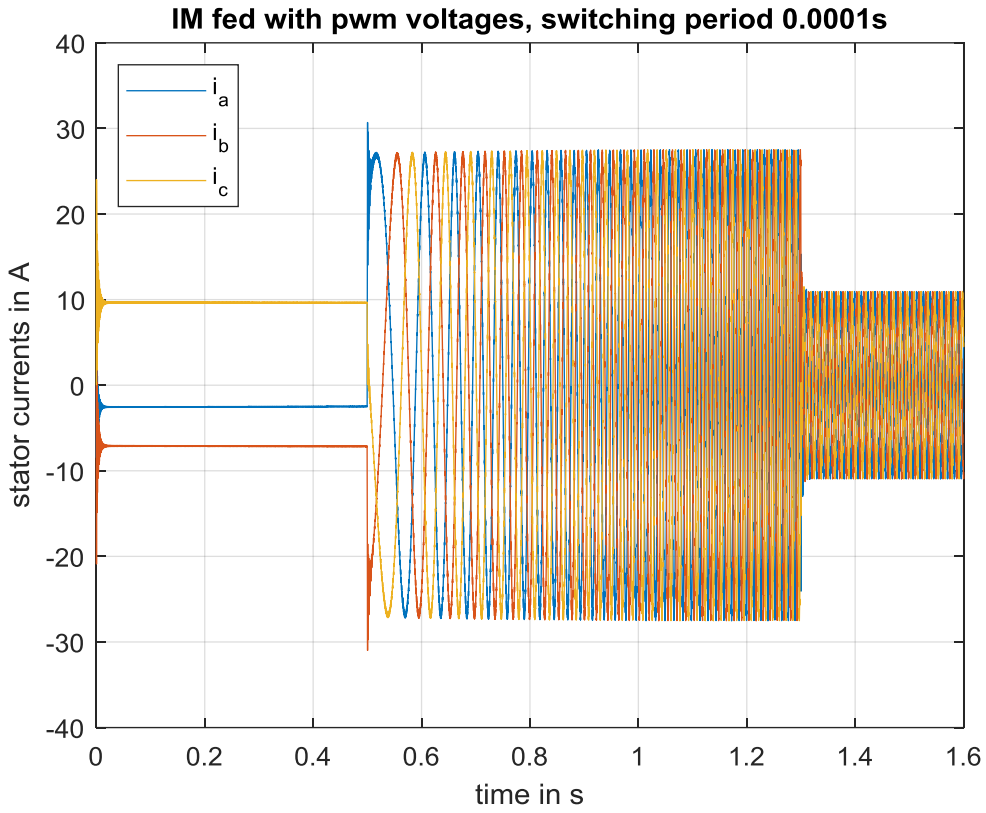

Fig. 40. Induction machine current envelope.

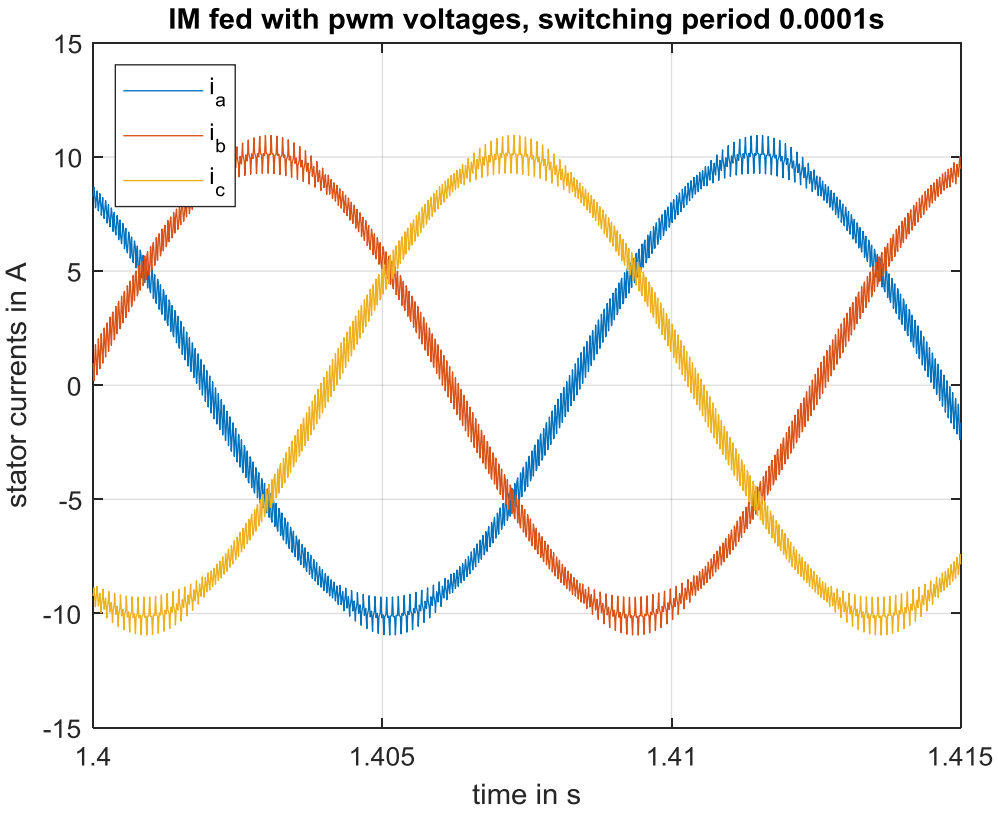

Fig. 41. Induction machine currents shown current ripples

CHAPTER 6

Finite Control Set Model Predictive Control with Long Prediction and Control Horizon (FCSLP-MPC)

Similar to the continuous control step set with long prediction and control horizons, a finite control set with long prediction and control horizon is presented in this section. An augmented model is created by augmenting the output incremental dynamics to that of the state incremental dynamics. The rest of the formulation is similar to the steps laid out in the continuous control set with long prediction and control horizons. In this section, only the differences in the two methods will be presented.

In this method, instead of applying the computed control inputs to the inputs of a pulse width modulator, the switching functions are directly synthesized in the controller. This eliminates the need for a pulse width modulation scheme. First, the eight possible voltage vectors of the two level inverter are computed at a given sampling time. The difference between the calculated optimum input voltage and each of the eight voltage vectors is obtained. The squared error is then computed. The voltage vector that corresponds to the minimum squared error is selected. The switching function corresponding to that voltage vector is applied to the inverter.

Just like the finite control set model predictive control scheme, the switching frequency for this control scheme is variable. The stability of the system is dependent on the sampling time selected. A low sampling time leads to a controller with high feedback gain. This can reduce the settling time of the system response but could result in a possible control deviation. The incremental model introduces some integral action into the system and therefore reduces the tendency to end up with a control deviation.

To reduce the computational burden, parameters of the control which are not dependent on the operating conditions of the machine are computed offline.

The graphs below show the response of the control system to various reference signals for a prediction horizon of five and a control horizon of two. Fig. 42 shows the response of the current controller to a reference current $I_{ds} = 10$ and a step change in the q-axis current from zero to twenty-five and then from twenty-five to zero at time steps 0.5s and 1.3s respectively. As can be seen, the output current tracks the given reference as desired. The q and d-axis current computed from the observer were compared with those obtained directly from the model to show the effectiveness of the designed observer. At zero torque the observer is able to estimate the actual q and d-axis currents. As can be seen from fig.30, when I_{qs} is increased from zero to twenty-five (which represents an increase in the electromagnetic torque), the current ripple is observed to increase accordingly. Fig. 43 shows the ripples in the q-axis current at 25A. A ripple of 3.2A can be observed. The magnitude of the ripple for the various model predictive control schemes will be compared in subsequent sections.

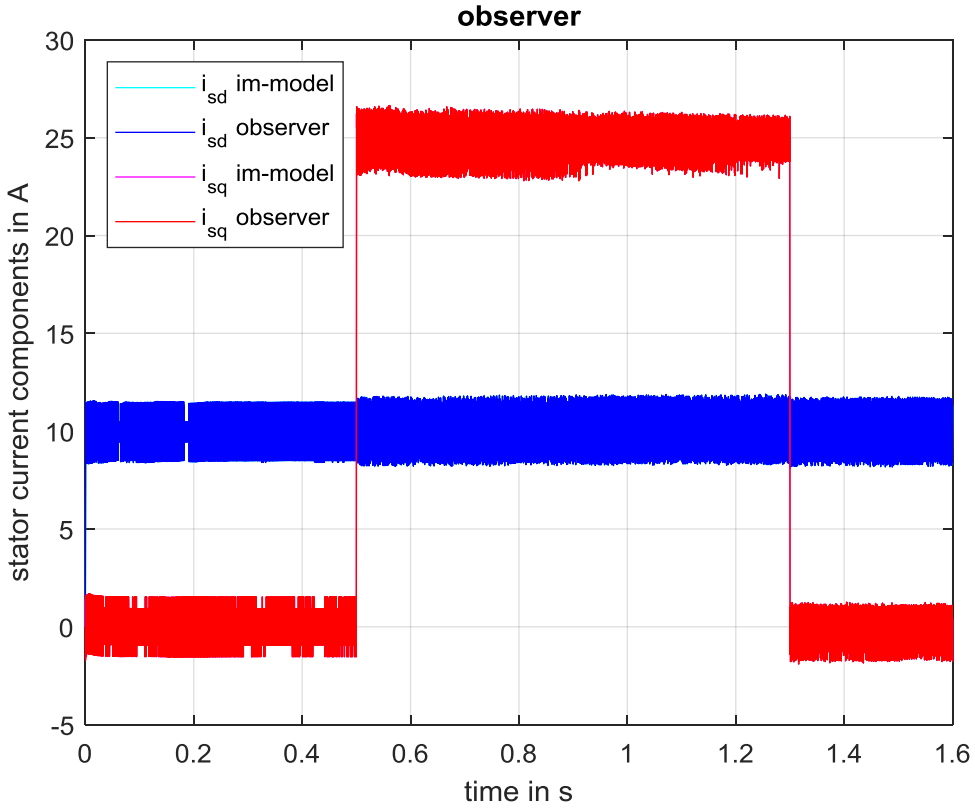

Fig. 42. Simulation results showing the estimated q and d axis currents by the observer and their respective values as obtained from the machine model.

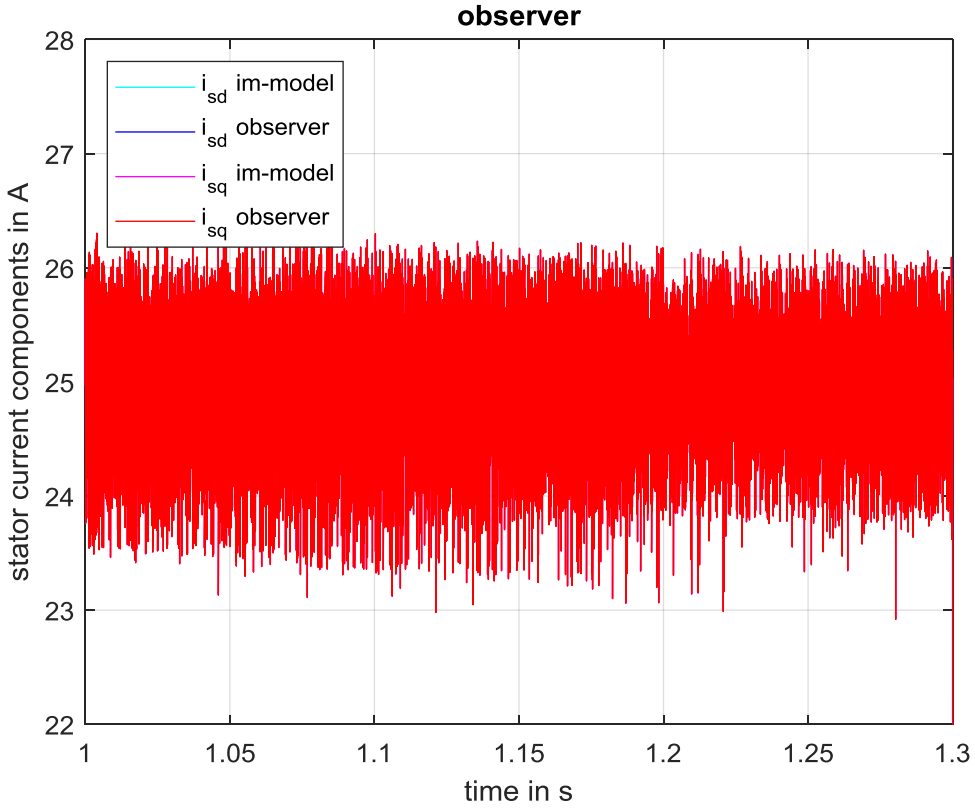

Fig. 43. Q axis stator current.

The electromagnetic torque is given in fig. 44. The torque is controlled by the rotor flux and q-axis current. An increase in the q-axis current results in an increase in the electromagnetic torque. The speed of the rotor is shown in fig. 45. As can be observed, the controllers are able to track the reference signals even at low speeds. The dynamic response of the control for a step change in the reference signal is shown in fig. 46. It takes $200\mu s$ for the current to reach its steady state value. This reveals the fast dynamics of the model predictive control scheme. In subsequent sections, the dynamic response of the FCSLP-MPC will be compared to other model predictive control schemes.

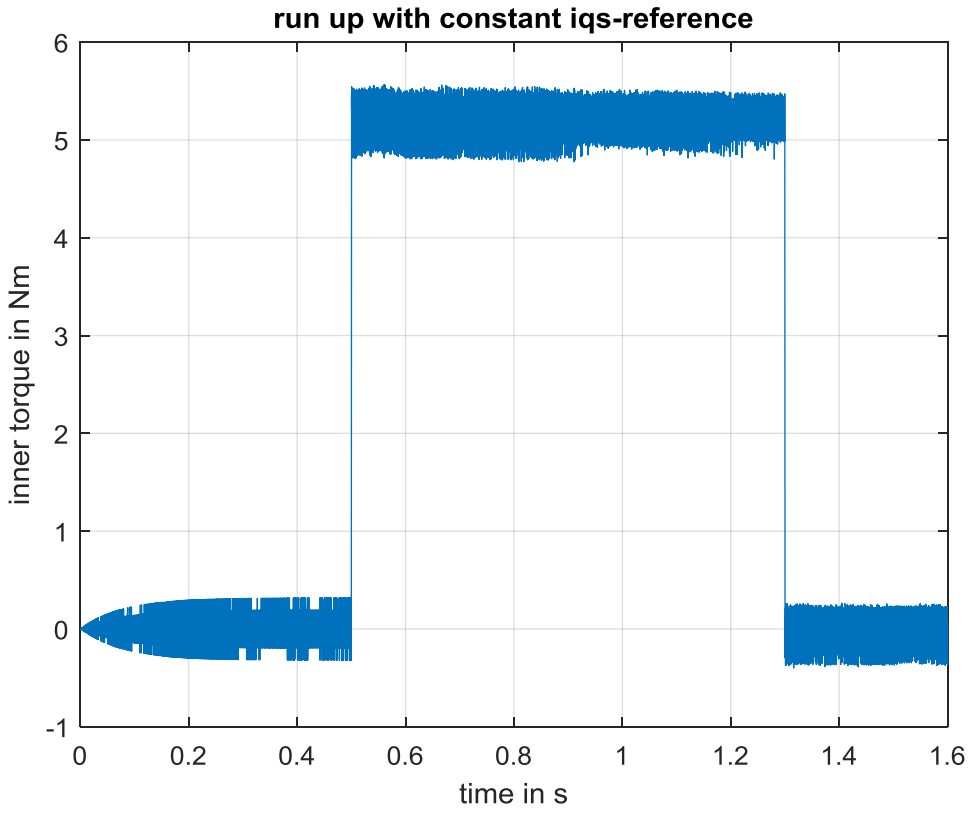

Fig. 44. Response to the electromagnetic torque to a step change in the q axis current.

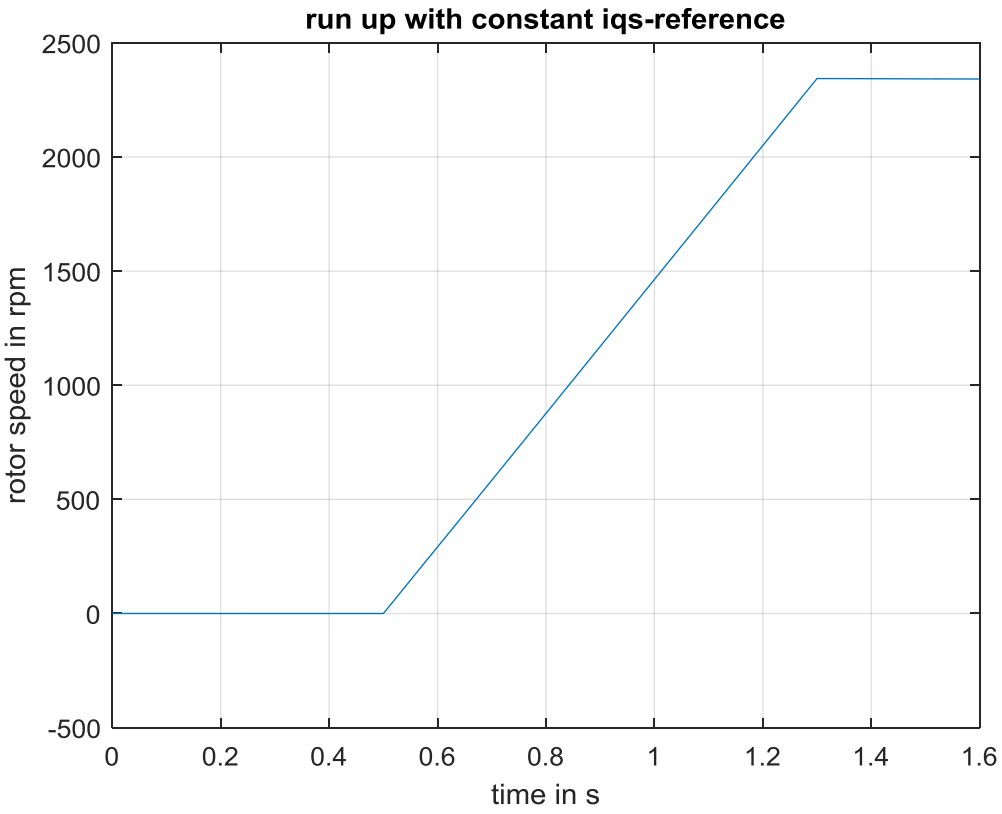

Fig. 45. Speed response of the induction machine for a step change in q axis current under FCSLP-MPC.

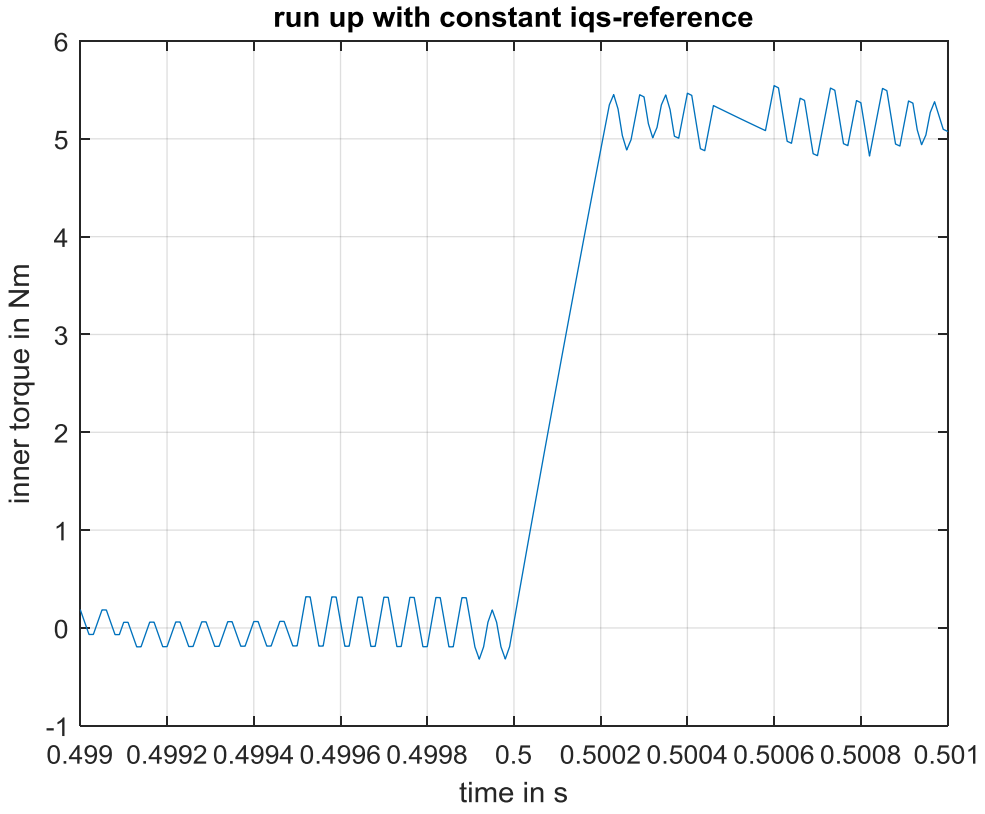

Fig. 46. Electromagnetic torque response of the induction machine under FCSLP-MPC.

The stator current of the machine in the regular abc frame is shown in fig. 47. The magnitude and frequency of the stator current is dependent on the magnitude of the q and d-axis currents and the speed of the induction machine respectively. Fig. 48 shows the stator currents of the machine in a short timescale. As can be seen, the currents have switching harmonics superimposed on the fundamental frequency current.

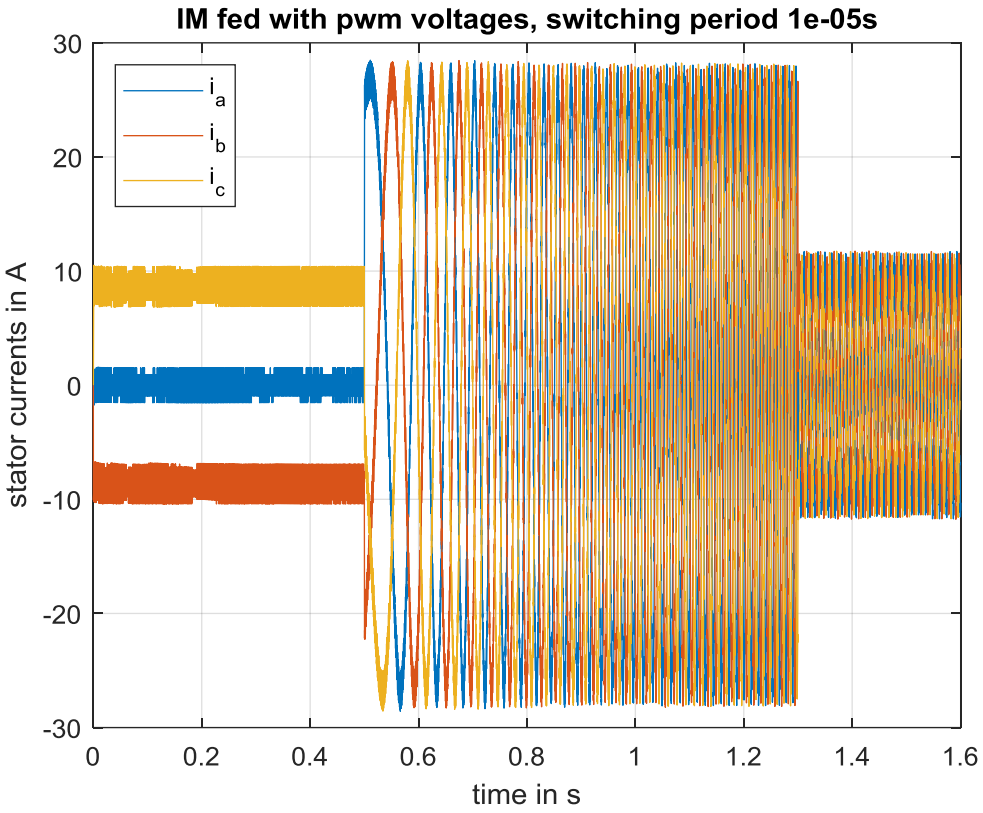

Fig. 47. Induction machine current envelope.

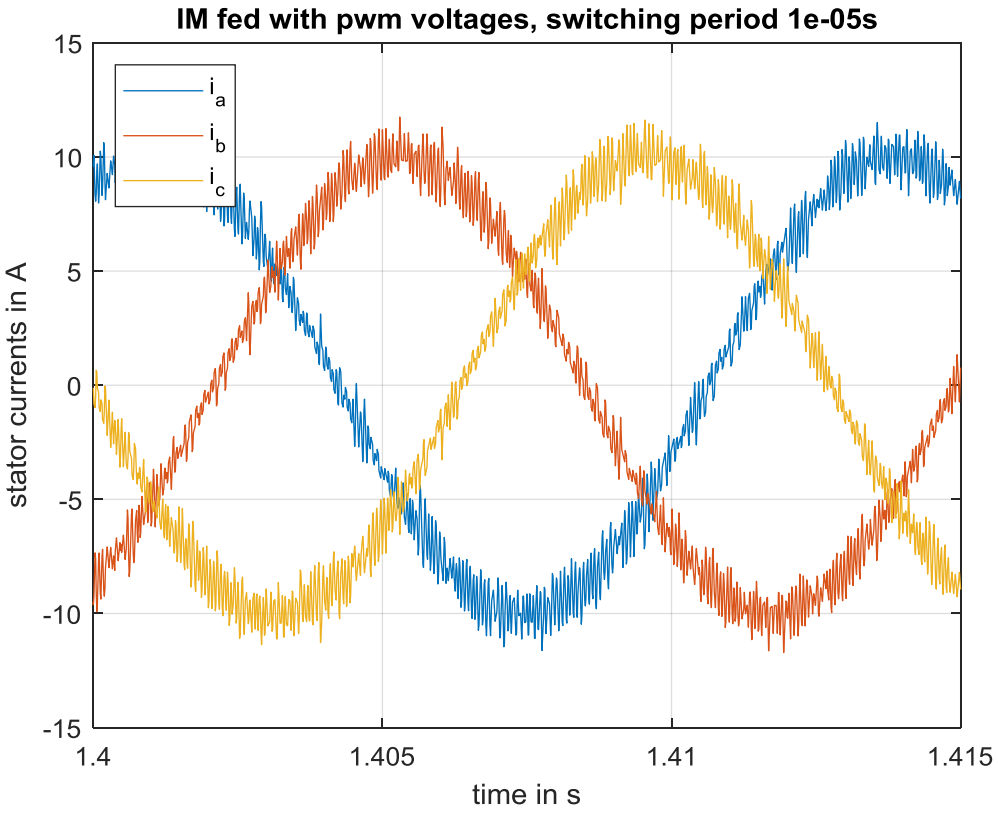

Fig. 48. Induction machine currents shown current ripples.

CHAPTER 7
ANALYSIS AND COMPARISON OF RESULTS

In this section the model predictive control schemes discussed above are compared to ascertain their performance under various operating conditions.

Though the elimination of PWM in FCS-MPC leads to a reduction in the cost of hardware and low complexity in the software design, there are certain applications that require a constant switching frequency. In such applications the variable switching frequency of the FCS-MPC is a major drawback. In this regard, the CCS-MPC is the controller of choice in constant switching frequency applications.

The dynamic response for the various schemes is analyzed first. Followed by a comparison of the performance of the various schemes when there is variation in the machine parameters.

7.1 DYNAMIC PERFORMANCE

The dynamic response of the torques for the CCS-MPC and FCS-MPC for step change in q-axis reference current is shown in fig. 49 and 50 respectively. The settling time for the CCS-MPC is 250μs and that of the FCS-MPC is 200μs. The two control schemes appear to have similar dynamic responses. The FCS-MPC is relatively faster than CCS-MPC. To achieve stability and reduce the ripple current the sampling frequency for the FCS-MPC scheme was chosen as 10μs and that of the CCS-MPC was 50μs. Therefore, even though FCS-MPC has a relatively faster response it requires a microcontroller with relatively faster clock speeds to achieve similar results with the CCS-MPC scheme. For the FCS-MPC, at every sampling instance, the voltage vector that minimizes the cost function is selected. This requires the computation the cost function for all possible switching combinations. Hence the computational burden on the controller as a result of FCS-MPC is higher compared to that of the CCS-MPC.

The FCSLP-MPC has a similar dynamic response as the FCS-MPC scheme. However, there is an increase in the computational burden on the controller due to the longer prediction and control horizons for the case of FCSLP-MPC. Longer prediction and control horizons allow for better planning of the control action and decreases the chances of running the controller into saturation. Therefore, from a dynamic response point of view a long prediction and control horizons has no special advantage. Fig. 51 shows the dynamic response of the electromagnetic torque of the FCSLP-MPC for a step change in the reference q-axis current. Fig. 52 shows the dynamic response of the electromagnetic torque of the CCSLP-MPC. From fig. 52, it can be observed that the introduction of the longer control and prediction horizon introduces a second order response to the dynamics of the controller. This leads to a longer settling time and higher percentage peak overshoot of the electromagnetic torque. The introduction of a longer prediction and control horizons therefore degrades the dynamic performance of the control system for this induction machine. The dynamic performance of the CCSLP-MPC schemes was examined with the switching frequency increased from 10kHz to 100kHz. Fig. 53. Shows the dynamic response of the machine stator currents for CCSLP-MPC for a switching frequency of 100kHz. From fig. 53, it can be observed that the dynamic response of the CCSLP-MPC is similar to the CCS-MPC when the frequency is increased.

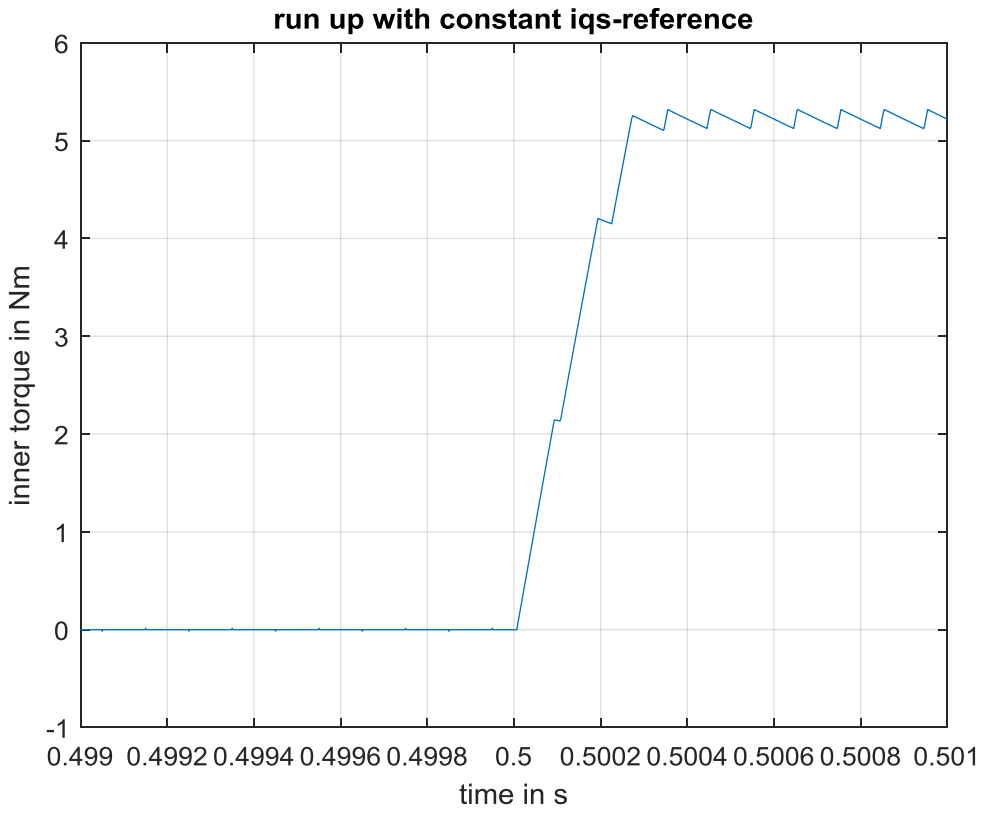

Fig. 49. Electromagnetic torque response of the induction machine under CCS-MPC.

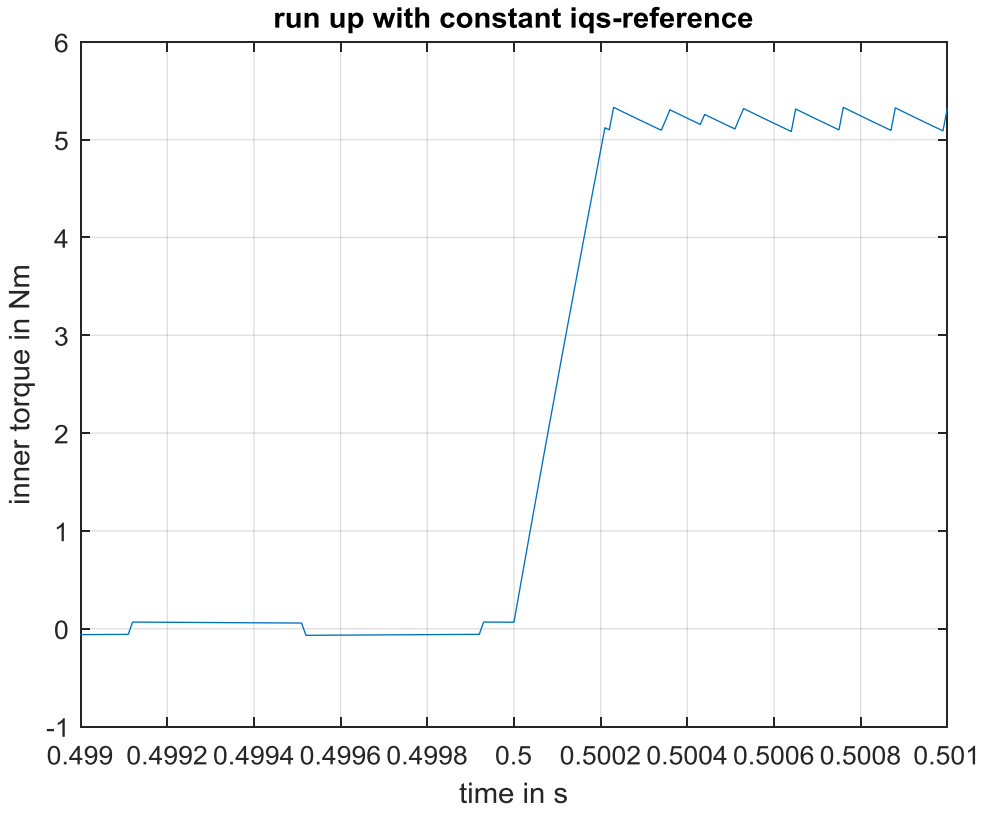

Fig. 50. Electromagnetic torque response of the induction machine under FCS-MPC.

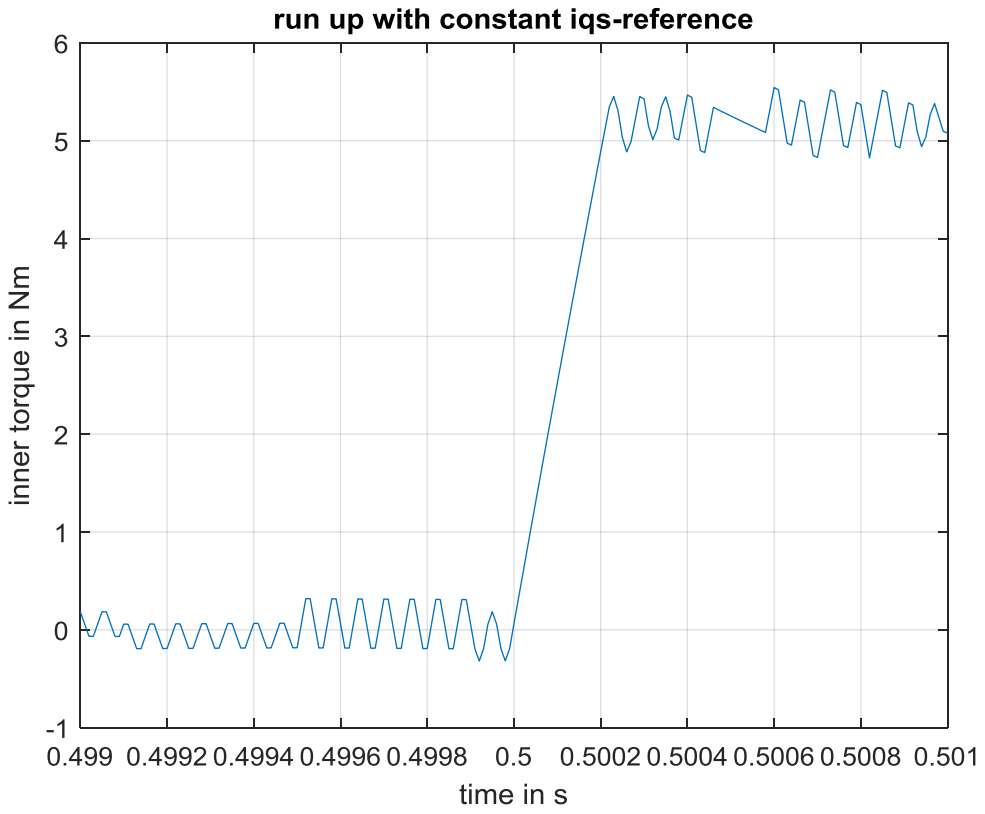

Fig. 51. Electromagnetic torque response of the induction machine under FCSLP-MPC.

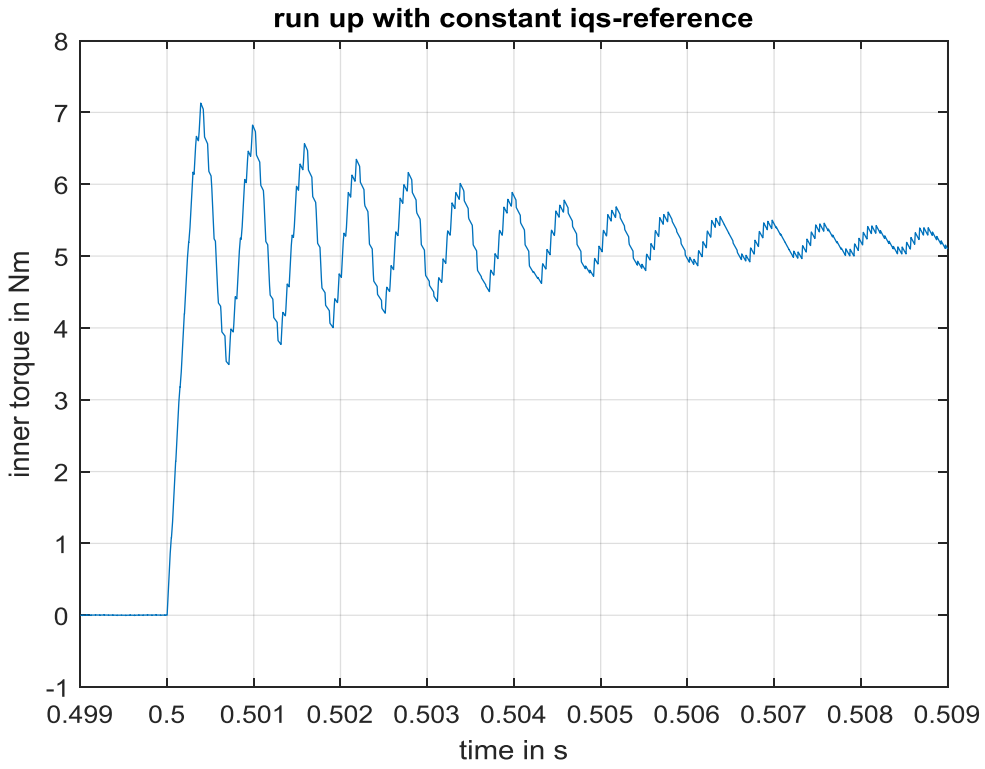

Fig. 52. Electromagnetic torque response of the induction machine under CCSLP-MPC for switching frequency of 10kHz.

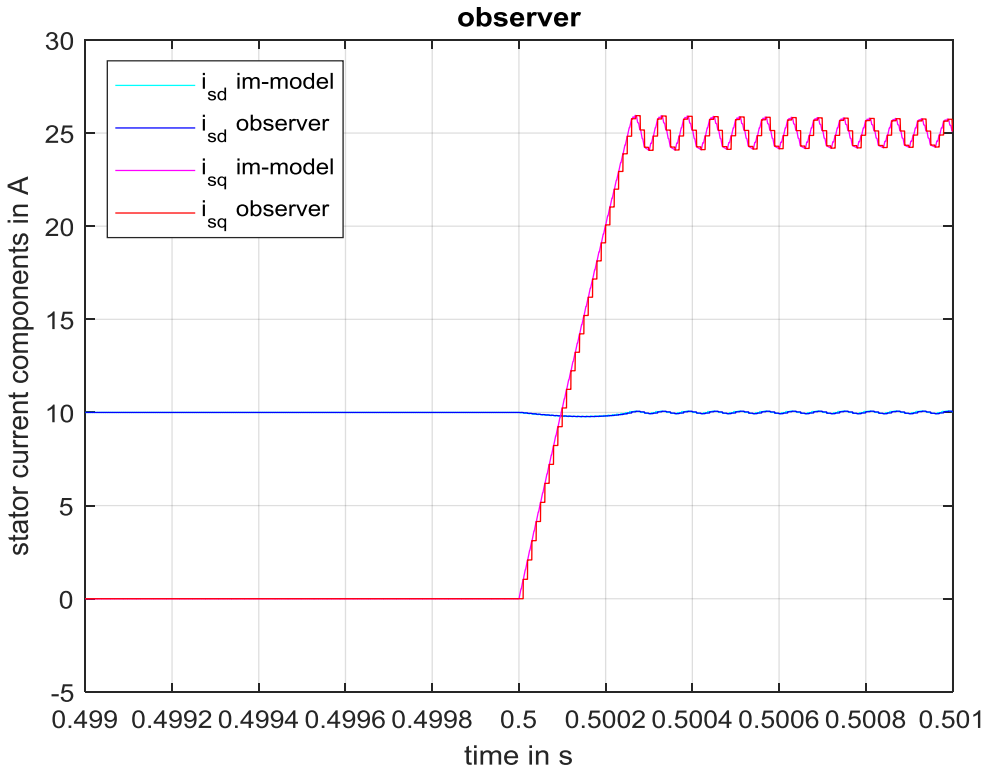

Fig. 53. Current response of the induction machine under CCSLP-MPC for switching frequency of 100kHz.

7.2 PERFORMACE UNDER MACHINE PARMETER VARIATION

The parameters of an induction machine are known to be affected by the operating conditions of the machine such as temperature and saturation effect. Model predictive control relies heavily on an accurate determination of the machine parameters. In this section the performance of various model predictive control schemes under varying machine parameters is determined.

The performance of the induction machine stator current under CCS-MPC scheme is shown in fig. 54. The stator resistance of the machine was reduced to half of its original value. As can be observed, the dynamics of the controller remain the same. However, the deviation of the steady state value from the reference value increases. The steady state value changed from 25A to 25.7A. This represents a deviation of 0.7A from the reference value. Fig. 55 shows the performance of FCS-MPC when the stator resistance of the machine was reduced to half of its original value. As can be observed there is a change in the steady state value from 25A to 25.1A. Therefore FCS-MPC is more robust to variation in stator resistance.

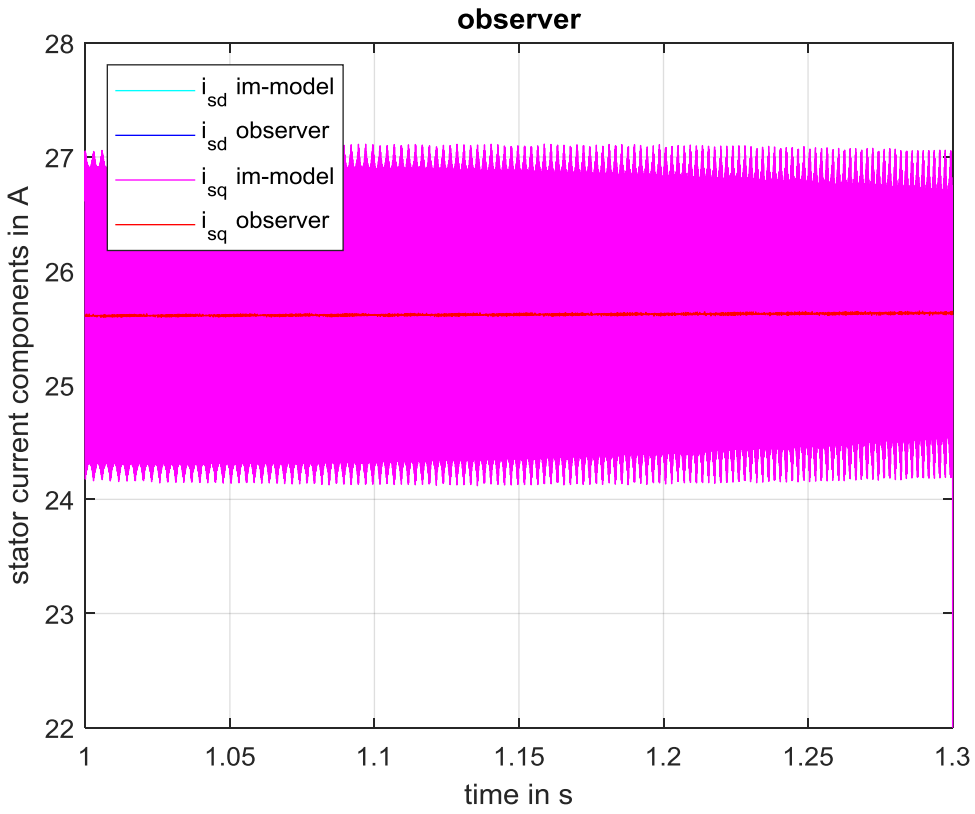

Fig. 54. Stator current for CCS-MPC with 50% decrease in stator resistance.

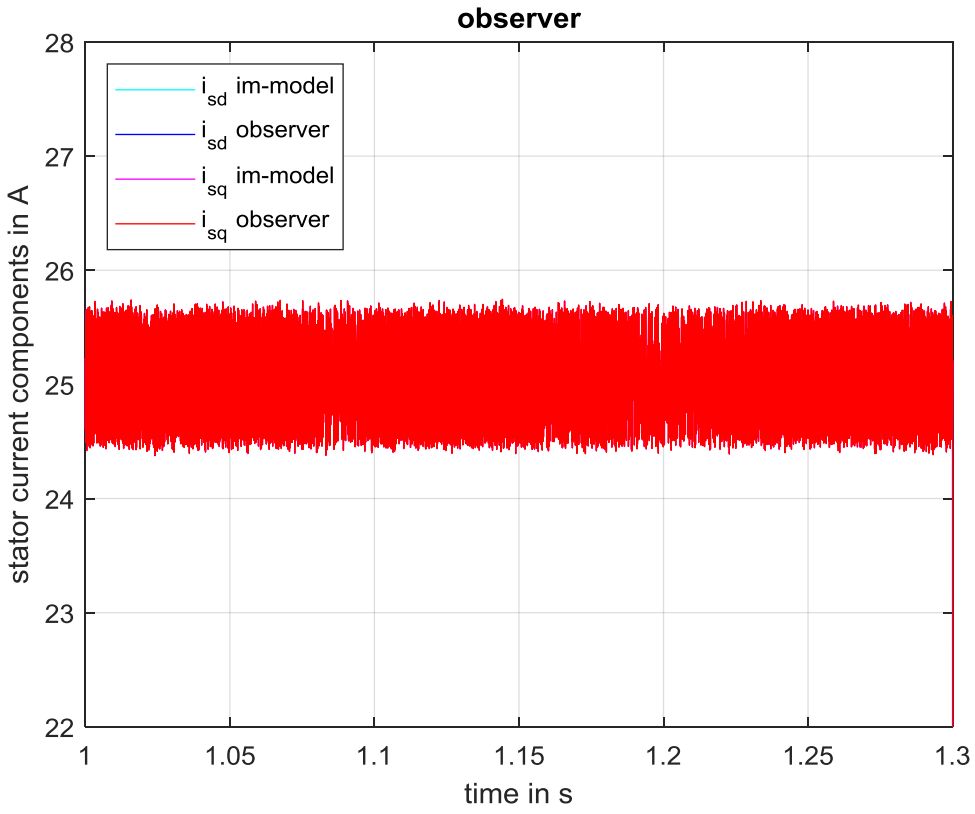

Fig. 55. Stator current for FCS-MPC with 50% decrease in stator resistance

The performance of the induction machine stator current under CCS-MPC scheme is shown in fig. 56. The stator resistance of the machine was increased to two times its original value. Under this condition also, the dynamics of the controller remain the same. However, the deviation of the steady state value from the reference value increases. The steady state value changed from 25A to 24.6A. This represents a deviation of 0.4A from the reference value. Fig. 57 shows the performance of FCS-MPC when the stator resistance of the machine was increased to two times its original value. As can be observed there was no change in the steady state value of the q-axis current. Therefore, in this case also FCS-MPC is more robust to variation in stator resistance.

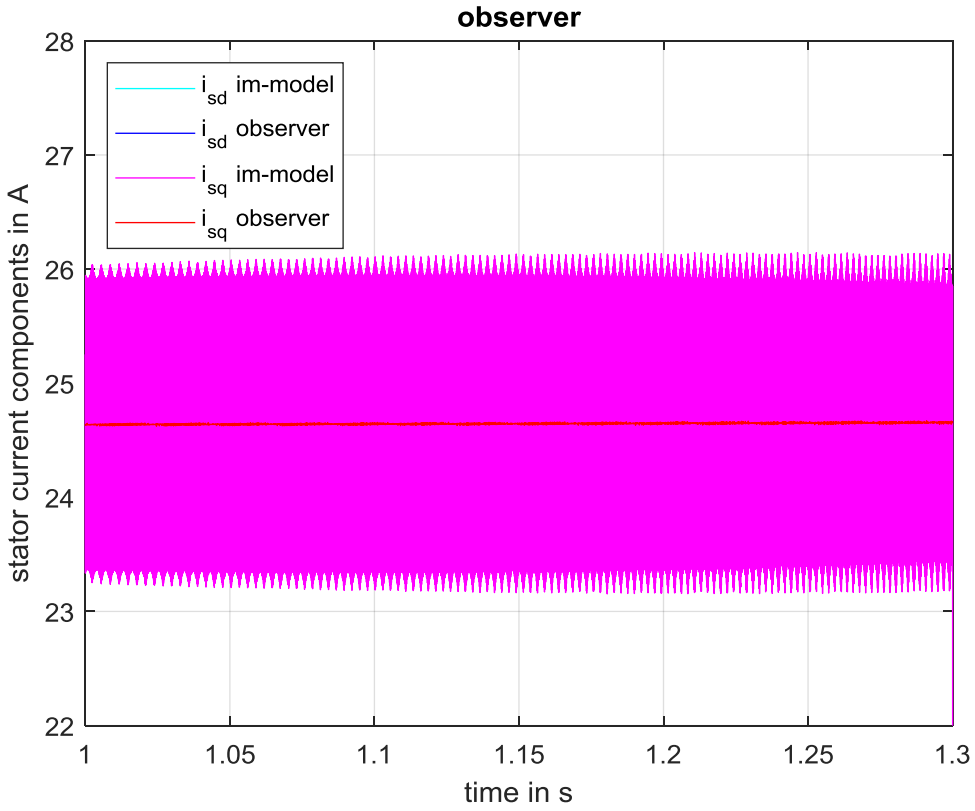

Fig. 56. Stator current for CCS-MPC with 100% increase in stator resistance.

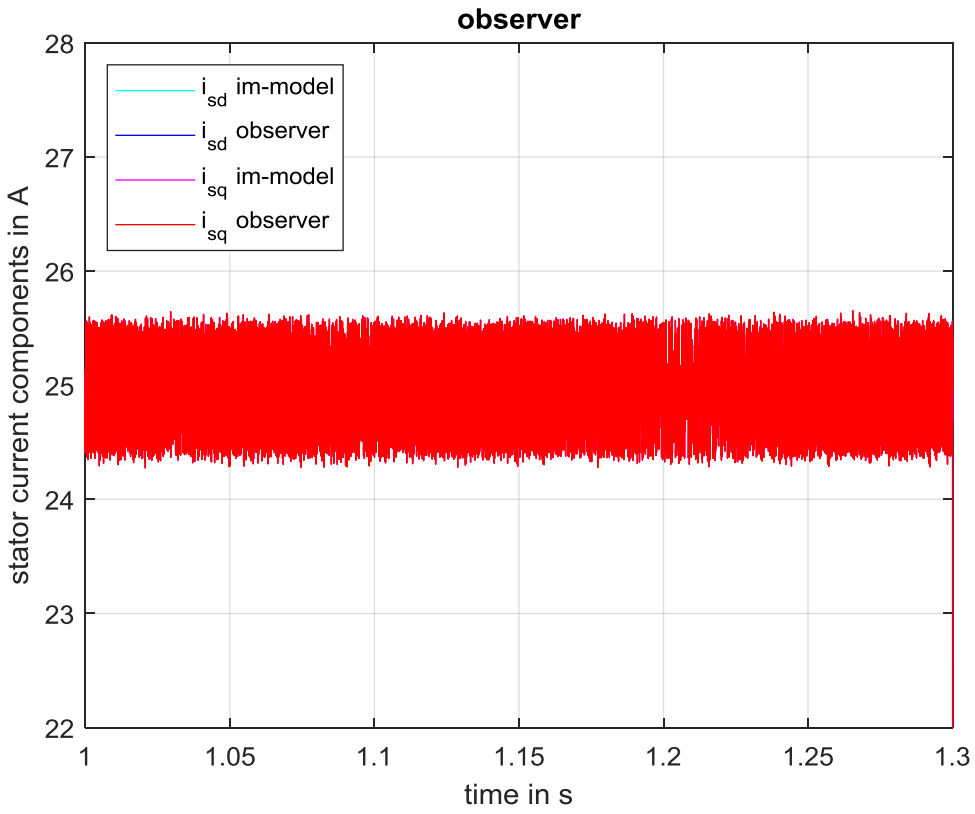

Fig. 57. Stator current for FCS-MPC with 50% increase in stator resistance.

Fig. 58 shows the performance of the induction machine stator current under CCS-MPC scheme for a change in the rotor resistance. The rotor resistance of the machine was decreased to half its original value. The controller is more sensitive to a variation in rotor resistance relative to the performance under a change stator resistance. The is an increase in deviation of the steady state value from the reference value. Fig. 59 shows the performance of FCS-MPC when the rotor resistance of the machine was decreased to half its original value. Here again FCS-MPC appears to be relatively more robust to variation in stator resistance when compared to CCS-MPC.

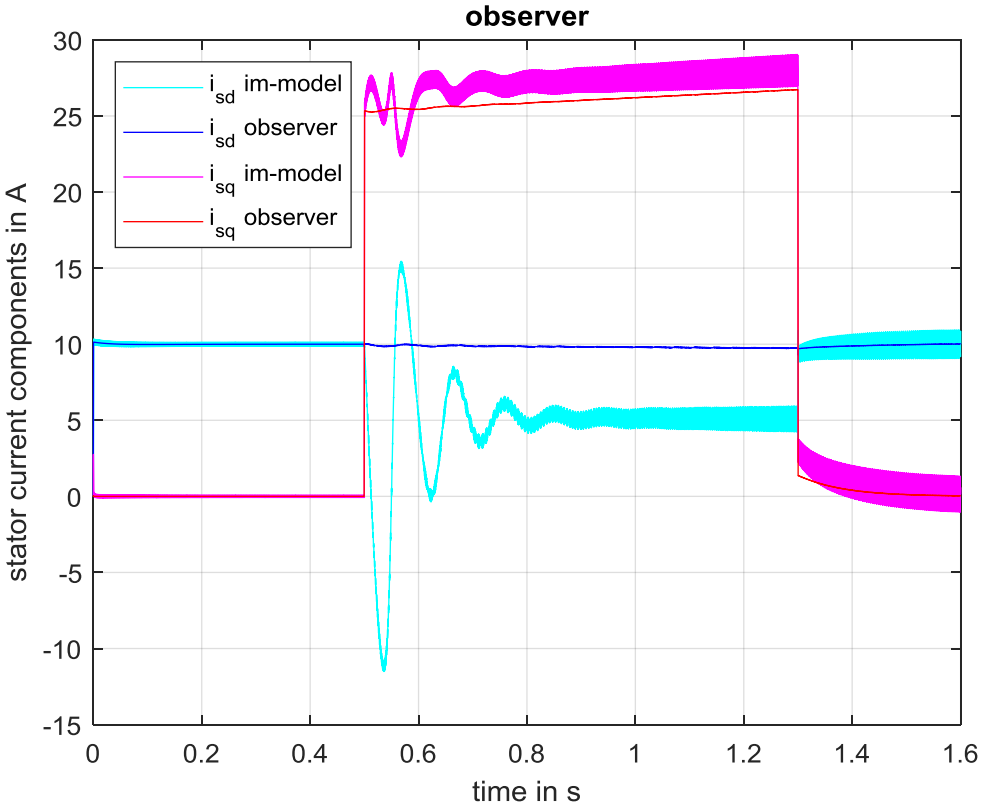

Fig. 58. Stator current for CCS-MPC with 50% decrease in rotor resistance

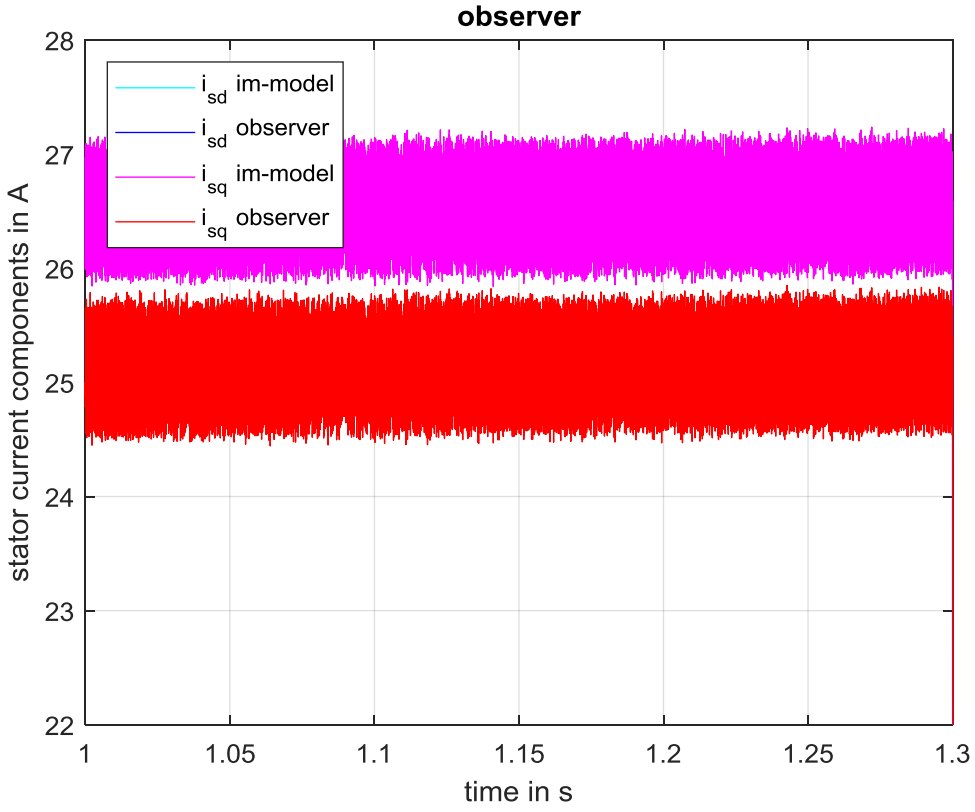

Fig. 59. Stator current for CCS-MPC with 50% decrease in rotor resistance

From the analysis above it can be observed that FCS-MPC performs better when the parameters of the machine change due to a change in the operating conditions of the machine. Both the CCS-MPC and the FCS-MPC schems are more sensitive to variation in rotor resistance when compared to a variation in stator resistance.

CHAPTER 8
MODEL PREDICTIVE CONTROL OF INDUCTION MACHINE WITH SINE LOSS FILTER

Despite the numerous advantages of FCS-MPC, the non-constant switching frequency of this control method is a major drawback when it comes to control of an induction machine with an input filter. The input filter is designed such that its resonance frequency falls in range were there is low probability for resonant modes of the filter to be excited. Since in FCS-MPC the switching frequency is not constant, there is a greater possibility of the converter operating at a frequency where the resonant modes of the input filter are excited. To avoid this, the CCS-MPC scheme is chosen for the control of the induction machine with input sine loss filter. In the initial approach the machine is simulated together with the designed input filter to ascertain the accuracy of the developed machine model with an input filter.

8.1 FILTER DESIGN AND OPEN LOOP SIMULATION

For the choice of filter parameters, the selection of the inductance and capacitance is made such that the resonant frequency of the resulting LC filter is less than the switching frequency of the inverter. Also, the resonant frequency must be higher than the fundamental frequency of the inverter output voltage. i.e.

$$f_e < f_{res} < f_{sw} \tag{73}$$

Where f_e, f_{res} and f_{sw} are the fundamental frequency of the inverter output voltage, the resonant frequency and the switching frequency respectively.

The resonant frequency of an LC filter is given by:

$$f_{res} = \frac{1}{2\pi\sqrt{LC}} \tag{74}$$

In [] the selection the inductor value was based on the voltage drop to be tolerated on the series inductor. The voltage drop should be as small as possible to increase the efficiency of the drive system. The choice of capacitance is made such that the current flowing through the capacitor does not exceed 10% or rated current of the drive system.

Fig. 60 shows the stator phase “a” current of the induction machine as a function of time. The transient and steady state envelope of the current can be seen from this figure. The envelope of the stator current varies during transient condition due to interaction between stator and rotor electrical transients. Fig, 61 shows the stator phase “a” steady state current of the machine as a function of time. As expected, the harmonic content in the current is eliminate due to the presence of the designed input filter.

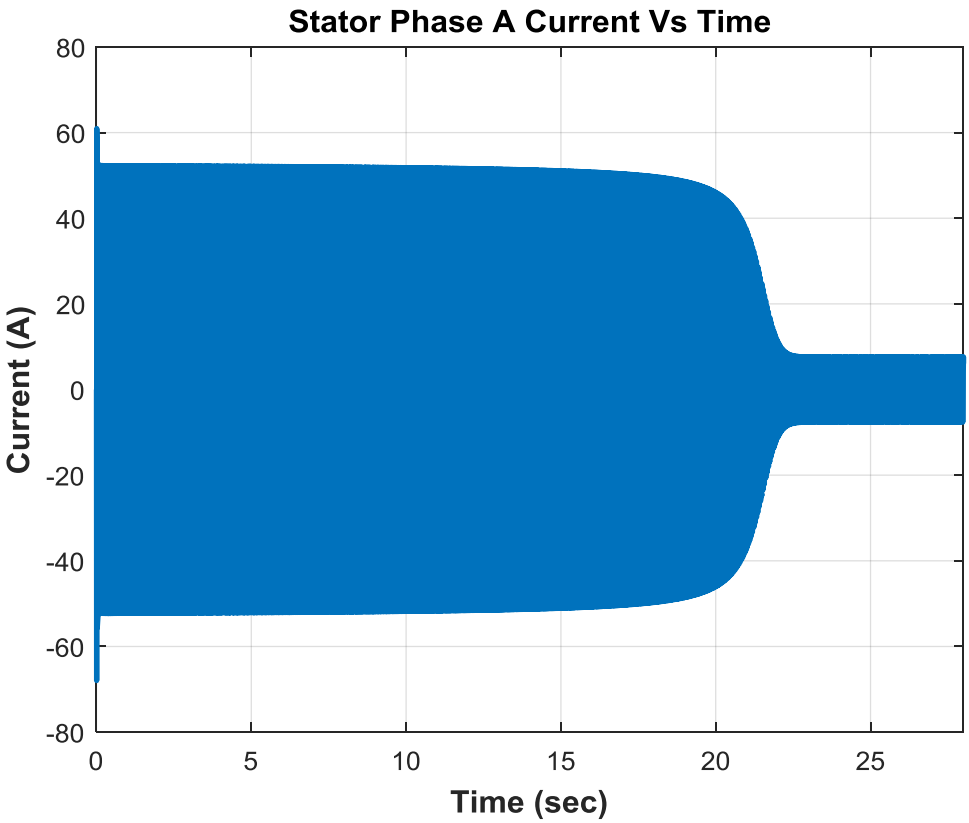

Fig. 60. Stator Phase "a' current envelope as function of time

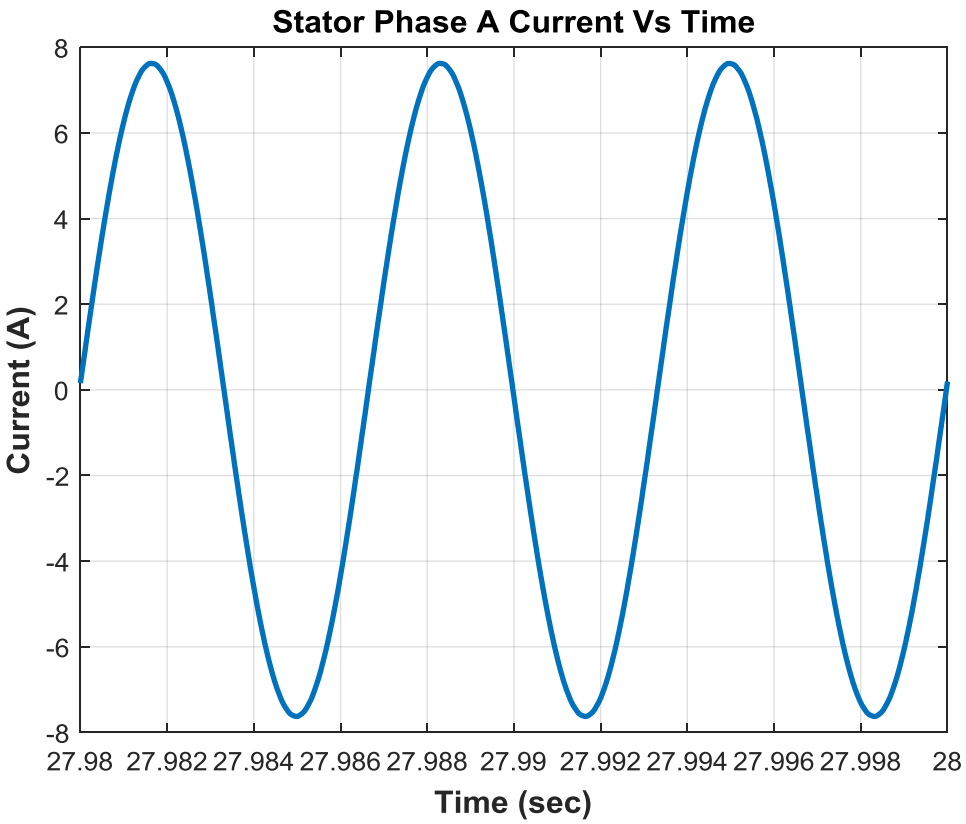

Fig. 61. Steady state phase "a" current waveform as function of time

The electromagnetic torque at start has a positive average value as shown in fig. 62. Rated torque is developed close to the synchronous speed, therefore this induction machine is a low slip induction machine.

Fig. 63 shows the rotor electrical angular speed of the induction machine. Because windage losses are not present the machine accelerates to synchronous speed. The machine is low horsepower machine hence the speed of the rotor is easily damped and does not exceed the synchronous speed.

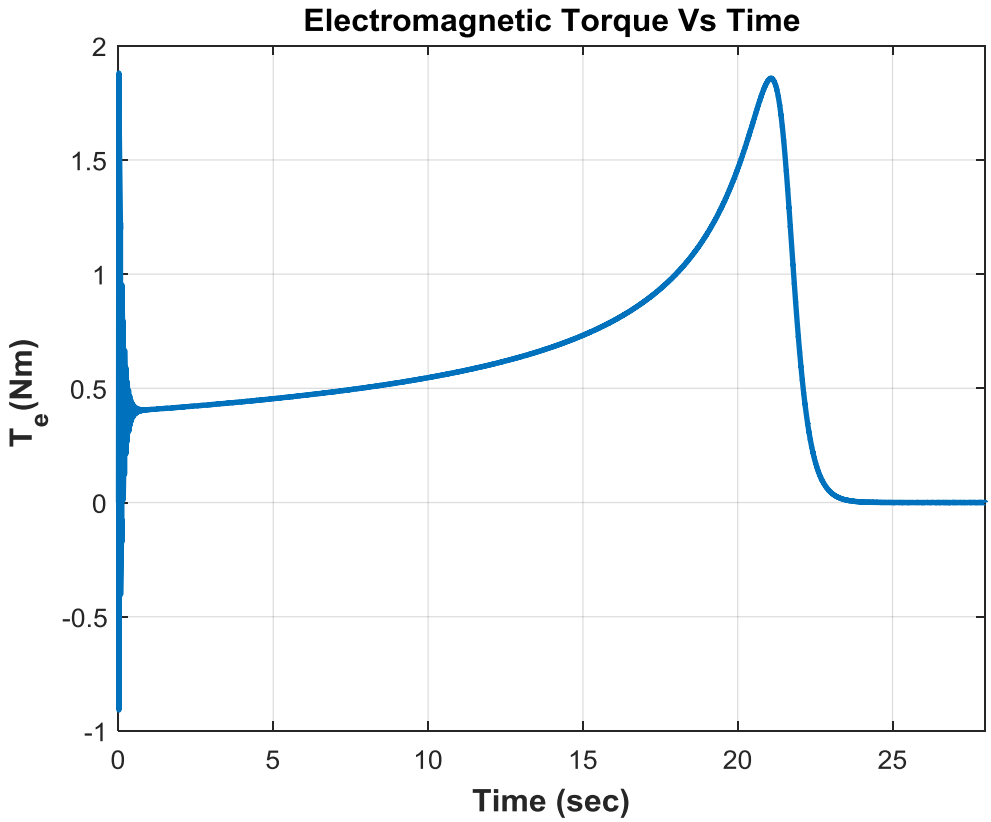

Fig. 62. Electromagnetic torque of induction machine as function of time

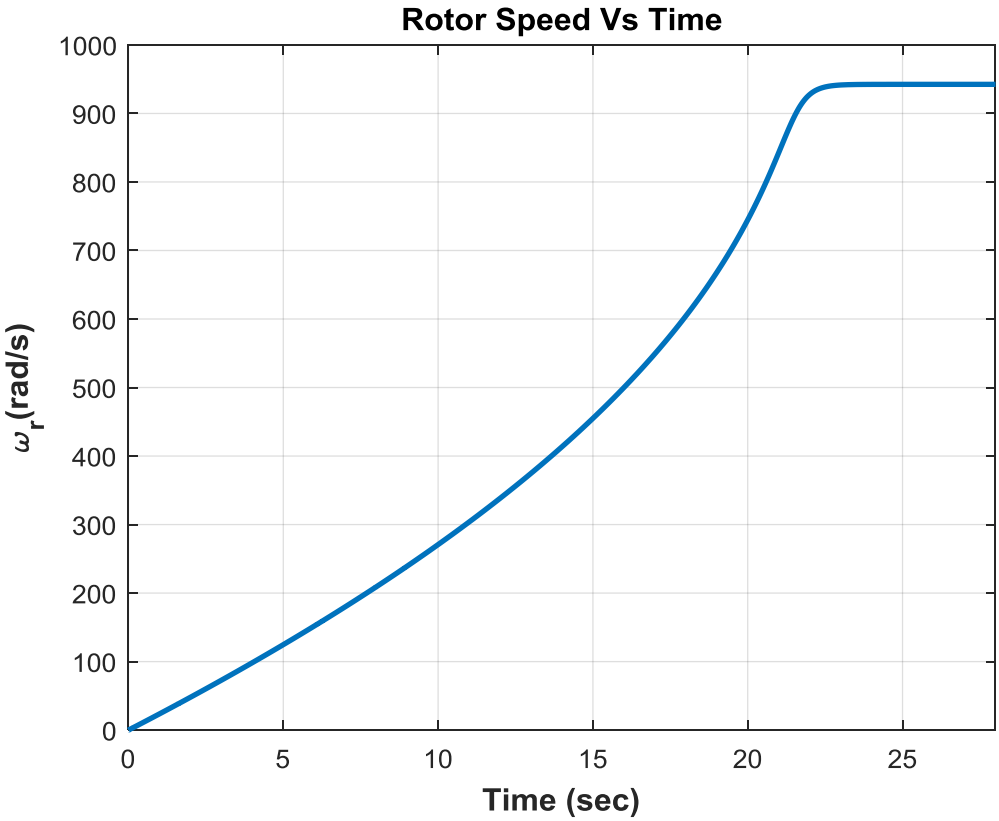

Fig. 63. Rotor electrical angular speed of the induction machine as a function of time.

8.2 CONTROLLER DESIGN

Now that the open loop model of the designed drive system has been verified, the next step is to design the controller for the system. In this system, besides the machine states, it is also important to control the filter states. The states of the filter are given by the series inductor current and shunt capacitor voltage. This introduces additional states for the control system and increases the complexity of the controller design. Model predictive control is well suited for multivariable control and hence its advantage over conventional control methods. The structure of the designed controller is given in fig. 64.

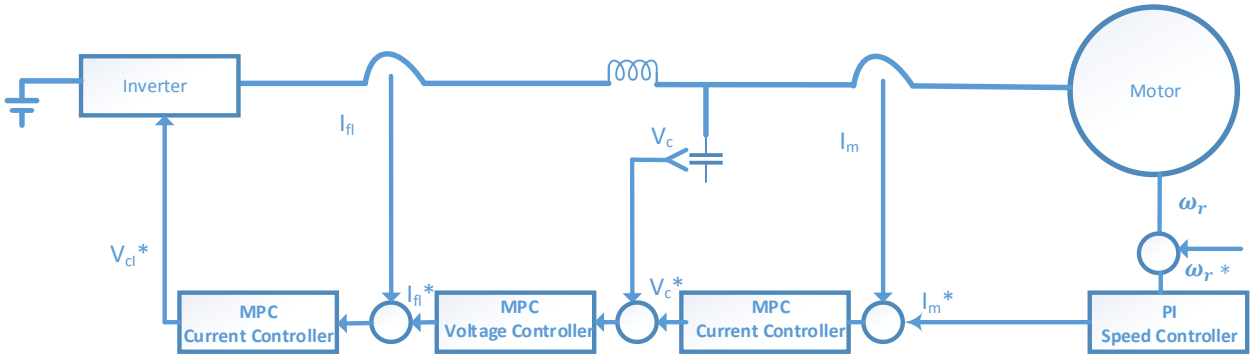

Fig. 64 Structure of proposed controller

Because the dynamics of the speed of the induction machine is slow, it can be controlled with a regular PI controller. The faster dynamics will be controlled with the CCS-MPC controller. The machine currents are controlled based on which the reference for the filter capacitor voltages is generated. The outputs of the stator current controller forms the reference input for the control of the capacitor voltages. The outputs of the capacitor voltage controller serve as reference for the control of the filter inductor currents. The output of the filter controller generates the reference voltage for the inverter PWM.

For the control of the machine currents, the state-space model of the system can be derived and is as shown below:

$$\begin{bmatrix} pi_{ds} \\ pi_{qs} \end{bmatrix} = \begin{bmatrix} -\frac{r}{L_\sigma} & \omega_e \\ -\omega_e & -\frac{r}{L_\sigma} \end{bmatrix} \begin{bmatrix} i_{ds} \\ i_{qs} \end{bmatrix} + \begin{bmatrix} \frac{1}{L_\sigma} & 0 \\ 0 & \frac{1}{L_\sigma} \end{bmatrix} \begin{bmatrix} v_{ds} \\ v_{qs} \end{bmatrix} + \begin{bmatrix} -\frac{\omega_r L_M}{L_\sigma L_r}\lambda_r \\ \frac{r_r L_M}{L_\sigma L_r^2}\lambda_r \end{bmatrix} \tag{75}$$

For the filter capacitor voltage control, the state-space model is derived as:

$$\begin{bmatrix} pV_{cd} \\ pV_{cq} \end{bmatrix} = \begin{bmatrix} 0 & \omega_e \\ -\omega_e & 0 \end{bmatrix} \begin{bmatrix} V_{cd} \\ V_{cq} \end{bmatrix} + \begin{bmatrix} \frac{1}{C} & 0 \\ 0 & \frac{1}{C} \end{bmatrix} \begin{bmatrix} I_d \\ I_q \end{bmatrix} + \begin{bmatrix} -\frac{I_{ds}}{C} \\ -\frac{I_{qs}}{C} \end{bmatrix} \tag{76}$$

The state-space model for the filter inductor current control is similarly derived as:

$$\begin{bmatrix} pV_{cd} \\ pV_{cq} \end{bmatrix} = \begin{bmatrix} 0 & \omega_e \\ -\omega_e & 0 \end{bmatrix} \begin{bmatrix} I_d \\ I_q \end{bmatrix} + \begin{bmatrix} \frac{1}{L} & 0 \\ 0 & \frac{1}{L} \end{bmatrix} \begin{bmatrix} V_d \\ V_q \end{bmatrix} + \begin{bmatrix} -\frac{V_{cd}}{L} \\ -\frac{V_{cq}}{L} \end{bmatrix} \tag{77}$$

The equations obtained above are digitized using Euler method and the discrete state space model is derived.

From the above equations and using Matlab/Simulink platform for the simulation, the performance of the designed controller can be evaluated. The parameters of the designed filter are as given in table. 2.

TABLE 2.

FILTER PARAMETERS AND SWITCHING FREQUENCY

Quantity	Value
Filter Inductor	$400\mu H$
Filter Capacitor	$500\mu F$
F_{sw}	6000kHz

To evaluate the performance of the designed controller, the simulation was performed at fixed rotor speed of 200rad/s. The reference q-axis current of the machine was varied from 0A to 5A at 1.6348s and then from 5A to 10A at 2.7s. The d-axis current was kept constant at 5A.

Fig. 65 shows the stator phase "a" current envelope of the machine. As can be seen, as the reference q-axis current increases, there is a corresponding increase in the amplitude of the stator current of the machine. Fig. 66 shows the stator current for a shorter time scale showing two cycles of the current waveform. The harmonic content of the waveform is eliminated by the introduction of the designed filter. To assess the dynamic performance of the designed controller, the d and q-axis currents have been provided in fig. 67 and 68 respectively. Both currents follow their reference values as expected. However, there is a significant error between the reference and the commanded currents. There error is due to the fact that designed controller is equivalent to a p-type controller when compared to a regular PID controller. To eliminate this errors, integral action will have to be introduced to the control design. One approach to achieve this is to use the incremental dynamics of the system in the controller design rather than the actual dynamics of the system. In later works, this kind of controller will be explored. From fig. 69, it is observed that the current takes $400\mu s$ to reach its study state value. This results goes to show the fast dynamics of the model predictive controller when compared to a PI type controller. The commanded electromagnetic torque of the system is shown in fig. 69. The ripple in the commanded torque has been eliminated by the introduction the sine loss filter at the converter output.

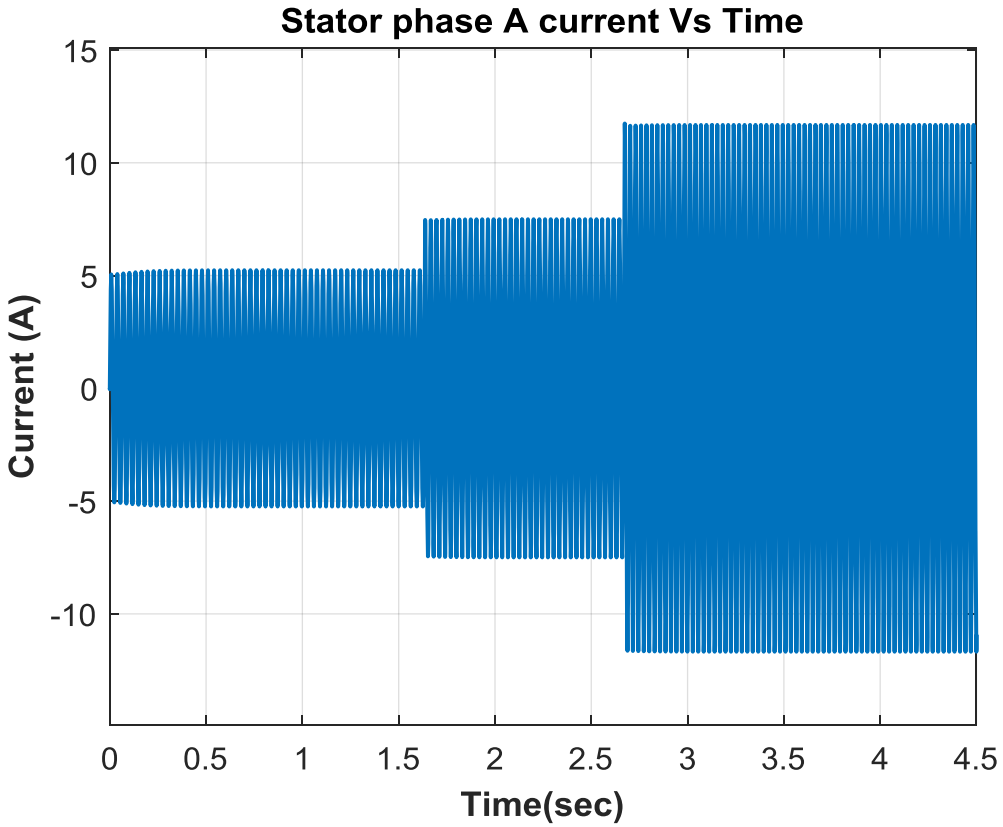

Fig. 65. Stator Phase "a' current envelope as function of time

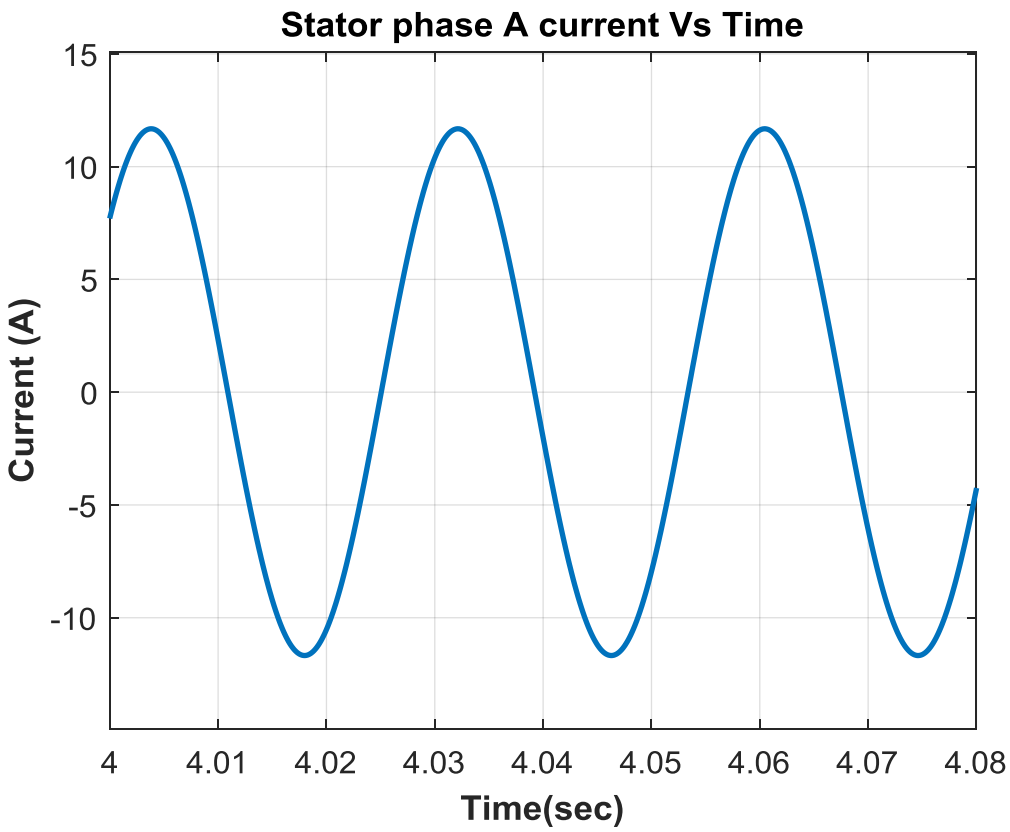

Fig. 66. Stator Phase "a' current waveform as function of time

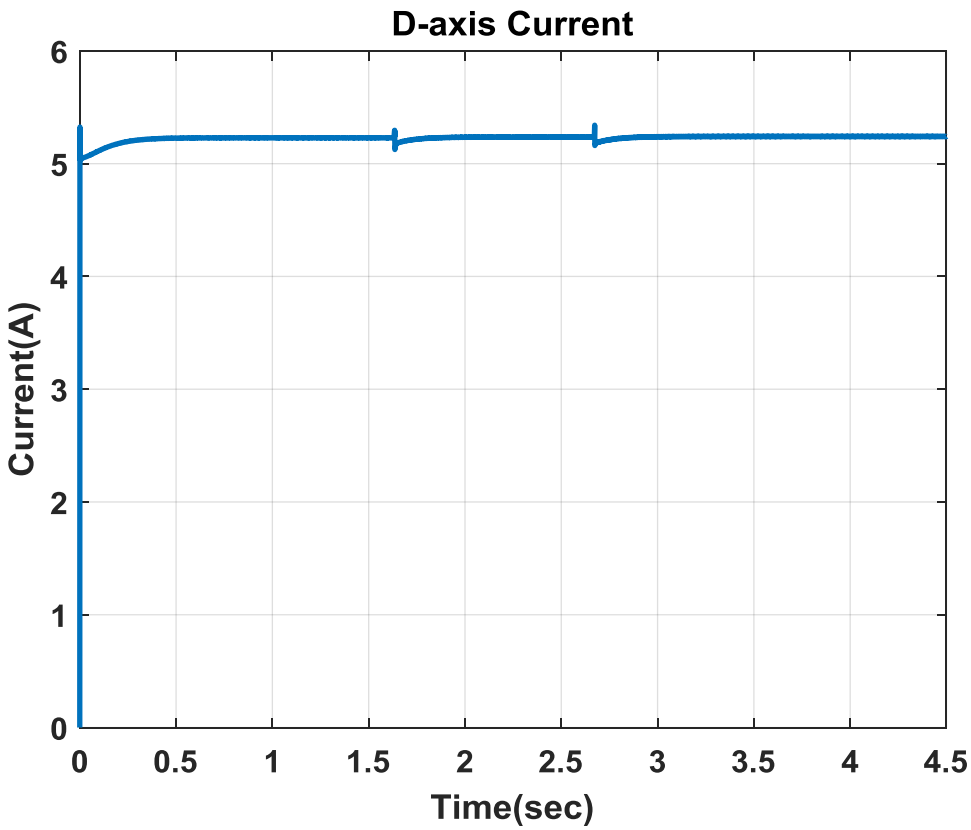

Fig. 67. D-axis current as function of time

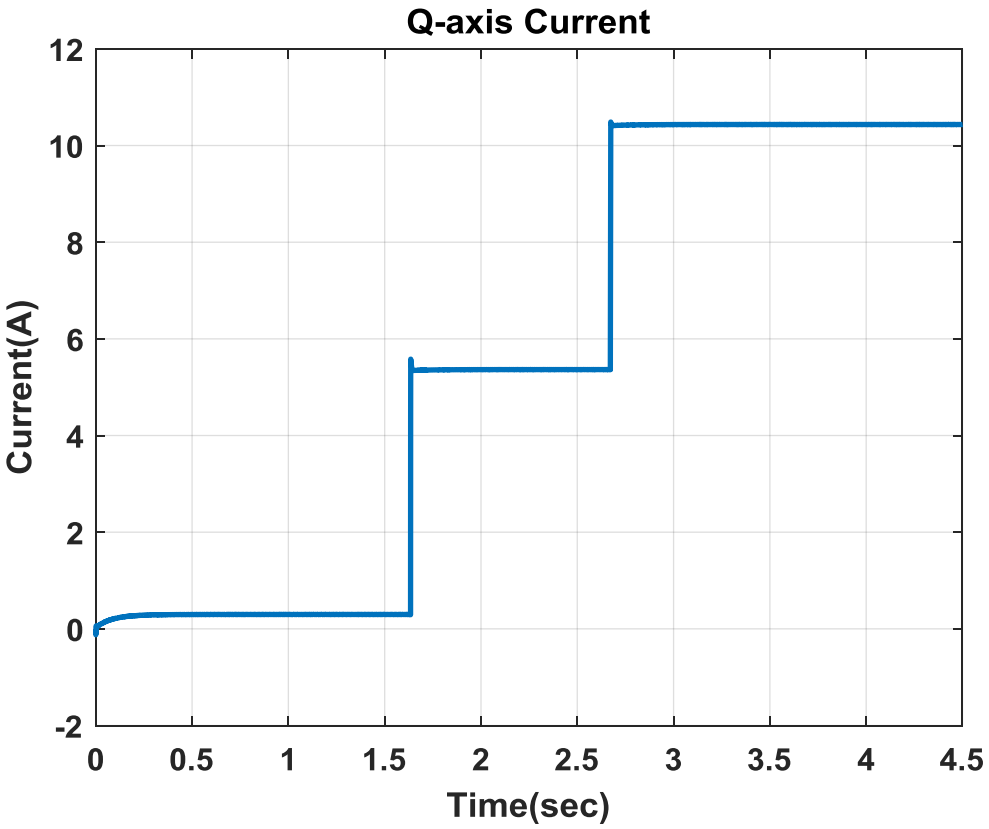

Fig. 68. Q-axis current as function of time

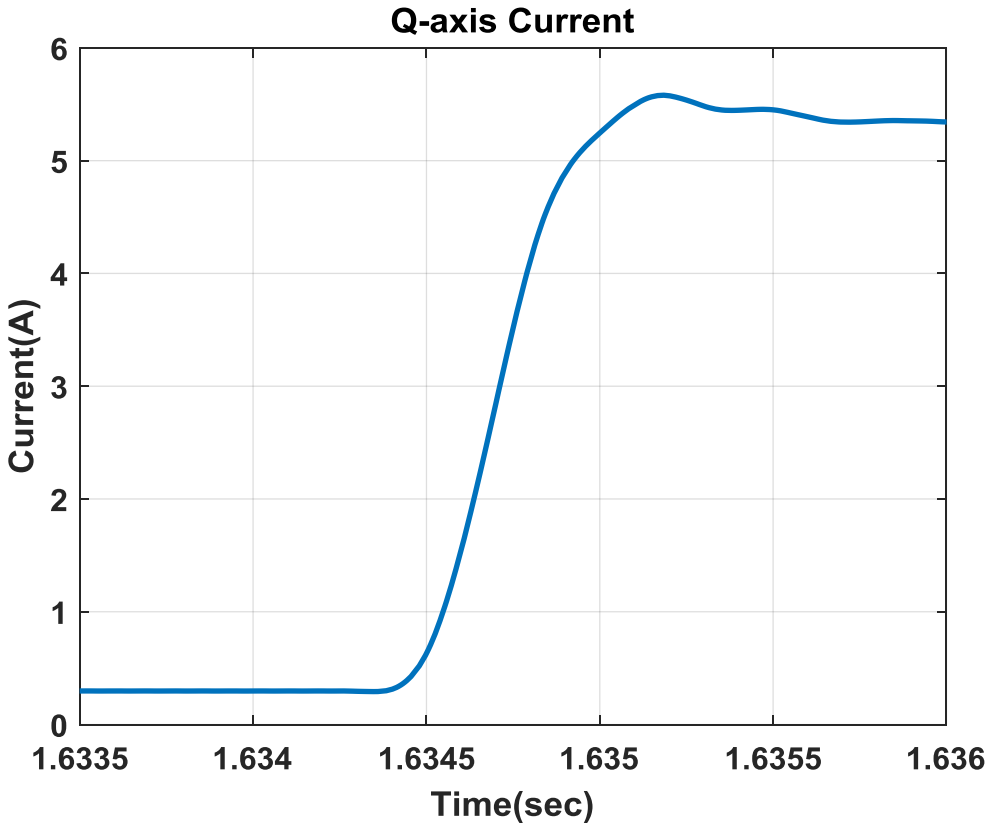

Fig. 69. Q-axis current as function of time showing dynamic performance

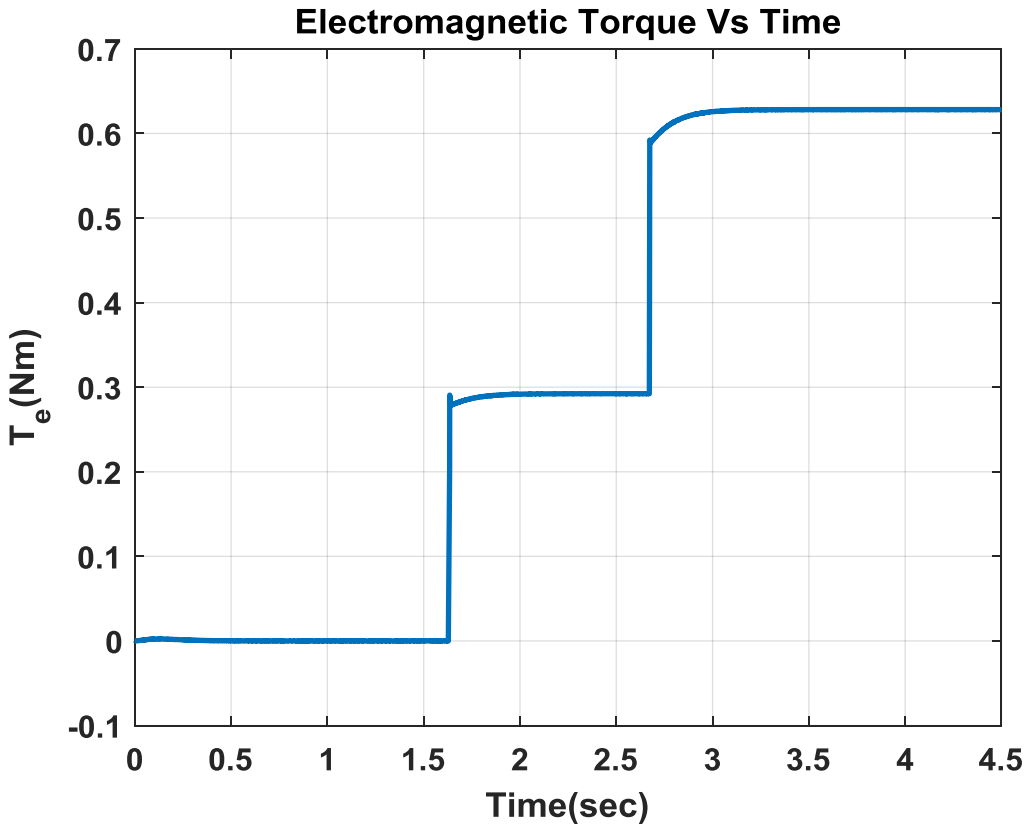

Fig. 70. Electromagnetic Torque as function of time

Conclusion and Further Work

In this work, the performance of the two main types of model predictive control of an induction machine was investigated. First, the principle behind the FCS-MPC was given. The FCS-MPC controller was developed for the current (torque) control of an induction machine. The performance of the FCS-MPC was examined using Matlab/Simulink. The CCS-MPC controller was developed next for the current (torque) control of an induction machine. The models of the two controllers with long prediction and control horizon were developed and their performance assessed. It was shown that the FCS-MPC outperforms its counterpart in terms of settling speed and robustness to machine parameter variation. Both control systems performed better under variation in stator resistance as compared to a variation in rotor resistance. Despite the stated advantages of the FCS-MPC schemes over their CCS-MPC counterparts, they are not suited for applications which require constant switching frequency. For the control of a machine with input filter, the variable switching frequency is likely to excite resonance in the input filter. Therefore for applications with input filter, the CCS-MPC was selected. The performance of the designed controller for an induction machine with input filter was assessed.

In the development of the controller for the machine control, it was assumed that all the states are measured. It is recommended that further work be carried to ascertain the performance of the designed controller with an estimation of some of the filter and machine states. This will reduce the number of sensors required for measurement of these states and elimination of the errors associated with such measurements.

REFERENCES

[1] Taeg-Joon Kweon and Dong-Seok Hyun, "High-performance speed control of electric machine using low-precision shaft encoder," in *IEEE Transactions on Power Electronics*, vol. 14, no. 5, pp. 838-849, Sept. 1999.

[2] D. Casadei, F. Profumo, G. Serra and A. Tani, "FOC and DTC: two viable schemes for induction motors torque control," in *IEEE Transactions on Power Electronics*, vol. 17, no. 5, pp. 779-787, Sept. 2002.

[3] L. Harnefors, "Design and analysis of general rotor-flux-oriented vector control systems," in *IEEE Transactions on Industrial Electronics*, vol. 48, no. 2, pp. 383-390, April 2001.

[4] G. S. Buja and M. P. Kazmierkowski, "Direct torque control of PWM inverter-fed AC motors - a survey," in *IEEE Transactions on Industrial Electronics*, vol. 51, no. 4, pp. 744-757, Aug. 2004.

[5] Y. Zhang, J. Zhu, Z. Zhao, W. Xu and D. G. Dorrell, "An Improved Direct Torque Control for Three-Level Inverter-Fed Induction Motor Sensorless Drive," in *IEEE Transactions on Power Electronics*, vol. 27, no. 3, pp. 1502-1513, March 2012.

[6] B. Singh, S. Jain and S. Dwivedi, "Torque ripple reduction technique with improved flux response for a direct torque control induction motor drive," in *IET Power Electronics*, vol. 6, no. 2, pp. 326-342, Feb. 2013.

[7] Y. Zhang, B. Xia and H. Yang, "Performance evaluation of an improved model predictive control with field oriented control as a benchmark," in *IET Electric Power Applications*, vol. 11, no. 5, pp. 677-687, 5 2017.

[8] Y. Zhang, H. Yang and B. Xia, "Model predictive torque control of induction motor drives with reduced torque ripple," in *IET Electric Power Applications*, vol. 9, no. 9, pp. 595-604, 11 2015.

[9] F. Wang, S. Li, X. Mei, W. Xie, J. Rodríguez and R. M. Kennel, "Model-Based Predictive Direct Control Strategies for Electrical Drives: An Experimental Evaluation of PTC and PCC Methods," in *IEEE Transactions on Industrial Informatics*, vol. 11, no. 3, pp. 671-681, June 2015.

[10] F. Wang, X. Mei, J. Rodriguez and R. Kennel, "Model predictive control for electrical drive systems-an overview," in *CES Transactions on Electrical Machines and Systems*, vol. 1, no. 3, pp. 219-230, September 2017.

[11] C. Garcia, J. Rodriguez, C. Silva, C. Rojas, P. Zanchetta and H. Abu-Rub, "Full Predictive Cascaded Speed and Current Control of an Induction Machine," in *IEEE Transactions on Energy Conversion*, vol. 31, no. 3, pp. 1059-1067, Sept. 2016.

[12] Y. Zhang and C. Qu, "Model Predictive Direct Power Control of PWM Rectifiers Under Unbalanced Network Conditions," in *IEEE Transactions on Industrial Electronics*, vol. 62, no. 7, pp. 4011-4022, July 2015.

[13] D. Busse, J. Erdman, R. J. Kerkman, D. Schlegel and G. Skibinski, "The effects of PWM voltage source inverters on the mechanical performance of rolling bearings," *Proceedings of Applied Power Electronics Conference. APEC '96*, San Jose, CA, USA, 1996, pp. 561-569 vol.2.

[14] A. von Jouanne, P. Enjeti and W. Gray, "The effect of long motor leads on PWM inverter fed AC motor drive systems," *Proceedings of 1995 IEEE Applied Power Electronics Conference and Exposition - APEC'95*, Dallas, TX, USA, 1995, pp. 592-597 vol.2.

[15] J. Salomaki, M. Hinkkanen and J. Luomi, "Sensorless Control of Induction Motor Drives Equipped With Inverter Output Filter," in *IEEE Transactions on Industrial Electronics*, vol. 53, no. 4, pp. 1188-1197, June 2006.

[16] A. von Jouanne, D. A. Rendusara, P. N. Enjeti and J. W. Gray, "Filtering techniques to minimize the effect of long motor leads on PWM inverter-fed AC motor drive systems," in *IEEE Transactions on Industry Applications*, vol. 32, no. 4, pp. 919-926, July-Aug. 1996.

[17] V. Blasko and V. Kaura, "A novel control to actively damp resonance in input LC filter of a three phase voltage source converter," *Proceedings of Applied Power Electronics Conference. APEC '96*, San Jose, CA, USA, 1996, pp. 545-551 vol.2.

[18] L. Malesani, P. Mattavelli and S. Buso, "Robust dead-beat current control for PWM rectifiers and active filters," in *IEEE Transactions on Industry Applications*, vol. 35, no. 3, pp. 613-620, May-June 1999.

[19] T. Kawabata, T. Miyashita and Y. Yamamoto, "Dead beat control of three phase PWM inverter," in IEEE Transactions on Power Electronics, vol. 5, no. 1, pp. 21-28, Jan. 1990.

[20] A. A. Ahmed, B. K. Koh and Y. I. Lee, "A Comparison of Finite Control Set and Continuous Control Set Model Predictive Control Schemes for Speed Control of Induction Motors," in *IEEE Transactions on Industrial Informatics*, vol. 14, no. 4, pp. 1334-1346, April 2018.

[21] T. Geyer, G. Papafotiou and M. Morari, "Model Predictive Direct Torque Control—Part I: Concept, Algorithm, and Analysis," in *IEEE Transactions on Industrial Electronics*, vol. 56, no. 6, pp. 1894-1905, June 2009.